A Thesis for the Degree of Ph.D. in Engineering

Development of Silicon-polymer Hybrid Lenses for Infrared Optical Systems

July 2017

Graduate School of Science and Technology
Keio University

ABDUL MANAF, Ahmad Rosli bin

DISSERTATION

Submitted to the School of Integrated Design Engineering, Keio University, in partial fulfilment of the requirements for the Degree of Doctor of Philosophy

For my parents for supporting me to achieve big,

and

for my wife, Nor Arzuwin binti Ahmad and my childrens, Nurul Insyirah, Muhammad Irfan, and Muhammad Ilman, for their love, support, and sacrifices

Table of Contents

List of figures

List of table

ABSTRACT

The demand for cost-effective infrared (IR) optics has increased over the past decade. Germanium (Ge) has been primarily used for the IR lenses because of its excellent IR transmittance and refractive index; however, Ge is bulky, heavy, and expensive. As an alternative, silicon (Si) is another IR material which is lighter and cheaper than Ge. However, as Si is a typical hard and brittle material, the ultraprecision machining of Si into complicated shapes like a Fresnel lens is considerably difficult. When diamond turning is used for machining Si, the process is very time-consuming, and serious tool wear takes place. In recent years, IR polymers, such as high-density polyethylene (HDPE), have been developed which are much cheaper and easier to shape by thermal molding processes. However, the transmittance of HDPE is still very low, thus the thickness of HDPE lens must be extremely thin, which brings the problem that the lens stiffness becomes very low and thus the substrate is easily deflected. Accordingly, there is an urgent need for exploring alternative IR substrate.

In this study, a novel IR optical lens substrate, namely, the Si-HDPE hybrid substrate, was proposed and developed. An extremely thin layer of HDPE was laminated to one side of a Si wafer by means of silane-crosslinking, and the mechanical strength is further improved by utilizing a mechanical lock structure. Thus, the resulting Si-HDPE hybrid lens substrate possesses the advantages of both materials, i.e., the high stiffness and IR transmittance of Si together with the high formability of HDPE. The hybrid substrate was fabricated by high-precision press molding where the pressure and temperature were strictly controlled. The surface integrity and form accuracy of the developed Si-HDPE hybrid substrates were experimentally investigated. The IR imaging evaluation showed that the hybrid substrate was useable for night vision and thermography.

The main contents of this study are summarized as follows:

1. Experimental results indicate that when the thickness of HDPE layer is less than 100 μm was attached to Si, the transmittance of Si is improved in ~7.4-8.8 μm and ~9.3-12 μm IR region. This is due to the HDPE layer acting as an anti-reflective coating of Si. The interface between Si and HDPE were evaluated and found that both substrates were successfully bonded with the aid of silane-crosslinking under controlled press molding parameters. The bonding of the two substrates occurs due to the chemical reactions at the interface. The bonding helps to eliminate the interface gap which affects the IR

transmittance of the hybrid substrate. The press molding temperature also needs to be controlled as the use of a higher temperature degraded the HDPE and also reduced the IR transmittance. The developed Si-HDPE hybrid substrate was then optically evaluated, and it was revealed that the hybrid substrate was able to capture an IR images with acceptable image quality.

2. Press molding experiments were done, in which micro-lens structures were formed on the thin HDPE layer of the hybrid substrate. Two different lens structures were fabricated; micro-lens array and Fresnel lens. The micro-lens array was press molded at the polymer molten state in a non-vacuum condition. It was found that the air trapping occurs during press molding and caused severe damage to the lens surface and also affected the form accuracy. To investigate, a new in-situ direct observation was developed and used, and it is found that the air pockets were formed between the polymer pellets. Unescaped air during pressing caused the trench formation on lens surfaces which also reflects on mold coating. A numerical simulation conducted verified similar behaviour with the in-situ observation. As for that, pressing force should be kept to the minimum at the higher temperature to reduce the effect of air trapping to the surface integrities and lens accuracy. Press molding in a vacuum condition and shrinkage compensation were also conducted where the form accuracy and surface integrity were significantly improved. Meanwhile, in fabricating the Fresnel structures, a two-step molding method was applied. In the first step, a flat hybrid substrate was formed and the Fresnel structures were press molded in the second step to reduce the effect of air trapping. The form accuracy of the Fresnel was achieved at the higher pressing temperature and force. The experimental results also compared with the numerical simulation and the flow behaviour during press molding was studied.
3. Novel extra-thin Si-HDPE hybrid Fresnel lens was designed and evaluated to demonstrate the hybrid substrate's usability for night imaging and thermography. The performance of the lens was measured and compared with simulated data, which showed good agreement. The night mode imaging trial also demonstrated the Si-HDPE hybrid lens usability as an IR systems lens where the object image at different distances was able to be captured. The thermography image was also captured, and the temperature distribution was shown. The Si-HDPE hybrid Fresnel lens also combined with Ge to show its ability to work with other lens material which resulted in clearer and sharper captured images.

ACKNOWLEDGEMENT

Full praise and thanks to Allah the Almighty for making it possible for me to come to this point in life by granting me the good fortune to work on a Ph.D. research that I enjoyed at Keio University, one of the best institutions in Japan and for seeing me through the ups and downs through the journey that every Ph.D. degree brings about.

Firstly, I would like to express my sincere gratitude to my advisor Professor Jiwang Yan for continuous support throughout my Ph.D. study and related research, for his patience, motivation, and immense knowledge. His guidance helped me in all stages of research and the writing of this thesis. I could not have imagined having a better advisor and mentor for my Ph.D. study.

Besides my advisor, I would like to thank the rest of my thesis committee: Professor Norihisa Miki, Professor Masaki Omiya, and Associate Professor Takasumi Tanabe, for their insightful comments and encouragement, but also for the thought-provoking questions which gave me greater incentive to widen my research from various perspectives.

My sincere thanks also go to Dr. Tsunetoshi Sugiyama, who continuously provided me with technical support during the research. Without his precious support, it would not be possible to conduct this research. Not to forget, many companies are also acknowledged: Global Wafers, Mitsubishi Chemical, Toshiba Machine, to name a few, for providing the samples and technical supports.

A great source of motivation and inspiration for me has also come from my circle of friends here in Keio University – Atiq and Erialdi. I would also like to thank all of my

colleagues in the Precision Machining and Nano Processing Laboratory (Yan Lab), including Dr. Huang, Mukaida, Moriya, Yamasaki, Ishizuka, Niitsu, Takayama, and many others. The atmosphere in our laboratory was very inspirational and supportive throughout these years.

I would like to reserve a very special gratitude, especially to my wife, Nor Arzuwin binti Ahmad, for always being very supportive with her encouragement, understanding, and for taking care of our children; Nurul Insyirah, Muhammad Irfan, and Muhammad Ilman, during my Ph.D. study. This dissertation is also dedicated to my family: my parents and to my brothers and sisters for supporting me spiritually throughout my studies and my life in general.

Last but not the least, I would like to thank Keio Leading-edge Laboratory (KLL) for providing my research grant every year, making it possible for me to participate in overseas and domestic conferences in order to share the idea of my research to the public. Finally, the financial support from Malaysian Ministry of Higher Education and Universiti Malaysia Pahang towards my scholarship for all these years is gratefully acknowledged.

CHAPTER 1

Motivation and introduction

1.1 Overview of issues regarding infrared lenses

In recent years, the demand for IR optical imaging systems has risen, especially in night mode imaging and thermographic applications. High-end IR imaging requires good lens material and is often used in sophisticated technologies, primarily in the military. Meanwhile, the application of the IR optics in engineering, night driving assistance, security surveillance to name a few, are also demanding especially in mid to far IR region (7-14 μm).

Recently, a new IR camera detectors which offer inexpensive detector are been developed [1]. This offers opportunities for the development of the cheaper IR camera system. Meanwhile, the current trend of the camera are also towards the miniature and compact system. However, due to the complicated and costly process of fabrication the IR lenses, the IR camera systems will remain out of the reach of the majority. It is due to the characteristic of some IR material which is hard to machine. If the manufacturing cost of the lens can be reduced, it is expected to reduce the cost of IR camera systems.

Germanium (Ge), for example, possesses excellent transmittance rates in the mid-to-far IR region. However, it is bulky, heavy, and expensive [2]. Silicon (Si) is relatively lower in cost compared to Ge. It is also lighter, and in contrast, its IR absorbance is higher than that of Ge. However, machining both Ge and Si materials are difficult and expensive towing to their hard and brittle nature [3–6]. Ultraprecision machines and extremely sharpened diamond tools are

necessary to enable the ductile machining of Si and Ge. Machining the IR lens materials such as Ge and Si requires high precision and high stiffness machining. The machines must also be usable under a stable environment with strict temperature control and vibration isolation. In addition, the production cost is exorbitant because expensive single-crystal diamond tools are worn down very quickly especially when machining Si. These problems greatly limit the productivity and application of high-precision IR optics for everyday use.

The polymer material is an alternative solution for expensive and difficult to machine substrates. High-density polyethylene (HDPE) offers a cheaper solution [7]. However, compared with Ge and Si, HDPE suffers from high IR absorbance and needs to be formed in very small thicknesses to obtain acceptable levels of IR transmittance. Thus, the stiffness level reduces and the substrate is easily deflected.

A hybrid optical lens may work for visible light optical application [8,9]. It combines the various optical properties of the composing lens materials. Past research has demonstrated that a combination of glass and polymer can reduce the manufacturing cost, and improve the optical properties of the lens systems [10]. With that, it is believed that combining HDPE with Si will enable it to be used as IR substrate. The HDPE can be formed as a thin layer and attached to the Si. The Si will retain the shape of the HDPE layer; nevertheless different IR properties of the material can be selected and combined. The lens structures can be formed on the HDPE layer using a thermal shaping process. Thus, a cheaper solution of IR lens can be fabricated.

1.2 Significance of the research

Although it is possible to develop the Si-HDPE hybrid substrate/lenses by using press molding, the adhesion between the Si and HDPE need to be developed. However, the use of silane crosslinking polymer make it possible to be realized in which tenth of micron HDPE

thickness can be attached to the Si. The thickness of the polymer was determined to achieve higher IR transmittance. As the press molding of the lens structures on the thin HDPE layer of the hybrid substrate is not reported in any literature, this research demonstrated the ability of the hybrid substrate to be formed precisely into an IR lens. Furthermore, the development of in-situ direct observation in this research also clarified the air trapping phenomenon due to the used of the HDPE pellets during press molding. This research also demonstrated the capability of the Si-HDPE hybrid lenses for IR imaging including thermography in which the temperature distributions are measured. Furthermore, this research aims to contribute towards lowering the manufacturing cost of fabricating IR lenses, thereby helping realize thin and compact IR imaging systems.

1.3 Research objectives

The objectives of this research are as follows:

1. To fabricate a Si-HDPE hybrid substrate/lens for IR applications for the wavelength of 7-14 μm. The adhesion method for Si and HDPE also needs to be developed. The gap between the substrate needs to be eliminated during the bonding process failing which it could detriment the IR transmittance. The interface phenomenon of the substrate also needs to be investigated.
2. To evaluate and determine the resulting IR properties of varying HDPE thicknesses of the hybrid substrate, and the image quality of the hybrid substrate with various HDPE thicknesses, respectively.
3. To form the lens structures on the thin layer of HDPE of the Si-HDPE substrate utilizing the press molding method. Also, to show the viability of forming the lens structures of the hybrid substrate using press molding, and to define the best process parameters.

4. To investigate the air trapping phenomenon during process needs, especially as the press molding is done in a non-vacuum condition. Also, to develop a new in-situ online observation method to study the formation of air trapping between the polymer pellets.
5. To design the lens using the Si-HDPE hybrid substrate to be used for IR application. Also to show the viability of the hybrid lens for IR imaging systems applications.
6. To verify the performance of the designed lens in the IR imaging, by developing home build testing equipment. Also to measure the lens performance, and the image quality was also evaluated. The possibilities of combining the Si-HDPE hybrid lenses with other lens material will also be examined.

1.4 Organization of dissertation

Chapter 1 provides the introduction and overview of the issues regarding research. The research significance and also the research objectives were included in this chapter.

Chapter 2 provides an overview of lens fabricating techniques, as well as the IR imaging systems and the materials normally used in fabricating the IR lens. In this chapter, a method that past researchers used for fabricating a hybrid optical lens was detailed as well.

Chapter 3 details the initial steps of fabricating the Si-HDPE hybrid lens. The method of combining the HDPE to the Si, and the interface phenomenon between Si and HDPE, and the IR evaluation and optical abilities of the hybrid substrate is explained in this chapter.

In Chapter 4, contains the fabricating processes of forming microstructures on a HDPE layer of the hybrid substrate The mold design and machining methods are included in this chapter. Chapter 4 also examines the effect of the press molding parameters in maintaining surface integrities, and for accuracies of the microstructures, including the coating. The in-situ observation of air trapping phenomenon during the press molding is also detailed here. In

addition, a numerical simulation also described as well. A press molding in a vacuum environment and the resulting results of the form accuracy and surface integrities of the microstructures are also included in this chapter. Also, the formation of a Fresnel shaped out of Si-HDPE lens, and the mold fabrication prior to the press molding processes were explained.

Chapter 5 delineates the lens and IR imaging evaluations respectively. The lens design and analysis are provided to show the performance of the designed lens. The lens performance was measured, and it was compared to simulated data. The formed lenses were tested using a home built imaging system, during which, the captured night mode and thermography images, demonstrated the designed and fabricated lens's ability to visualise objects during the IR imaging. The combination of the different IR lens materials was also introduced in this chapter to examine the compatibility of the Si-HDPE hybrid lens with other lens material.

Chapter 6 consists of the overall conclusion of the research. The future of this research area is also included.

CHAPTER 2

Literature review

2.1 Precision IR lenses fabrication

An infrared lenses are usually made from hard and brittle materials such as silicon and germanium. These materials had to experience a complicated shaping process in order to transform them into a final shape. A conventional method that involves three steps, particularly grinding, lapping, and finishing are imperative procedures for the transformation [11,12]. This method can be used to form a single lens and derive a good surface finish. However, it is inefficient to produce the complicated lens shapes in a large quantity that can be costly and time-consuming. The worst of it is the use of cutting fluid in the process is detrimental to our environment. Figure 2.1 illustrates a schematic diagram of the precision lens grinding process.

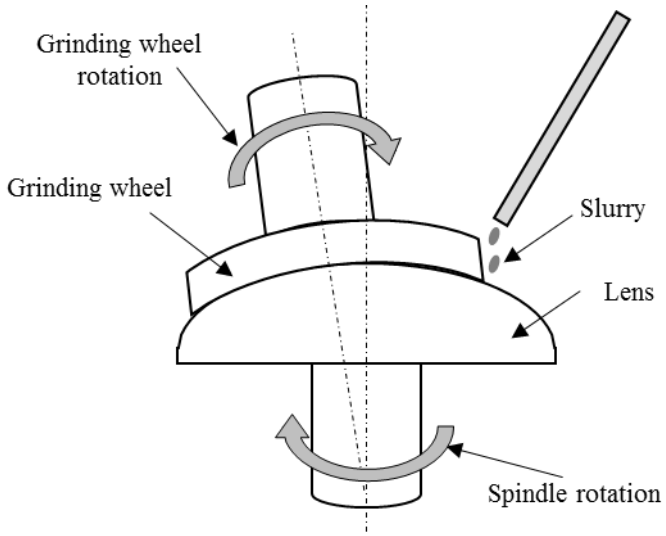

Figure 2.1: Schematic diagram of lens grinding process.

Precision glass molding process (GMP) is a prominently used method to fabricate the optical lenses at lower cost [13–15]. This lens molding process involves heating and cooling. During the thermal process of the molding, the glass is heated to the glass transition point with the aid of the IR heater, and subsequently it forms a viscoelastic material. Then, the nitrogen gas is used to cool down both mold and lens after the lens are press molded. This process is effective to produce the glass lenses, and obtain the accuracy and excellent surface finish of the lenses. The schematic process of the GMP is illustrated in Figure 2.2.

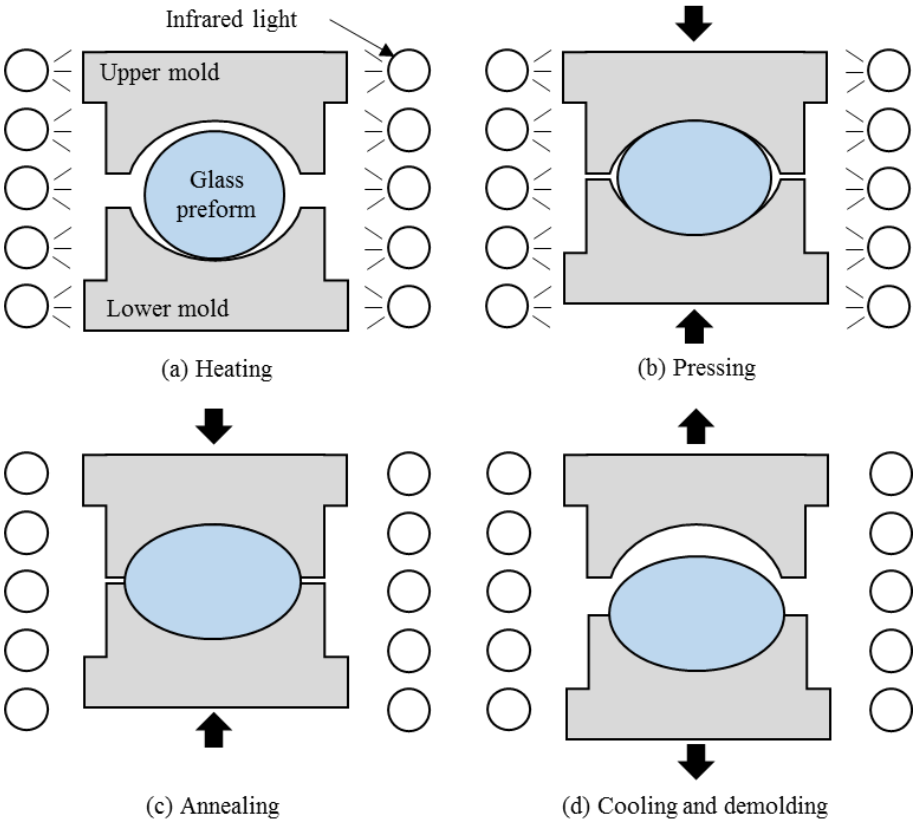

Figure 2.2: Schematic diagram of precision glass molding process.

Chalcogenide glass is considered as an alternative material for the IR lenses [16]. Similar to a visible light glass lenses, it can be molded by using the GMP process effectively while the form accuracy can also be obtained. The chalcogenide glass can be heated above the softening point, pressed, and finally cooled. However, it is very sensitive to the molding process because the parameters of the GMP can influence the lens performance. This material

is subjected to the changes in refractive index due to the stress during molding [17]. During the GMP process, precaution measures need to be taken against the negative effects the glass will bring to the environment. It is due the chemical contents of the chalcogenide glass which contains hazardous and poisonous chemical for example arsenic. Therefore, the glass should be molded in vacuum surrounding to minimise the effect. Another major issue of this process is the long thermal cycles. The mold is also subjected to the thermal expansion that shortens the life span of the mold. This is a departure for many researchers to conduct their studies experimentally and numerically in response to this issue.

Although the glass molding process is advantageous to the formation of the glass lenses, it is not applicable to silicon and germanium which require a higher softening point of both substrate. Given that the maximum operating temperature of the GMP is 800 °C, the softening point of more than 800 °C is mandatory to both silicon and germanium.

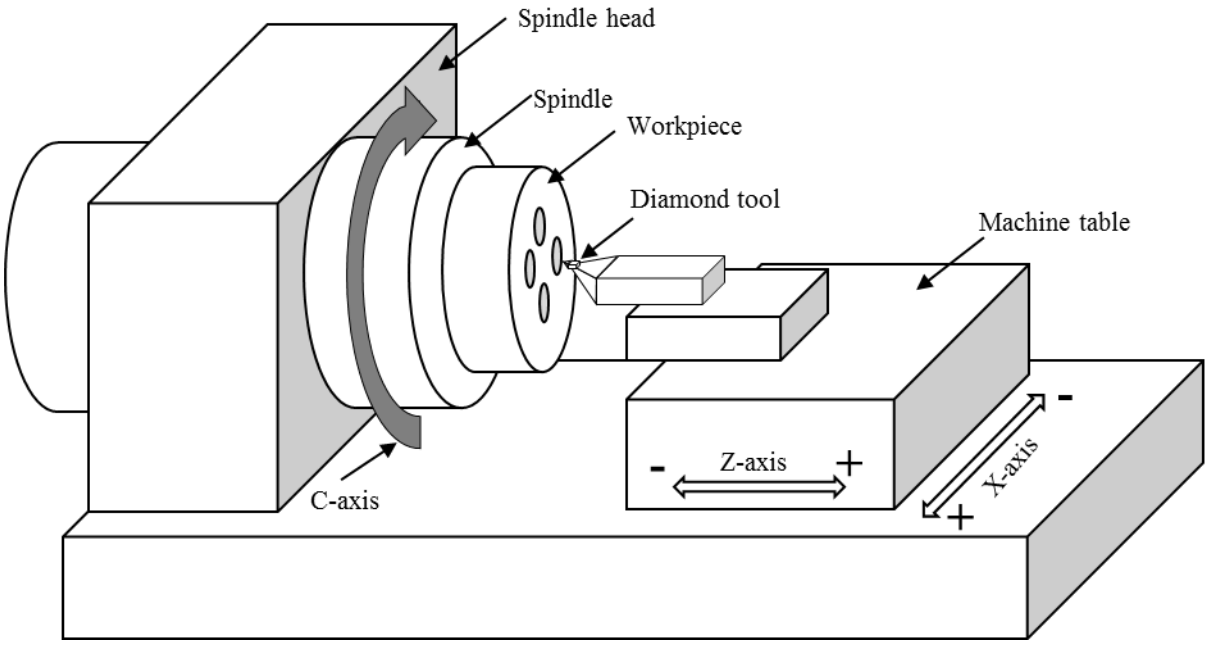

Figure 2.3: Schematic diagram of ultra-precision diamond lathe.

Ultra-precision diamond lathe machine enjoys scholarly attention being the lens manufacturing method [4,6,18]. An aspherical to micro-lens array can be fabricated by using

this machine with a high accuracy and surface finish. With a combination of diamond point tools and slow tool servo systems, the machine eases the entire lens cutting process. This machine also enables the production of different shapes of the lens with the support of computer numerical code (NC) generation. The schematic diagram of the ultra-precision diamond lathe is shown in Figure 2.3.

Although ultra-precision machining can produce different forms of lens, it still suffers from inevitable drawbacks. This method is similar to the conventional grinding and lapping process, which does not have the function to manufacture hard materials. As Si and Ge are hard and brittle, the cost incurs is much higher when adopted to fabricate lens from these two materials in a mass production. In fact, machining Ge is easier than machining Si [19]. A ductile mode cutting must be activated during the process to ensure that the precision and higher surface finish to be obtained. In the similar vein, the use of the diamond pointed tool also incurs higher fabrication cost. However, the lens cutting process may cause the machine to be easily worn out that reduces the machining efficiency.

2.2 Infrared imaging

A body with a temperature above the absolute 0 °C will release radiation energy or electromagnetic (EM) radiation. When EM is released, radiation is distributed from the body, the rate of which depends on the temperature of the body. The radiation that is emitted from the body is also called emissivity, which functioned as an IR wavelength [20]. The IR wavelength consists of, near-IR, mid-IR, and also far-IR. The maximum radiation energy, which depends on body temperature, can be calculated using Plank's equations:

$$W(\lambda, T) = e(\lambda) C_1 / \pi \lambda^5 \left[\exp\left(\frac{C_2}{\lambda T}\right) - 1 \right] \quad (2.1)$$

where *W (λ, T)* represents the wavelength radiance in μm; and temperature in Kelvin (*K*). Meanwhile, the radiance, C_1 is 3.7418×10^8, and C_2 is 14387.9 in units of watts m^{-2} steradians^{-1} μm^{-1}, which are constant for the equation. The emissivity of a wavelength which is varied in the range of 0 to 1, is represented by *e* (λ).

A special devices or systems is required to capture the body emissivity, which cannot be captured by the normal invisible camera. Individuals with normal eye-vision lack the ability to view of 0.4 – 0.7 μm light [21]. However, this view can be captured using an IR camera equipped with the cooled or uncooled image sensor. A special lens material is also attached to the camera, which can transmit the IR from the object body to the camera sensor via the lens. In fact, anything which emits the heat from the body can be captured with IR imaging systems. Figure 2.4 showed some of the applications of the IR camera.

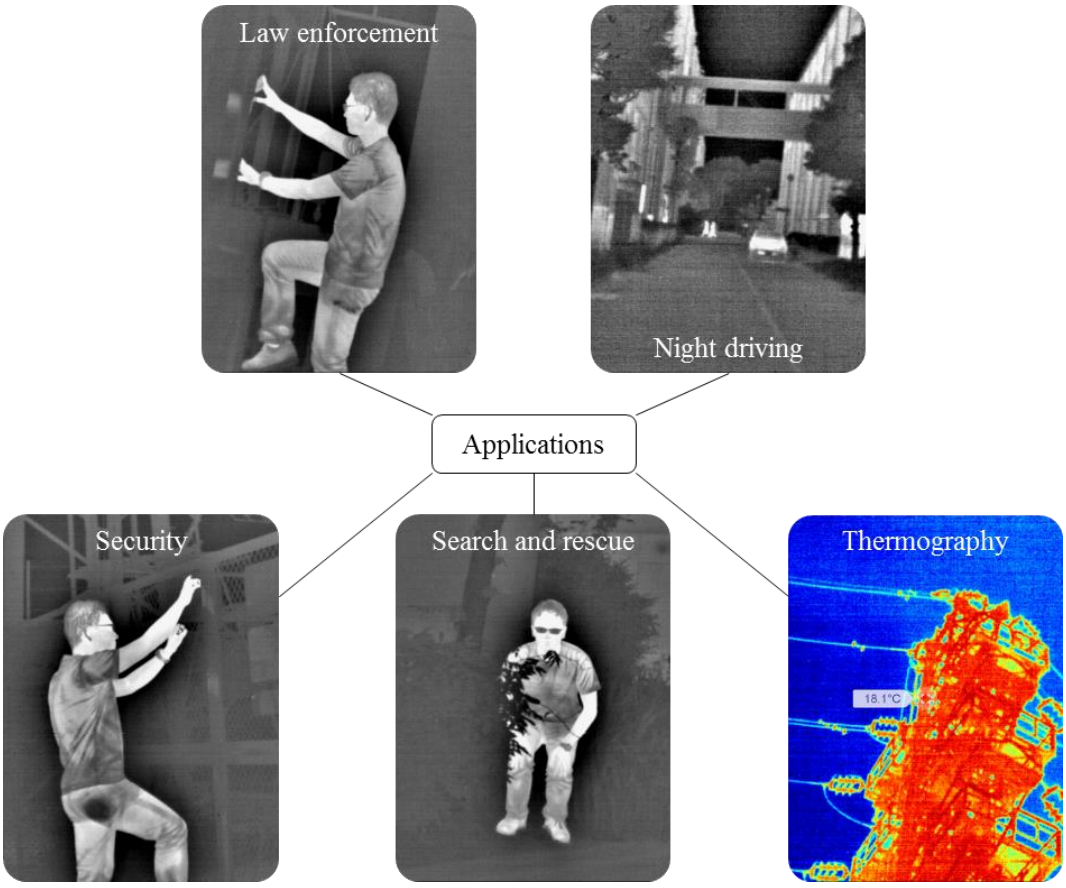

Figure 2.4: Examples of IR imaging applications.

2.3 Infrared lens material

IR material can be made conventionally from several types of material. These materials are usually either made from semiconductors or crystalline. Germanium (Ge) and silicon (Si) are examples of semiconductor material. Some of the lenses are also made from a glass, for instance the chalcogenide glass (Ch). The aforementioned substrates will offer different characteristic of IR properties, each with different applications. This is displayed in Figure 2.5. These materials have their own advantages, drawbacks. The details of the IR material will be discussed after this section's sub-topics.

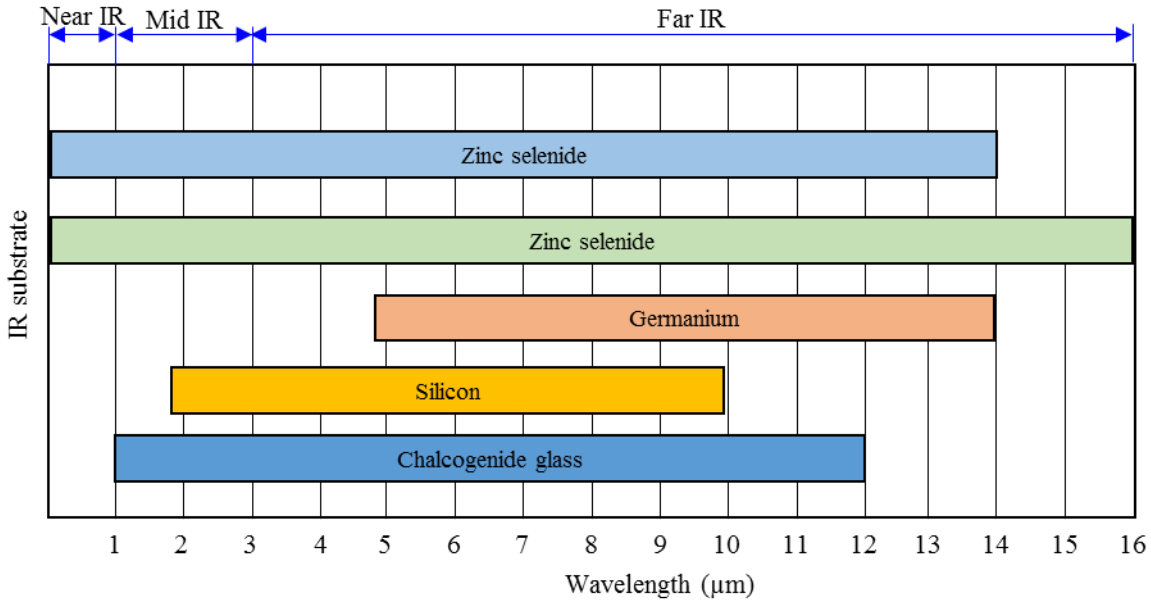

Figure 2.5: IR transmittance comparison of different IR substrates.

2.3.1 Germanium

Germanium (Ge) a semiconductor material, is very popular as IR lens material. It has high permeability and a high refractive index, the latter of which is around 5.76. Meanwhile, it has stable and good transmittance in the IR region of 2-14 µm. Thus, it is an excellent candidate for infrared lenses substrate material.

Ge is relatively expensive, bulky, and heavy. Machining Ge into a flat and thin Fresnel shape appears to be the appropriate solution for reducing its weight [4]. However, fabricating the germanium into the final shape of the lens is a difficult and time-consuming process, and the resulting lenses are expensive. During heat exposure, Ge becomes opaque at about 400 °C, while its transmittance decreases by a factor of 2 at a temperature above 120 °C. Figure 2.6 shows an example of IR lens made from Ge.

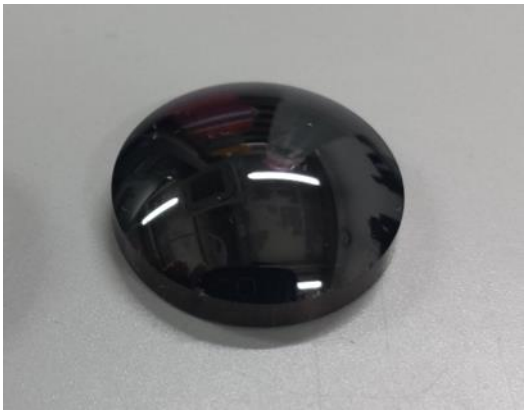

Figure 2.6: An example of Ge lens for IR imaging.

2.3.2 Silicon

Silicon (Si) is a popular material for electronic and photonic applications as it is cost-effective [22]. It can be found in rocks, sand, clay and soil, as well as in other elements such as silicates. In its oxide or silicate form, it can be used to makes glass. Si is a brittle material and is used in many industries. It has become popular for optical components such as IR lenses and thermal imaging cameras. Si has a high transparency for far infrared (FIR) and is opaque for visible light. It also has excellent optical properties and thermal conductivity. The refractive index of Si is ~3.5.

Although silicon can be used in IR optical applications, it has its own set of limitations. Reflectance is one of the problems, and although anti-reflective coating can be used to solve the issue, nevertheless the coating is not always appropriate for infrared optical systems [23].

Meanwhile, the IR transmittance depends on the thickness of the Si. A significantly higher IR transmittance is recorded when the thickness of Si is less than 1 mm [24].

Si costs less than Ge, and the former is also light. However, to mold Si into the final shape of the IR lens, a precision machining is required. Ductile mode machining needs to be used when machining this kind of material. Specifically, an extremely sharp diamond point tool is required to make sure the ductile machining mode is realized. Typically, however, the diamond tools gets worn out very quickly due to the Si characteristics itself. Another method Si can also be shaped using an etching process. Nevertheless, the process is very time-consuming making it an unpopular choice.

2.3.3 Chalcogenide glass

Recently, chalcogenide glass has received a considerable amount of as suitable IR lens material. Chalcogenide glass has excellent IR transmission in the mid to long IR [16]. It offers a cheaper solution compared to Ge. The former's refractive index (~2.5) is slightly higher than Si and slightly lower than Ge [25]. The forming process is considerably cheaper, as the lens shape can be formed using molding processes, especially using the glass molding press machine [26–28]. However, molding this particular type of material is hazardous, due to the contents of the material, which include arsenic and selenium. The only relatively safe ingredient of the glass is sulphur.

2.3.4 High-density polyethylene

Although there are many types of polymers that reportedly can be used for optical systems, not all of them are suitable for IR applications. Polycarbonate (PC) and acrylic, for example, are good for visible light as owing to their optical clarity [29,30]. However, in IR light, this polymer is opaque, wherein IR is absorbed by the material. The IR absorption of the

polymer is due to the molecular vibration that occurs when IR light passes through it [31]. Specifically, it is because the normal polymer has light elements of carbon, hydrogen, and oxygen, wherein higher vibrational frequencies occur.

The use of the polymer allows several thermal fabrication methods to be used to form the lens into its final shape; for instance by using injection molding and hot embossing. Unlike Ge and Si, the polymer can be heated into a softened state, before undergoing hot embossing. The polymer can be melted inside the injection molding barrel before being injected into the mold. The polymer then changes to the solid state after being hot embossed or being used in injection molding. When cooled the final product will be easily obtained.

High-density polyethylene (HDPE) is the most suitable material to be used as IR material; this has been reported over 4 decades ago [32]. It is commonly available and used in various industries. HDPE's good IR transmittance, in 6-14 μm region, is significantly higher than most polymers [33]. Previous research has highlighted the use of this material as an IR lens [34]. However, it still suffers higher from IR absorbance and needs to be formed into a very thin lens so as to compensate for the IR losses. Figure 2.7 displays a 300 μm thick Fresnel lenses, to compensate for IR absorbance.

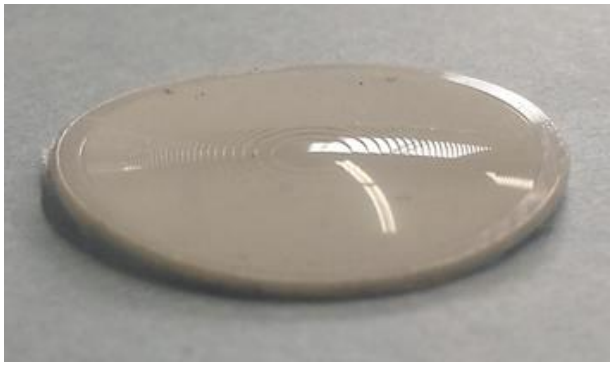

Figure 2.7: Thin Fresnel lens for IR applications.

2.4 Previous research works in the literature

In fabricating hybrid optics, several methods are utilized by the previous researchers. Various types of optical materials were attached, mainly to improve the lens performance, as well as to reduce the manufacturing cost. For instance, the achromatic lens, which is a lens consisting of different optical materials, which were combined to form a hybrid lens.

2.4.1 Previous works on hybrid lens

Ultraviolet (UV) curable resin was the earliest method used to fabricate a hybrid lens whereby the resin was applied to the substrate, and subsequently it was cured by UV light [35–38]. Before the UV curing (hardening) process starts, a suitable amount of UV resin is placed within the lens mold. After that, the glass lens is placed on the top of the UV resin, while the resin is cured with the aid of UV light. As a general rule, the glass lens or the mold must be UV light transparent to ensure that the UV light can be transmitted in order to harden the resin. The process of UV curing resin is illustrated in Figure 2.8, whereas an example of a hybrid glass-polymer is illustrated in Figure 2.9. This method provides a strong adhesion between the two materials.

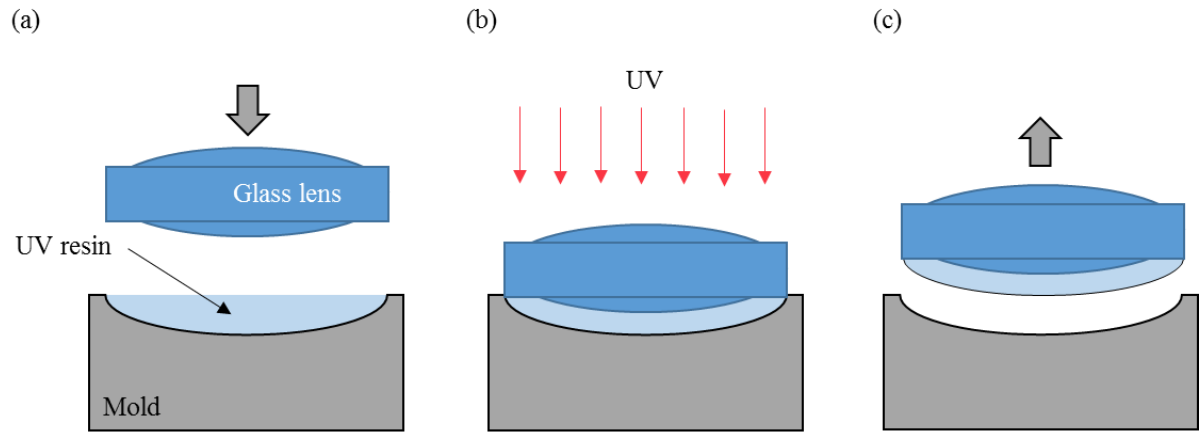

Figure 2.8: Hybrid glass-polymer UV curing process: (a) placement of UV resin and glass lens, (b) UV curing process, and (c) demolding.

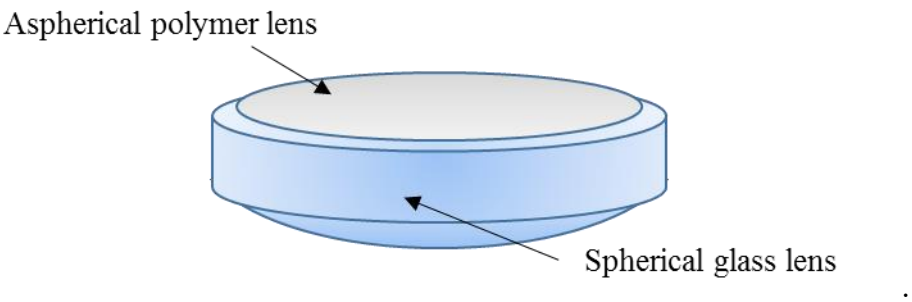

Figure 2.9: Glass-polymer hybrid lens fabricated using UV curing method.

Despite the usefulness of UV curable method, the curing process is indubitably complicated. The curing needs to be controlled properly as excessive UV power can cause the UV material to crack [37]. Due to the use of liquid UV resin, the air trapping is another problem in the process [39]. After pouring the UV resin into the mold, the resin will expose the material to the air trapping phenomenon, and thus it is strongly advisable to perform the process in a vacuum condition. However, the use of this method for producing hybrid IR optics is impossible because UV resin cannot transmit the IR. To date, there is no research done on the use of the UV resin as IR lenses.

Another method used to fabricate a hybrid glass-polymer lens is injection molding. This method has a special design of the injection mold which controls the lens's characteristics. To use this method, the glass is first inserted into the mold, then the molten polymer is injected to cover one side of the glass [10], as described in Figure 2.10. However, no adhesive agent is used in the injection molding process. The resulting lens assembly is held by the flange of the polymer lens. Most importantly, this process can produce the lens in a large quantity at cheaper cost with lower time cycles. A similar process is used to fabricate a silicone-glass hybrid lenses for photovoltaic application [40].

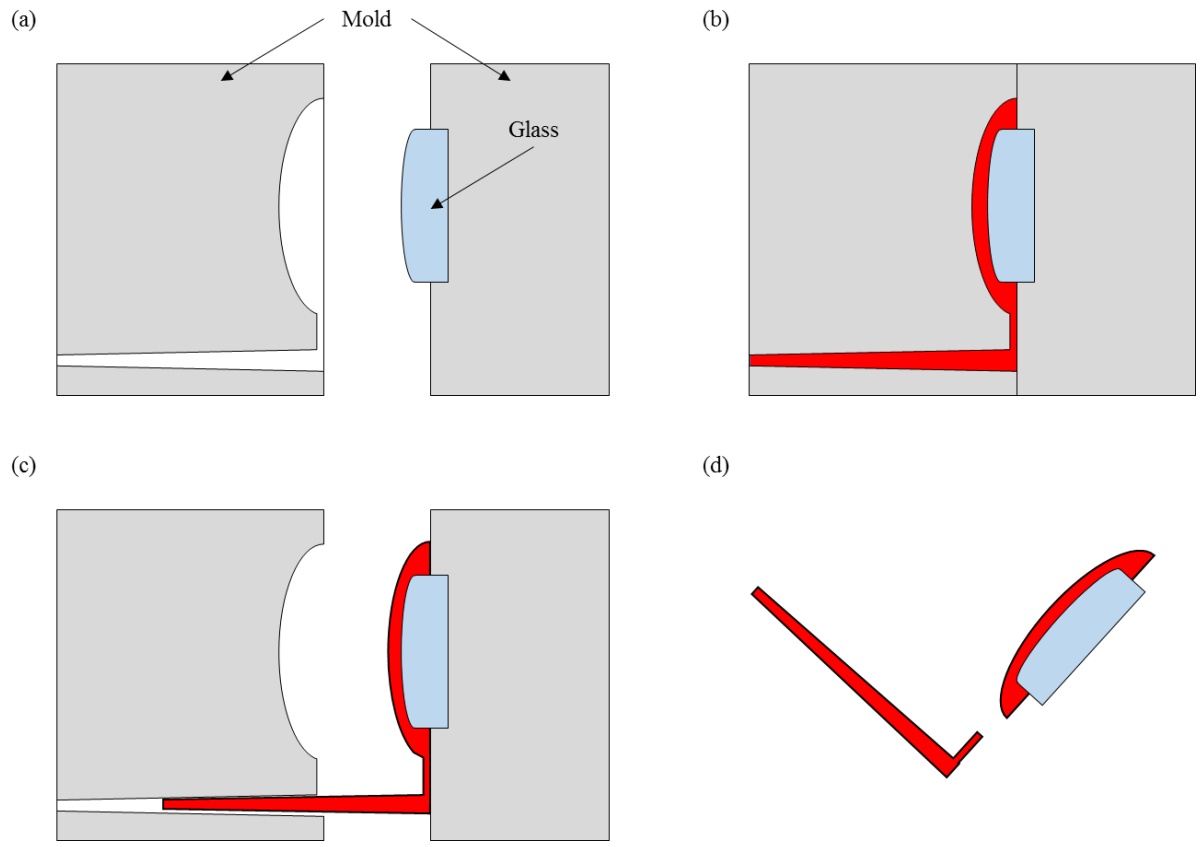

Figure 2.10: Fabrication of glass-polymer hybrid by using injection molding: (a) a glass lens is inserted into the mold, (b) the mold is closed and polymer injected into the mold, (c) the mold is opened, and (d) the hybrid glass-polymer lens is completed.

To guarantee a mass production of the lens, a multi mold cavities can be implied to the injection mold to allow the production of multiple lens in one injection molding cycle. Still, the injection molding suffers from some shortcomings. The effect of polymer flow will reduce the performance of the lens [10]. Hence, care should also be taken in designing the mold, especially the gate size and location where the polymer enters the lens cavity after being injected through the machine nozzle. When the hybrid lens are manufactured through this process, a weak adhesion exists between the two lens substrate due to the shear force between the substrate at the cooling stage.

Figure 2.11 exhibits the compression molding process, which is another method used to fabricate glass-polymer hybrid lens. Through this method, a glass lens is molded and used as the lower cavity then. After that, the polymer is inserted on the top of the glass to be heated

and pressed. The polymer is adhered to the glass by heating and cooling the polymer during compression. The adhesion can be improved by applying hot glue between the two substrates [41].

In general, the compression molding process is similar to the GMP process. It enhances the efficiency of molding the optical lenses. The control of the pressing force can improve the adhesion between the two different substrate during the molding process. Concurrently, it can reduce the effect of shear force on the interface of the substrate.

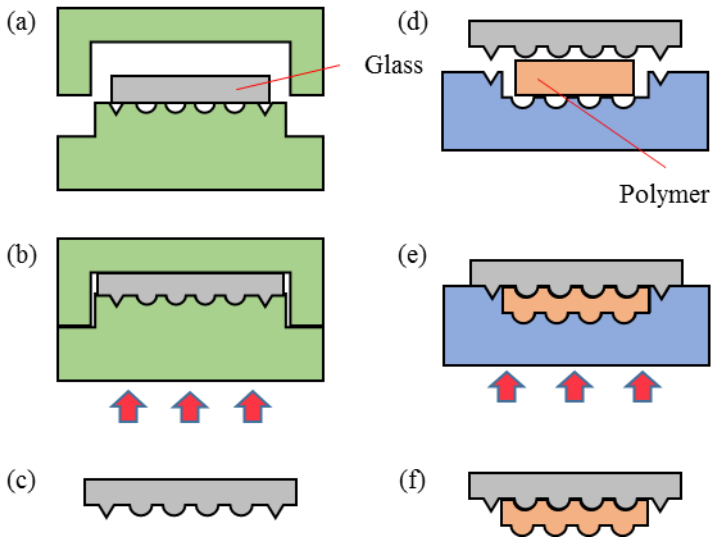

Figure 2.11: Fabrication of glass-polymer utilizing the compression molding process: (a)-(c) glass molding process, and (d)-(f) hybrid glass-polymer hot embossing.

A combination of glass and Si for simultaneous visible and infrared imaging has also been performed, whereby the glass is placed at the centre of a Si lens without any adhesion [42]. The combination of the Si and the glass for this application is showed in Figure 2.12. Undeniably, the fabricating process is challenging. This is because the time-consuming etching process is utilized to fabricate the Fresnel lens, which are made of silicon. Nevertheless, the quality of the surface finish produced through this method is considered poor as compared to other lens forming methods.

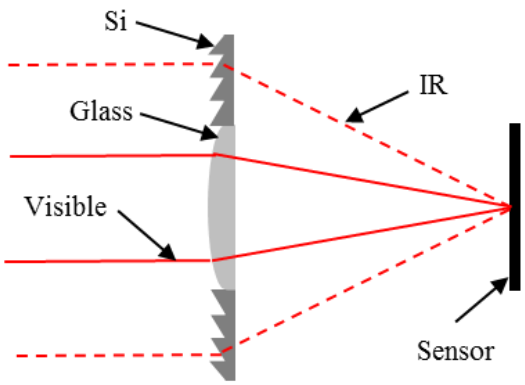

Figure 2.12: A Si-glass hybrid lens.

Attaching a polymer onto Si has been reported previously, and the adhesion of the polymer substrate to the Si was done with the help of the chemical process. In the present study, an adhesion chemical was applied to the Si, and the polymer was attached. The diamond turning was then used to cut the polymer into the final lens shape [43,44]. It should be added that, in using the adhesion between these two materials, care should be taken in choosing the appropriate adhesion material. This is because the adhesion material used must be able to transmit the IR light.

A chemically attached polymer to the silicon helps to improve the adhesion between the two materials. However, it involves several process starting with the adhesion process and ends with the cutting process. During the adhesion process, the uniformity of the adhesion need also to be considered. On contrary, the ununiformed adhesion process creates an interface gap between the two substrate that allows the light to be reflected on the interface gap, and eventually the lens performance reduces. The interface phenomenon is not reported.

CHAPTER 3

Press molding of Si-HDPE substrate

3.1 Introduction

In this study, a Si-HDPE substrate is fabricated. A HDPE layer is attached to one side of the Si, as illustrated in Figure 3.1. The HDPE thickness is formed in a varying thicknesses to investigate the effect of these variations on the IR transmittance of the hybrid substrate. To attach the HDPE to the Si, no adhesion promoter is used, and the attaching process is done in melt condition of the HDPE.

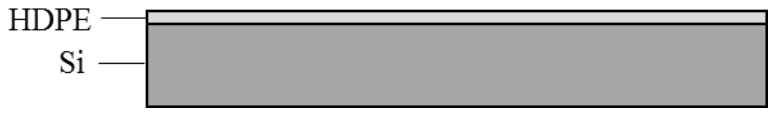

Figure 3.1: Si-HDPE hybrid substrate.

In this study, a glass molding press (GMP) machine is used as a press molding to form the Si-HDPE hybrid material. The molding temperature and pressure is precisely controlled in order to ensure that the shape transferability, surface quality, and interface strength can be improved [45,46]. Glass is normally formed at high temperatures (~500°C) which are above the glass transition temperature. At this point, the glass is in its softened state. In this study, as the HDPE polymer exhibits a lower softening temperature (125°C) and a lower melting point (133°C). Therefore, forming the Si-HDPE hybrid structure is more easily done in the melt state of HDPE, which is similar to that used in other applications [47]. Forming the polymer in its

melt state is also beneficial for complete replications of microstructures or complicated shapes to the polymer, without damaging the mold and the thin Si substrate. Moreover, forming the Si-HDPE in the melt state also helps to create strong Si-HDPE adhesion during the press molding process.

In the experiments, two types of materials were used. The first is single-crystal Si with 755 μm thickness in the form of a two-side polished wafer, which was provided by Global Wafers Japan Co. Ltd.. The properties of the Si material are displayed in Table 3.1. The Si wafer is then cut to the size of 15 mm × 15 mm using a diamond pen. Cylindrical HDPE granules with resin/pellets size of Ø3 mm × 3.5 mm, supplied by Mitsubishi Chemical Corporation, Japan, were used in the experiments. The grade of the HDPE material is LINKLON HM600A, which is a silane cross-linkable resin. This type of HDPE was selected because of its adhesive ability to Si.

Table 3.1: Si material properties

Material properties	Value
Type	P
Doping element	Boron
Resistance, Ω.cm	27
Surface orientation	(111)
Thickness, μm	755
Refractive index	3.5
Surface roughness (Ra), nm	3.5

The properties of the HDPE granules are displayed in Table 3.2. The utilization of a silane cross linkable, such as HDPE does not require an adhesive because of its ability to create a direct bond between non-polar surfaces [48,49]. Crosslinking is a type of polymerization

reaction in which branching occurs out from the main molecular chain to form a network of chemical links.

Table 3.2: HDPE material properties.

Material properties	Value
Density, g/cm³	0.955
Melting point, °C	133
Softening temperature, °C	125
Shape	Granules
Grain size, mm	Ø3 × 3.5
Melt flow rate (190℃,21.2N), g/10min	9
Refractive index	1.5

3.2 Si-HDPE substrate design

To attach the HDPE layer to Si, several methods were developed. As the Si used in the experiment is polished, the HDPE does not adhere very well. Roughening the Si surface improves the adhesion of the two substrates. However, doing so will scatter the IR light when it is passing through an uneven surface of the Si substrate. The effect of the rough surface on the IR transmittance of the Si can be viewed in Figure 3.2, where is demonstrated that polished Si would result in higher IR transmittance.

To improve the adhesion between HDPE and Si, a mechanical lock is considered, simply by securing the assembly using strong locking devices [50]. The mechanical lock or coupling was the earliest method introduced by MacBain almost 9 decades ago [51]. The shape irregularities or undercuts will become the mechanical coupling to attach the different substrate. The shape irregularities or undercuts become the mechanical couplings to attach the differing substrate. By considering this, research implemented the locking idea, to improve the adhesion between HDPE and Si.

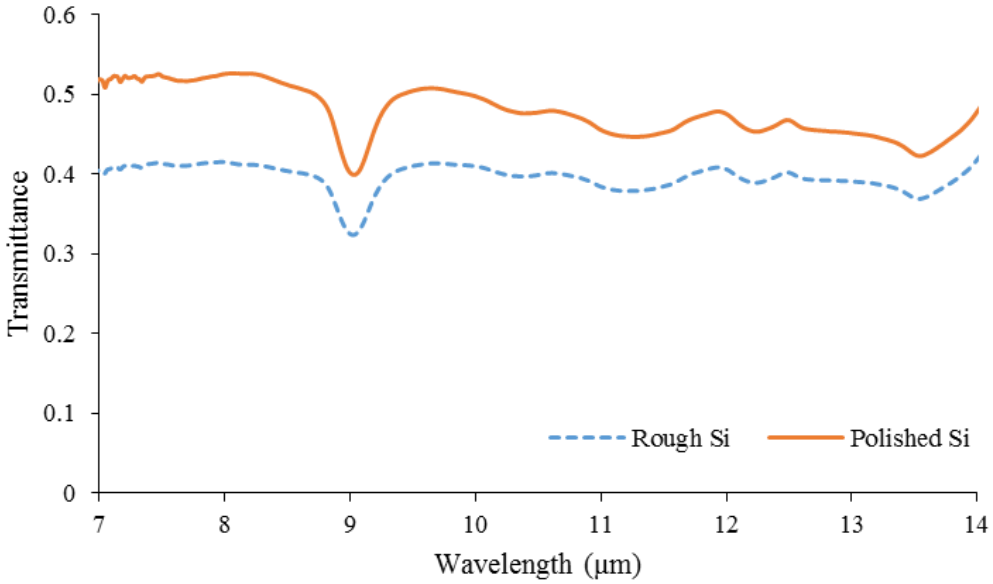

Figure 3.2: IR transmittance of rough and polished Si.

To create surface irregularities in some area of the Si surfaces, the used of drilled holed was considered. The first trial was conducted by drilling a hole into the Si using a laser. The HDPE layer is then created by heating and pressing it onto the Si. During pressing, the molten HDPE flows into the drilled hole to become the mechanical lock for both substrates.

However, it is found that the Si is easily broken after the press molding process, especially at the laser drilled holes. This leads to micro-cracks around the hole. The micro cracks are then subjected to a pressing force during the press molding, and this causes the Si to break. Thus, the laser drilling method is not suitable for this study. The sample of the Si-HDPE hybrid substrate that uses laser drilling holes as its locking is shown in Figure 3.3.

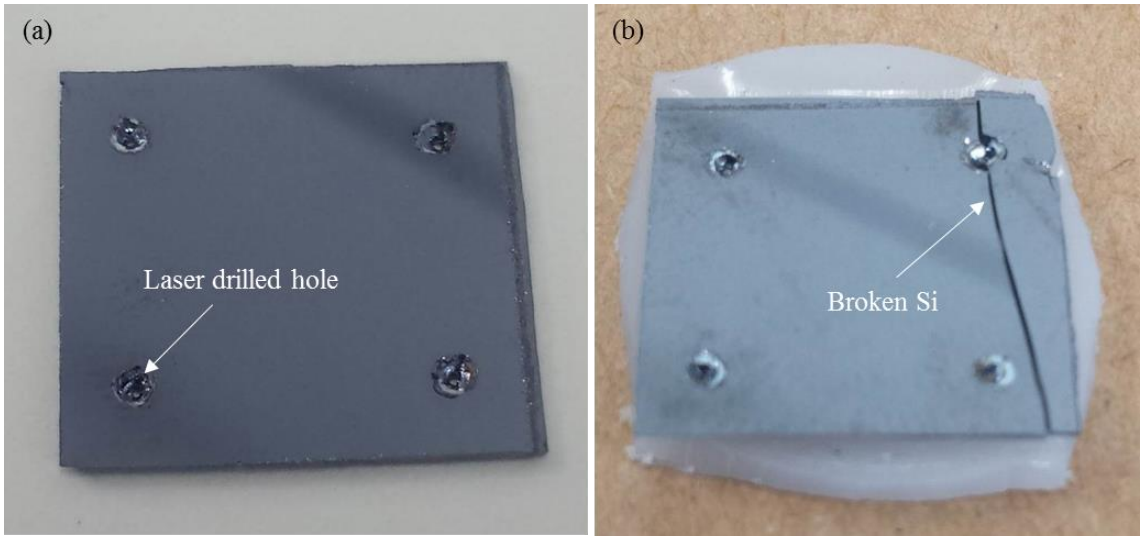

Figure 3.3: Photograph of: (a) a laser-drilled Si, and (b) a broken piece of Si after press molding.

The structure of the Si-HDPE hybrid structure test piece was improved, and this is schematically shown in Figure 3.4. In the design of the hybrid substrate, the HDPE laminates one side of the polished Si, and the adhesion of the HDPE to the Si is carried out via cross-linking. As mentioned above, in order to improve the adhesion strength between the two materials, a mechanical lock (undercut) was designed at the edge of the Si substrate, leaving an effective lens area of 13 mm × 13 mm, after subtracting 1 mm for locking. In this way, the fragile Si substrate is fully protected by the HDPE from external shocks. Furthermore, the flatness of the HDPE film can be firmly maintained by the Si substrate.

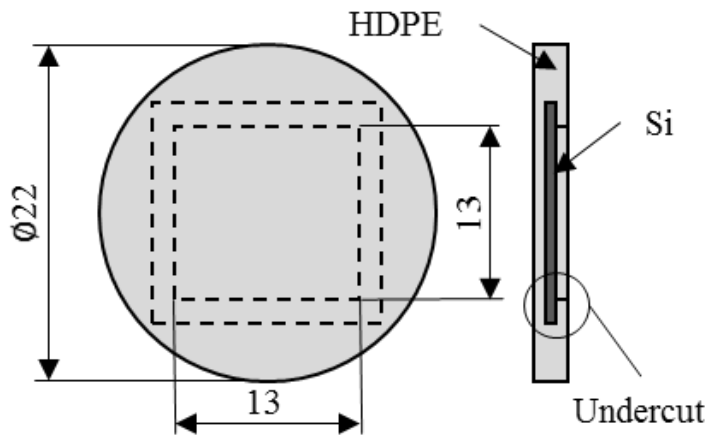

Figure 3.4 Si-HDPE hybrid structure design.

3.3 Mold design and fabrication

Aluminum was selected as the material for the mold due to it being malleable in the machining process. As the HDPE polymer is also soft, the strength of aluminum is sufficient to prevent mold deflection. Next, the upper mold used in this study was shaped by using a universal lathe from an aluminium cylinder, to a diameter of Ø40 mm and a height of 20 mm. The top surface of the mold was then flattened/micro-structured using an ultraprecision lathe, NanoForm X (Ametech Precitech Inc., USA). The machine was equipped with an air bearing spindle and a single crystalline diamond tool, with a nose radius of 250 µm. The final mold surface had a mirror finish, with a surface roughness of 7.8 nm Ra.

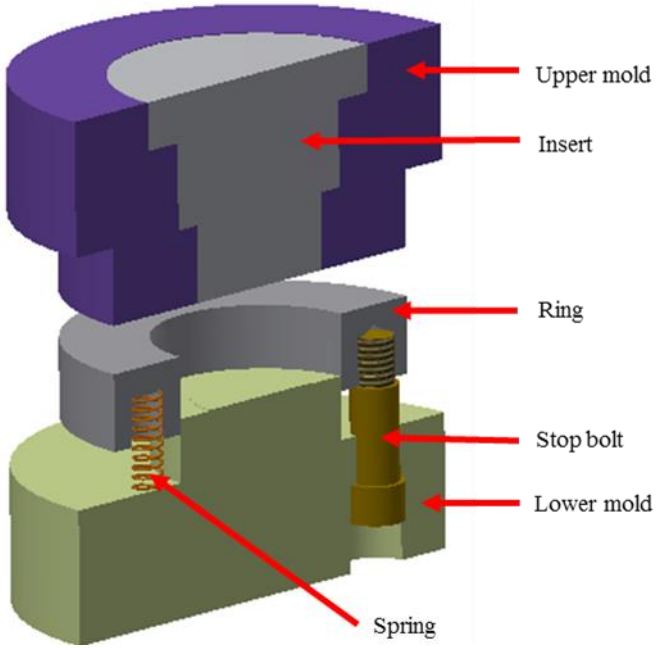

Figure 3.5: Schematic diagram of upper and lower mold structure.

The lower mold comprises of a group of elements, as is schematically shown in Figure 3.5, to form a flexible mold cavity. This is essential to control the shape of the HDPE material and create the mechanical lock for the Si-HDPE hybrid substrate. The cavity formed by the circular ring has a diameter of Ø22 mm, whereas the depth is automatically adjusted by a spring supporting the ring in accordance with the varying HDPE thickness. A stop bolt was put in

place prevent the circular ring from dislodging itself from the mold. A photograph of the molds are displayed in Figure 3.6.

Figure 3.6: Photographs of fabricated aluminium molds.

3.4 Press molding

A glass molding machine GMP211 (Toshiba Machine Co. Ltd., Japan) was used for the press molding process of the Si-HDPE hybrid substrate. The machine was not equipped with a vacuum system. Instead, it contained a transparent silica glass tube chamber, which holds the purging nitrogen gas during molding. This prevents the oxidation of the molds at high temperatures. The machine structure is illustrated in Figure 3.7. The molds are usually attached to the heat isolator, which is made from ceramic. There is no moving component at the fixed upper mold system. Meanwhile, the lower mold is attached to the lower system of the machine. It has a moving Z-axis, which is moved in the upwards direction (+ve) when the press molding takes place.

The molding temperature can rise to 800 °C with a ±1 °C tolerance level and is monitored by a thermocouple. The pressing force of the machine ranges from 0.2 kN to the maximum of 20 kN with a 0.98 N resolution. An AC servomotor controls the lower mold's movement

accuracy towards the stationary upper mold, with a resolution of 0.1 μm. Figure 3.8 displays the glass molding press machine.

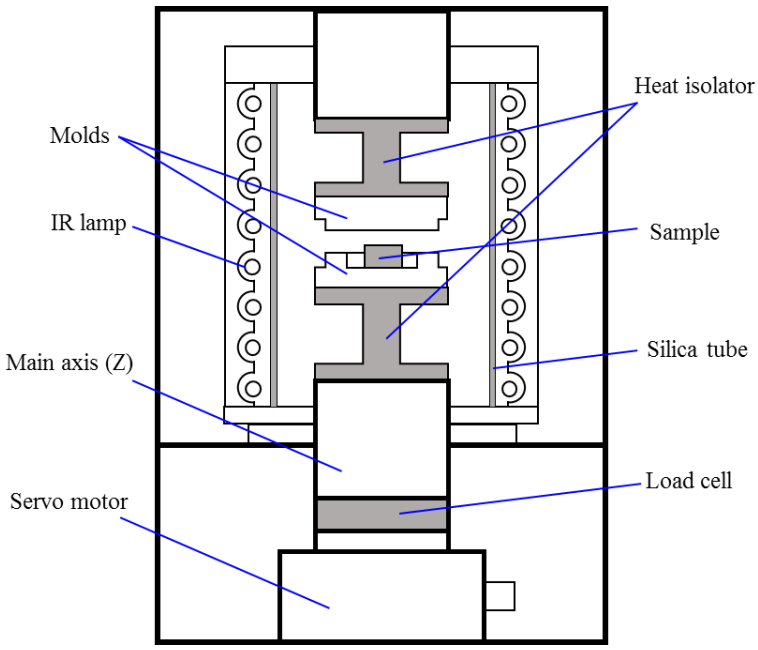

Figure 3.7: Schematic diagram of the glass molding press machine.

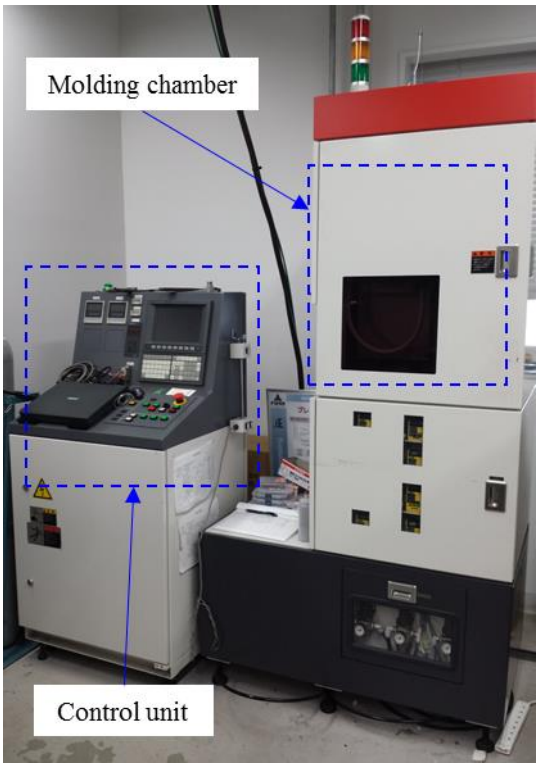

Figure 3.8: Glass molding press machine.

3.4.1 Experimental setup

During the press molding process, a Si substrate is at first placed inside the mold cavity, followed by the HDPE granules, as displayed in Figure 3.9. The lower mold is then raised up towards the upper mold, after which the heating takes place using circular infrared lamps. The pressing process starts when the temperature reaches the melting point of the HDPE, and both the lower and the upper molds are completely closed. The molding process needs to be carried out at the molten state of the HDPE to ensure that the polymer can flow beneath the Si, in order to form the mechanical lock. During the press molding, HDPE would fill into the impression, and laminate one side of the Si substrate. The molds are then cooled down, and the resulting hybrid substrate is removed from the surface of the lower mold.

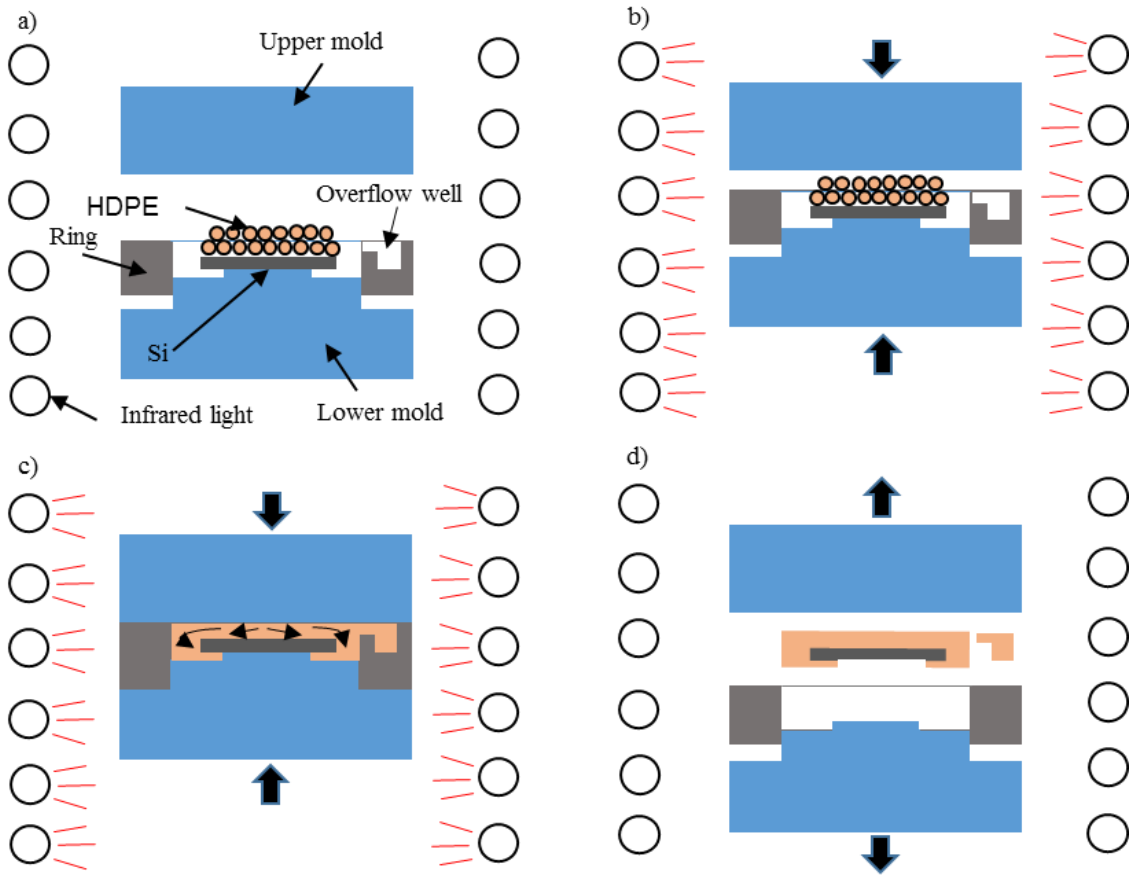

Figure 3.9: Schematic diagram of press molding process: a) material setup, b) heating, c) pressing, and d) cooling and specimen removal.

3.4.2 Molding conditions

During the press molding of the hybrid structure, it is important to eliminate any gaps between the two materials after press molding, as these gap would affect light transmission, in accordance with Snell's law. Light reflection can be characterized by Equation 3.1:

$$n_1 \, Sin \, \theta_1 = n_2 \, Sin \, \theta_2 \tag{3.1}$$

where n_1 and n_2 are the refractive indexes of materials 1 and 2, while θ_1 and θ_2 are the incident and refraction angles, respectively. Leaving a gap between Si and HDPE causes light variance in the hybrid structure. Thus, it affects the image quality of the resulting lens. The effect of light traveling through the hybrid structure with and without a gap are shown in Figure 3.10.

Figure 3.10(a) displays no light diversion between the two substrates, whereas Figure 3.10(b) demonstrates light diversion in the presence of a gap. The focal point of the two-material structures will vary due to the presence of the gap. Therefore, it is crucial to precisely control the pressing force and heating time, in order to eliminate any possible gaps between the Si and the HDPE.

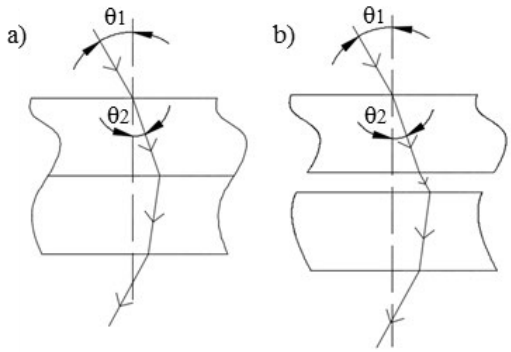

Figure 3.10: Light diversion in a hybrid structure a) without a gap, and b) with a gap.

In this study, the thermal cycle used for making the Si-HDPE hybrid structure is shown in Figure 3.11. It differs from hot embossing, whereby in the latter, the polymer is heated to a

softening state and press. In this experiment, however, the HDPE is heated to the melting state (M_t) followed by the pressing step. The press molding needs to be done in the molten condition of the polymer due to the mechanical lock features that are designed along with the hybrid substrate, as discussed in Section 3.2.

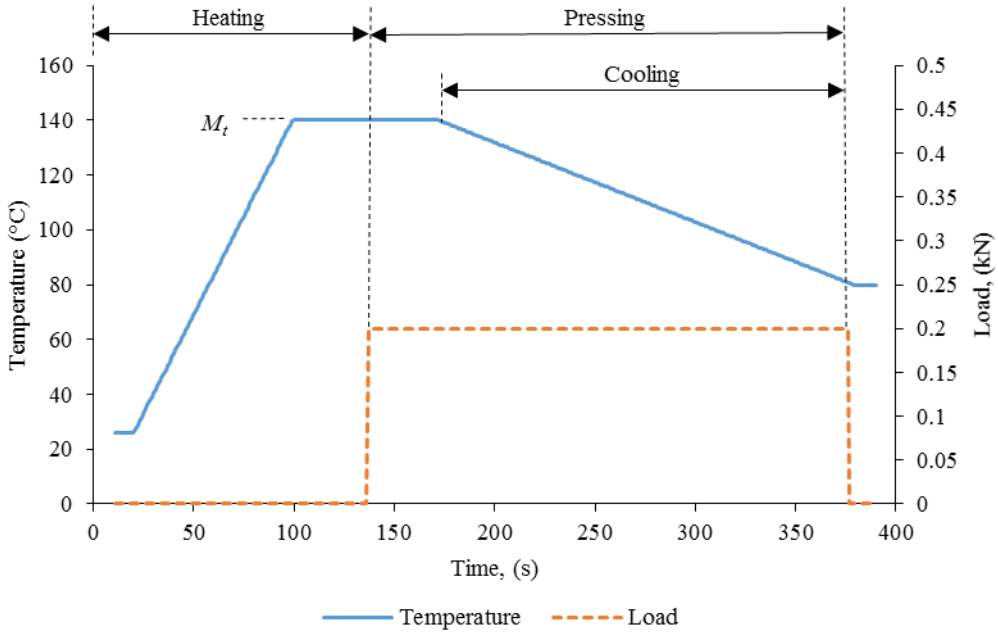

Figure 3.11: Process parameters for the hybrid structure molding press.

By carrying out press molding in molten conditions, the polymer can flow freely, and the mechanical lock will be formed. The experimental steps are described as follows:

(1) The Si substrate is placed into the cavity, followed by the measured volume of HDPE granules. The molding chamber is then closed.

(2) The lower mold is moved towards the fixed upper mold, leaving a gap of 2 mm between the two molds. Nitrogen gas was purged into the chamber for 20 seconds to prevent mold oxidation.

(3) The molds and the specimen were heated from room temperature to 140 °C by an IR lamp heater at a heating rate of 0.6 °C/sec.

(4) The temperature was maintained for 70 s and followed up by the molding press at a minimum pressing force of 0.2 kN. A minimum pressing force was selected to prevent breakage of the Si.

(5) While pressing is continuing, nitrogen gas is purged into the chamber again to cool the mold to 80 °C at a rate of 0.3 °C/sec. The cooling rate here is important to prevent shear deformation at the substrate interface, which affects the adhesion strength.

(6) The mold was opened, and the molded hybrid substrate was discharged for further cooling at room temperature.

3.5 Si-HDPE substrate evaluation

The transmittance measurement was conducted to verify the IR transmittance and absorbance of the hybrid Si-HDPE structure for varying HDPE thicknesses. The IR value of the Si substrate was also measured for comparison. The IR measurement was carried out using a Bruker Fourier Transform Infrared (FTIR) Spectrometer that is capable of measuring at a wavelength range of 2.5 to 25 μm. The sample was placed between the IR source, and the IR detector of the FTIR instrument, as shown in Figure 3.12.

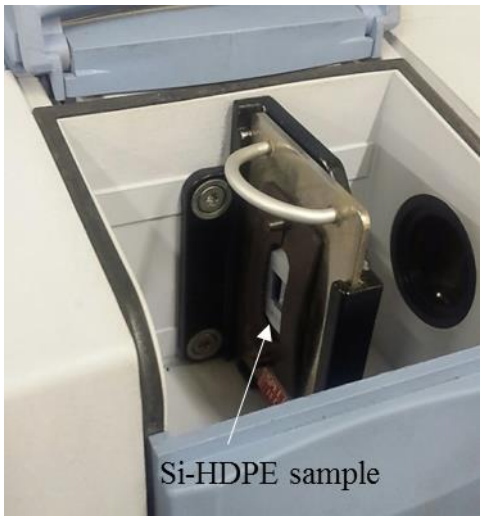

Figure 3.12: Si-HDPE measurement using FTIR measuring instrument.

When measuring the hybrid substrate, the HDPE side was placed facing the IR source while the Si side was facing the detector. This is because, micro lens shapes will be formed on the HDPE side, and it is important to ascertain the particular IR characteristics of the hybrid substrate at this particular orientation.

To measure the IR transmittance of the hybrid substrate, a Beer-Lambert law was applied in the present study, and the equations are as follows:

$$T = \frac{I}{I_0} = e^{-\varepsilon bc} \tag{3.2}$$

where I and I_0 represent intensity and incident radiation, respectively. Meanwhile, ε represents how strong the specimen absorb the light. The path length and molar concentration are represented by b and c, respectively.

3.5.1 Si-HDPE adhesion

A number of press molding tests were performed under various conditions to produce Si-HDPE hybrid substrates with varying thicknesses. It is discovered that at the nominal melting temperature (133 °C), HDPE was not able to stick to the Si substrate firmly. Figure 3.13 displays a photograph of a hybrid substrate pressed at 133 °C after being heated for 70 sec. It is clear that gaps occurred in many regions because the interface bonding was not strongly created between HDPE and Si under this condition. It might also be due to the air trapping that occurs between the two substrates during pressing.

Hence, the molding temperature is set at 140 °C, slightly above the nominal melting temperature, in order to reduce the viscosity of the polymer. Therefore, this temperature was chosen, as it is the maximum recommended temperature and higher temperatures will degrade the polymer.

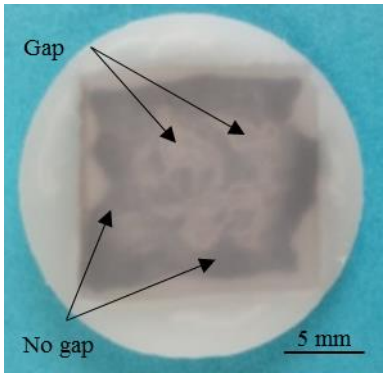

Figure 3.13: Photograph of the Si-HDPE hybrid substrate under melting temperature of 133 °C.

In order to prevent the degradation of the HPDE polymer, the heating time should be set to be as short as possible. In the present molding test, it is discovered that a heating time of 70 seconds was the best. During shorter heating times, such as 50 and 60 seconds, the HPDE did not fully melt and this affected the substrate's adhesion. An insufficient heating time also affects the polymer's flow during molding, leading to the incomplete filling of the mold cavity and the occurrence of flow marks. Photographs in Figure 3.14 demonstrate the effects of heating time on the adhesion and polymer flow.

Figure 3.14(a) displays the flow marks and interface gaps that were formed by the incomplete mixture of HDPE granules, when the heating time was 50 seconds. The flow marks can also be considered as a weld lines due to the HDPE pellets mixing during pressing. The flow marks reduced and interface gaps were eliminated when the heating time was increased by 10 seconds, as shown in Figure 3.14(b). The flow marks were completely eliminated as shown in Figure 3.14(c) when the heating time was set to 70 seconds. Furthermore, strong crosslinking bonding was found to occur between the two substrate interfaces at 140 °C of press molding temperature.

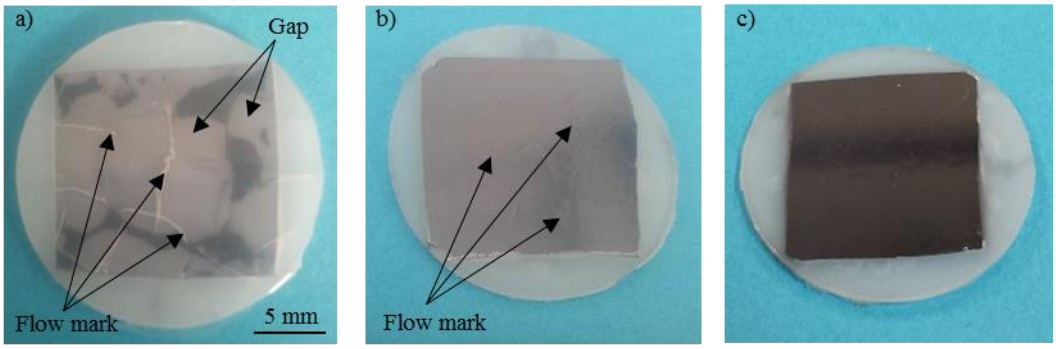

Figure 3.14: Photographs of the Si-HDPE hybrid substrates pressed under different heating times: a) 50 seconds, b) 60 seconds, and c) 70 seconds.

Under optimal press molding conditions, the silane cross-linkable HDPE resin was able to create strong bonding between the two materials and left no gaps at their interface. The mechanical lock designed at the edge of the Si substrate proved to be very useful in holding and protecting the Si substrate. As an example, two finished Si-HDPE hybrid substrates after undergoing the molding press are displayed in Figure 3.15. No gaps nor flow marks are visible, demonstrating the HDPE has uniformly and strongly adhered to the Si substrate.

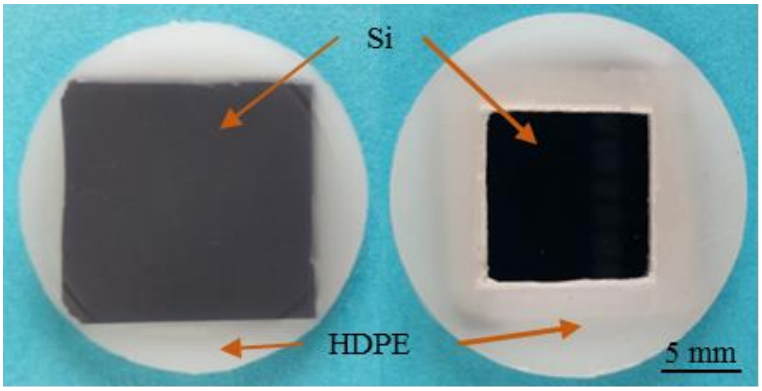

Figure 3.15: Photograph of two pressed HDPE-Si substrates, showing different sides.

3.5.2 Si-HDPE interface phenomenon

An interface phenomenon of the two substrates is the makes for complex defining. As of yet, there is a dearth of experimentally verifiable theories detailing the interface

phenomenon, especially when the interphase involves the adhesion of two different substrates [52].

Nevertheless, in defining the interface phenomenon between Si and HDPE, some theories have been proposed, adsorption, diffusion or interdiffusion, and electrostatic attraction theories. The most popular theories are the adsorption theories founded by Sharpe and Schonhorn, who defined the different materials that will adhere due to intermolecular and interatomic force [53]. According to these theories, the adhesion between the two substrates occurs due to the intimate contact on the surface.

When bonding non-polar material, electrostatic attraction theories should also be considered as mentioned by Yang [54]. In theory, when the two substrates are brought together, the combination forms a capacitor, which charges negative and positive electrical charges as shown in Figure 3.16. A difference of electrical charge causes the attraction force between the two substrates. This model can also be applied to define the interface phenomenon between Si and HDPE, whereby this type of bonding is strengthened by silane.

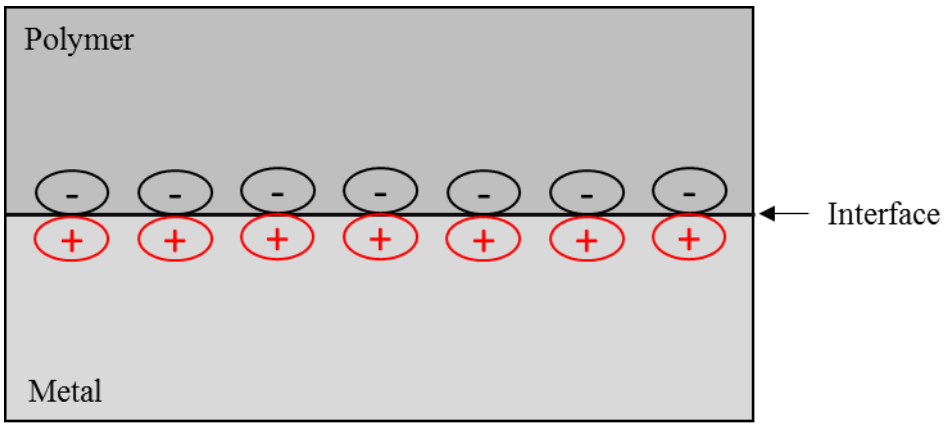

Figure 3.16: Positive and negative charges at the polymer-metal interface.

For this investigation, a cross sectional method is used to observe the interface phenomenon between the two materials. In order to examine the interface between the two materials, the press molded Si-HDPE sample was cross-sectioned using an ion milling machine

(IM4000, Hitachi High-Tech., Co., Japan). This machine is capable of cutting the sample without any flaws, a phenomenon that normally occurs when traditional polishing methods are used. The cross-sectional area of the samples are then analyzed using FE-SEM (SU8020, Hitachi High-Tech. Co., Japan).

Figure 3.17 displays the interface phenomenon between the two substrates. A small gap occurs within the sample under the pressing temperature of 133 °C. Using this temperature, weak bonding occurs between the substrates. This is apparent in Figure 3.18, where stretched HDPE is noticed at the interface phenomenon. The pulling reaction during the mold opening is the reason of the stretched HDPE on the interface. The interface gap between the two substrates might be due to an insufficient press molding temperature. Week bonding occurs because of the air pores during molding, as the press molding is done in a non-vacuum environment. Bikerman and Kinloch have also discovered that air pores will create weak boundary layers on the interface [55,56].

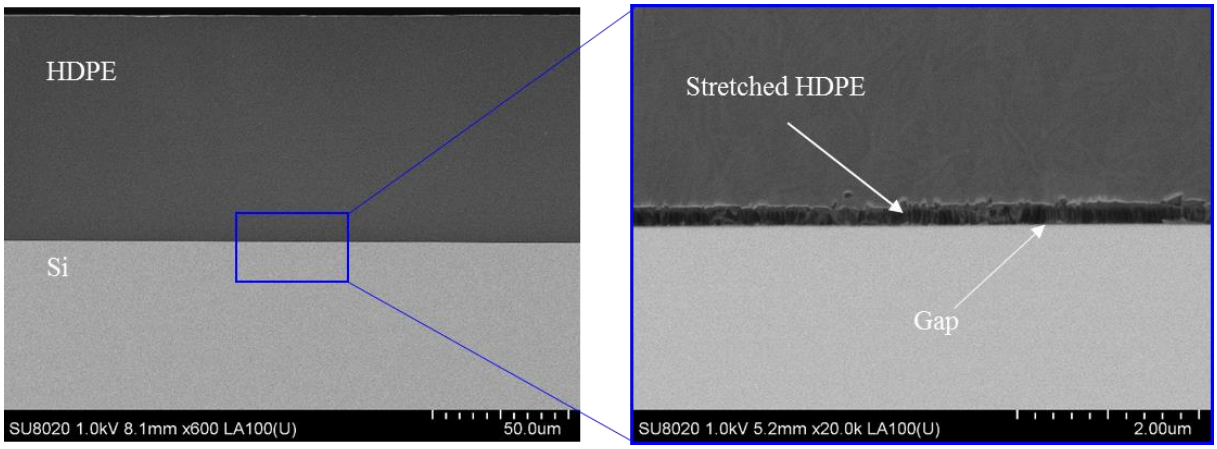

Figure 3.17: Cross-sectional SEM images of the interface of a hybrid substrate formed at 133 °C.

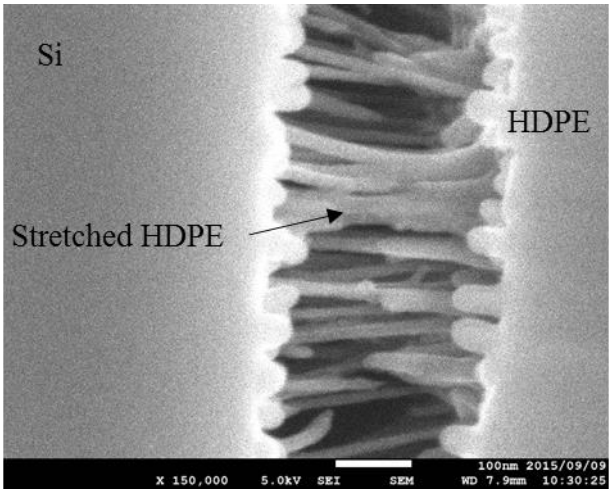

Figure 3.18: Enlarged view of Si-HDPE interface phenomenon showing the stretched HDPE.

Meanwhile, in Figure 3.19, no gap is seen between the two materials. There is also no stretched HDPE noticed at the sample cross-section, and this is displayed in Figure 3.20. It is therefore demonstrated that the hybrid substrates were strongly bonded during the molding press when at 140 °C. At this temperature, the cross-linking between Si and HDPE was successfully achieved, whereby the chemical attraction between the two substrates' was established.

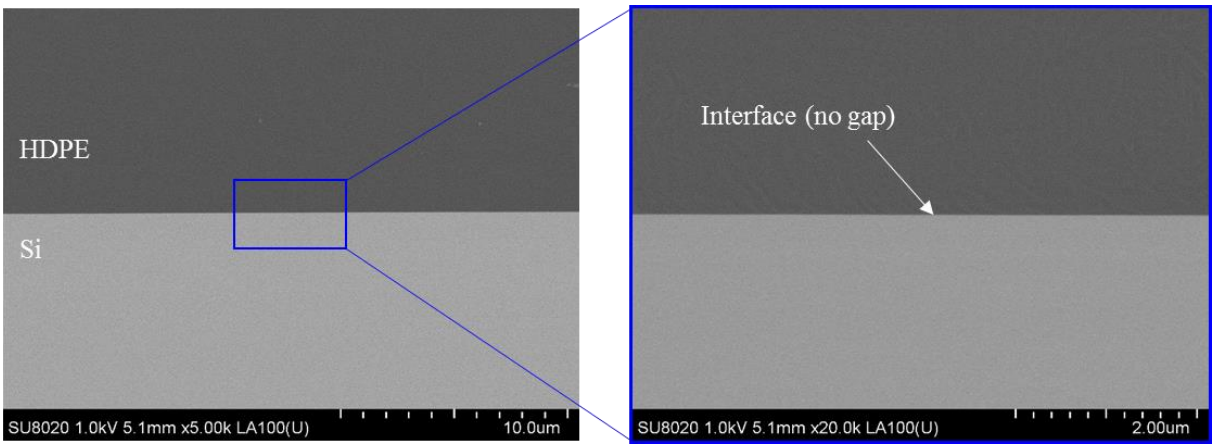

Figure 3.19: Cross-sectional SEM images of the interface of a hybrid substrate formed at 140 °C.

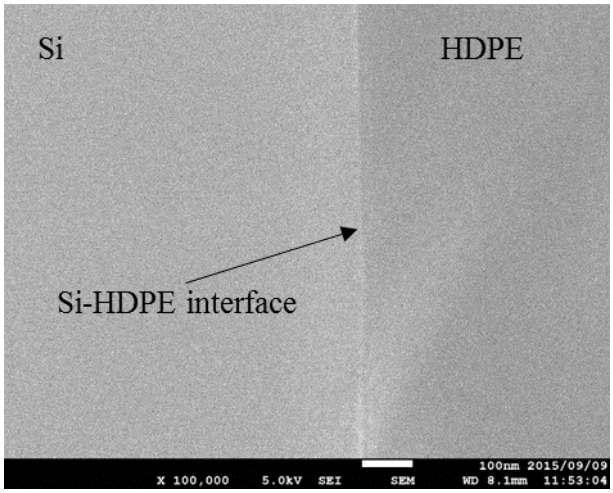

Figure 3.20: Enlarged view of the Si-HDPE interface.

The bonding reaction between Si and HDPE using silane-crosslinking resin, is demonstrated in the schematic diagram in Figure 3.21. The adhesion between the Si and HDPE is due to the silane which act as a coupling agent to improve the adhesion between the two substrates. The silane will react to one side of the polymer and the other side of Si, thus creating the chemical linking at the interface. The adhesion is improved at desired temperature.

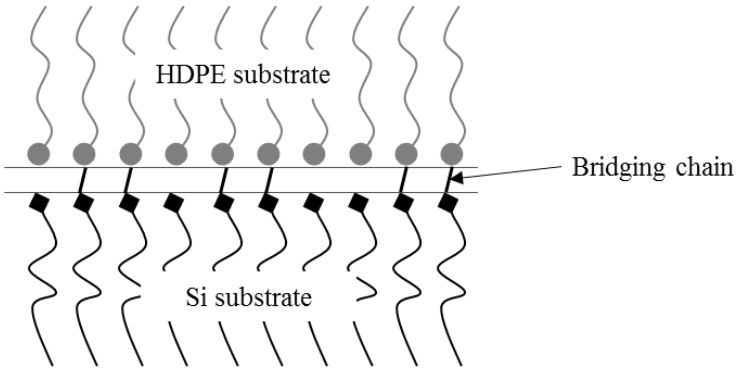

Figure 3.21: Schematic of chemical bonding between substrate.

When the silane was used as coupling agents, the oxane-hydroxyl bonds was formed between the polymer and the Si. The structures of the silane primer are shown in Figure 3.22. From the figure, it can be seen that the silane composed of main elements of oxygen and hydrogen. The oxygen will be bonded to the polymer as an oxane, while the hydrogen will

form hydroxyl bonds on Si. As in Figure 3.18, chemical bridging chains might form at the Si-HDPE interface. The bridging chain creates the adhesion of the HDPE to the Si.

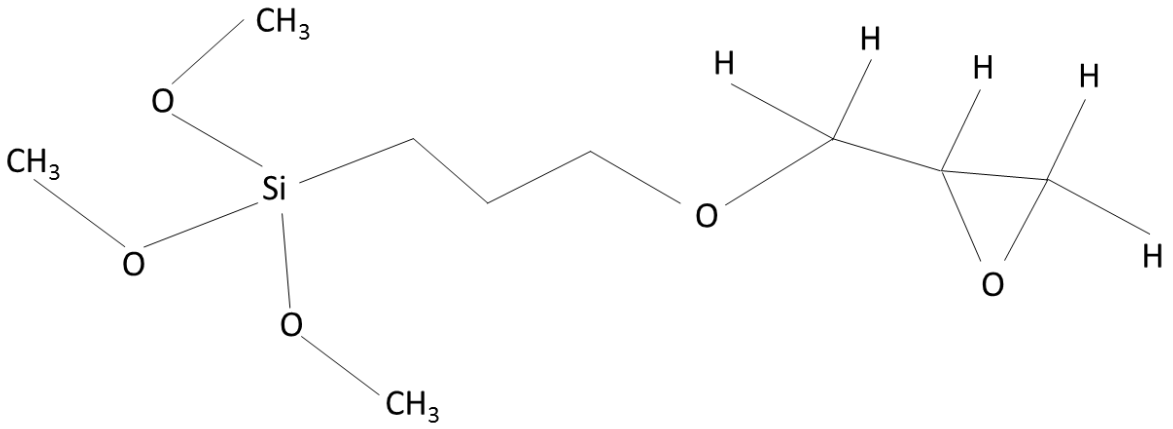

Figure 3.22: Silane primer structures.

According to Yang et. al, diffusion occurs when two macromolecules adhere together during intimate contact, and cause interdiffusion of the macromolecules at the superficial interface layer [54]. The average interpenetration adhesion layer depth (x) can be calculated by following the Fick's law equation:

$$x \propto exp\left(-\frac{E}{2RT}\right)t^{1/2} \tag{3.3}$$

where E is the activation energy of the diffusion, t is the contact time, R is the molar gas constant, and T is the temperature. This model can be used for the adhesions of polymers and also for thermoplastic welding. However, in the case of the HDPE bonding to Si, this theory is not possible due to the lower molding temperature where certain Si substrates will not be evaporated onto the polymeric substrate.

3.5.3 Infrared transmittance

In determining the IR transmittance of the hybrid substrate, the optimum thickness of the HDPE is determined. The HDPE film with varying thicknesses was formed. The IR transmittance of each film was then measured. The IR transmittance of different HDPE thicknesses is illustrated in Figure 3.23.

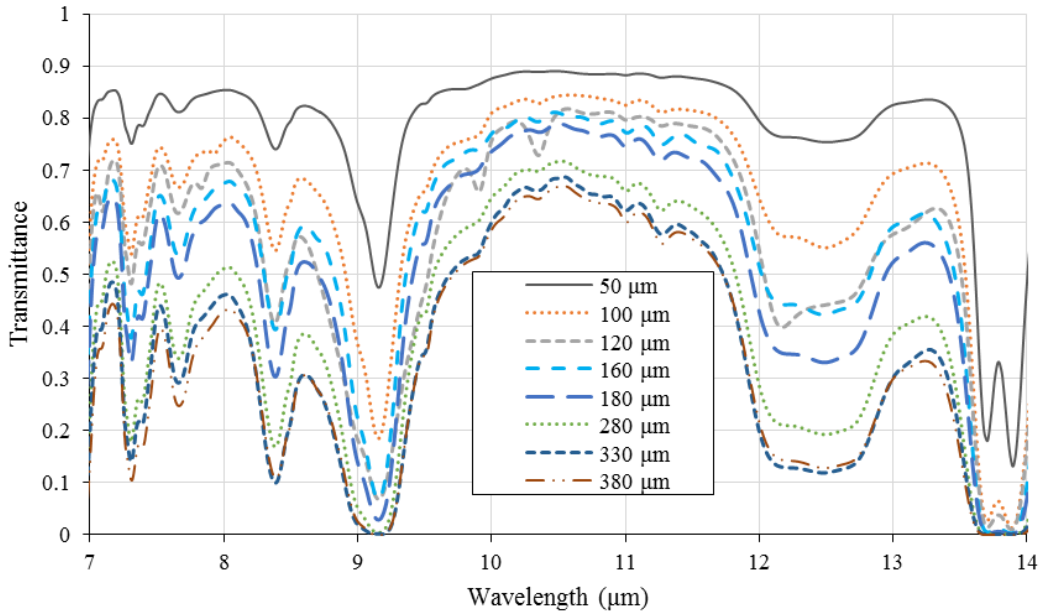

Figure 3.23: HDPE IR transmittance of different varying thicknesses.

From the figures, it is demonstrated that the IR transmittance depends on the HDPE thickness. The HDPE needs to be maintained as thinly as possible, as a thicker HDPE results in lower IR transmittance. For this reasons, a HDPE of around 100 µm or less, in thickness, was selected to laminate one side of the Si substrate.

In fabricating the Si-HDPE hybrid substrate, varying hybrid substrates with different HDPE thicknesses were formed on the Si substrate. The hybrid substrates with four different thicknesses of HDPE, 50, 55, 65, and 115 µm on the Si substrates with the same thickness (755 µm) were then measured using FTIR to investigate the effects of HDPE thickness on IR transmittance and absorbance.

Figure 3.24 displays the transmittance of the hybrid substrates at a range of wavelengths from 7 to 14 µm and is contrasted with the varying thicknesses of Si and HDPE individually. Generally, the IR transmittance was reduced as the thickness of HDPE increased. When the HDPE thickness was increased to 115 µm, the IR transmittance was lower in almost all the wavenumber regions compared to that of the Si substrate. Thus, a successively thick HDPE film is not suitable for use in this study. This phenomenon also concurs with the results illustrated in Figure 3.23, whereby the thicker the HDPE, the lower the transmittance. Furthermore, the transmittance of the Si-HDPE hybrid substrate is especially lower than that of Si in the regions of ~8.8-9.3 µm and ~13.6-14 µm. This phenomenon is due to the higher IR absorbance in this region, which results from the presence of the hydrogen content of the HDPE.

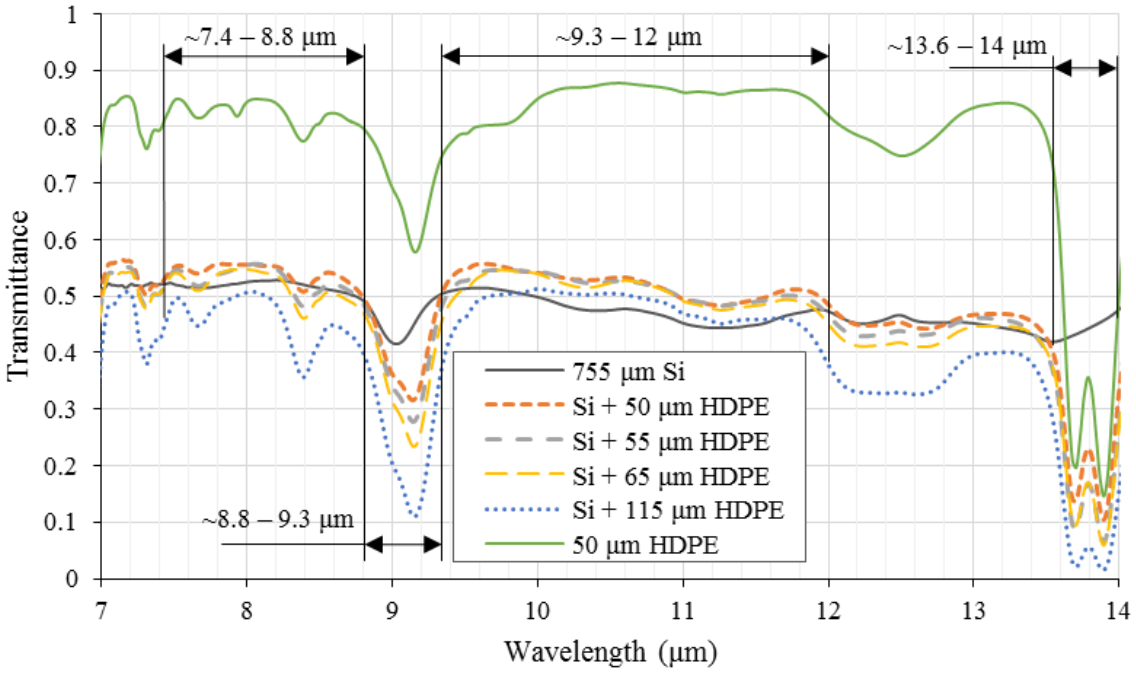

Figure 3.24: IR transmittance of Si, HDPE, and Si-HDPE hybrid substrates with various HDPE thicknesses.

However, it is found that for thinner HDPE films (50 to 65 µm), the hybrid substrate has a higher IR transmittance than that of the Si substrate in some specific wavenumber regions,

such as ~7.4-8.8 μm and ~9.3-12 μm. Arguably, by laminating Si with a thin layer of HDPE polymer, the IR transmittance may be further improved. This phenomenon is due to the HDPE layer itself being able to reduce the reflection of light at the substrates' surface, much like an anti-reflection film [57]. In the reflective coating of the optical material, a lower refractive index of material was required. Hence, HDPE becomes the anti-reflective coating of the Si substrate due to the higher refractive index of the Si substrate.

Meanwhile, the Si substrate itself has a reflection of around 30%. Therefore laminating it with low refractive index materials would reduce its reflectance. The reflectance (r) of the Si without the HDPE layer can be calculated by the following equation:

$$r = \left(\frac{n_{air} - n_s}{n_{air} + n_s}\right)^2 \tag{3.4}$$

where n_{air} represents the refractive index of air and n_s is the refractive index of the substrate. The reflectance of the hybrid substrate can be calculated using the following equation, whereby the refractive index of the coating substrate (n_2) is included in the calculation:

$$r = \left(\frac{n_{air}n_s - n_2}{n_{air}n_s + n_2}\right)^2 \tag{3.5}$$

The IR transmittance of the hybrid structure is higher, especially in regions ~7.4-8.8 μm and ~9.3-12 μm because the IR transmittance of the HDPE itself is higher in those regions than in other regions, as demonstrated in Figure 3.23. Although the total IR transmittance of the Si-HDPE hybrid substrate is lower than that of HDPE alone, the shape of the IR transmittance curve is effectively maintained. Meanwhile, the transmittance of the Si itself also found out to have lower transmittance at ~9 μm of IR region which might be also due to the hydrogen contents, especially at the polished surface. The Si is etched with the hydrofluoric (HF) for 10 and 30 minutes and the results are presented in Figure 3.25. From the figure, it

showed that the transmittance was slightly increased, which might due to the hydrogen content removal from the Si surface. However, due to very small difference, the result is neglected.

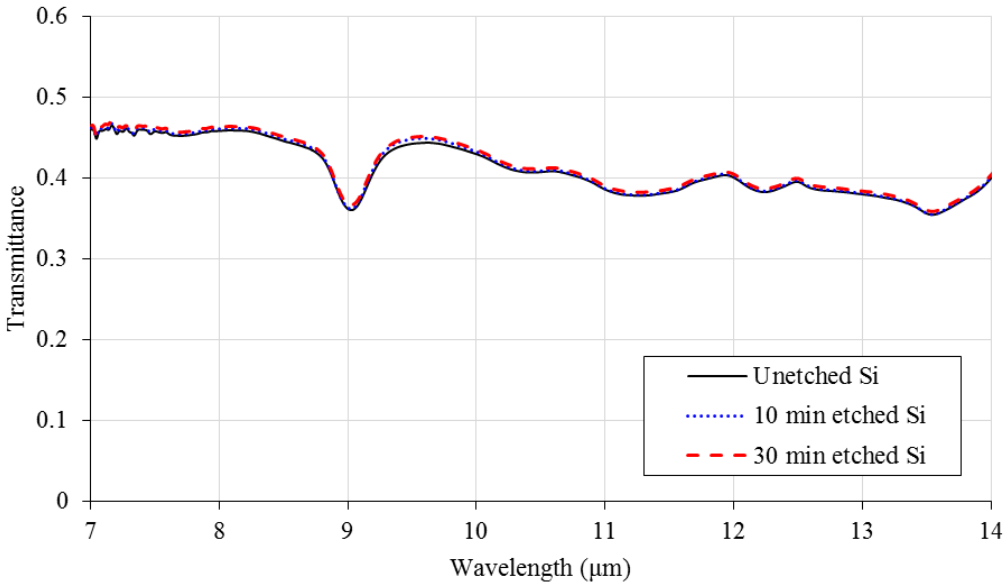

Figure 3.25: IR transmittance of Si etched with HF.

To estimate the transmittance of the hybrid substrate, the reflectance of each substrate needs to be calculated first using Equation 3.4. The following equation (Eq. 3.6) can be used to calculate the estimate transmittance:

$$T_t = T - R_1 - R_2 \tag{3.6}$$

where T is the transmittance, R_1 is the reflectance at the HDPE surface, and R_2 is the reflectance at the Si substrate's surface.

Meanwhile, the IR absorbance (A) of the Si-HDPE hybrid substrate can be calculated by using the following equations:

$$A = 1 - T \tag{3.7}$$

where T is the IR transmittance.

As the increasing of the HDPE thickness reduces the IR transmittance, it might limit the laminating process to only one side of the Si. Laminating both sides of Si will also increase the thickness of the HDPE in total. A trial has been made to laminate both surfaces of the Si, as displayed in Figure 3.26. The lamination process is done by inserting the HDPE pellets at first into the mold cavity. The Si is then placed on the HDPE pellets. Lastly, another pellets were placed on top of the Si. In this way, the Si is sandwiched in between the HDPE resin before the molding process. All the substrates are then heated and pressed. Finally, the two-sided laminated Si with HDPE was obtained after the press molding process.

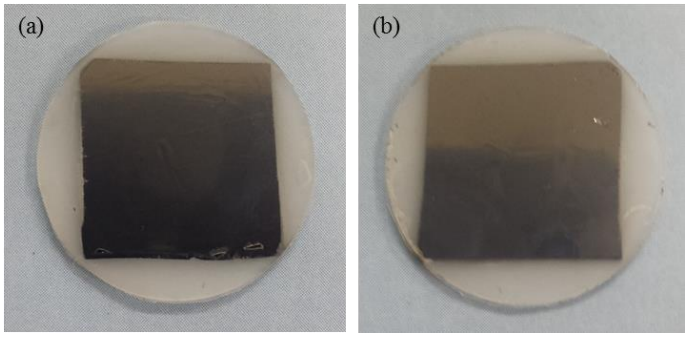

Figure 3.26: Photograph of two side laminated Si-HDPE hybrid substrates, showing different sides.

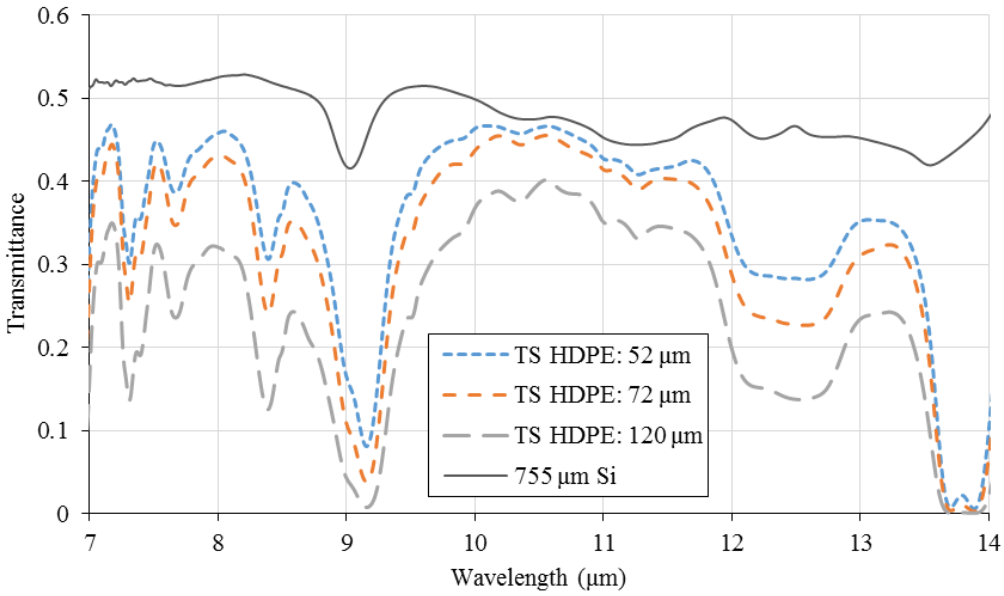

Figure 3.27: IR transmittance of two side (TS) laminated Si with different varying HDPE thicknesses.

The result of IR transmittance of the Si-HDPE hybrid substrate with both sides of Si laminated by HDPE is shown in Figure 3.27. From the results, it can be seen that the IR transmittance was reduced at all IR regions. Accordingly, experimental results demonstrated that the Si can only be laminated on only one side. This augurs with the theory that laminating both sides of Si will increase the HDPE thickness, thus reducing the IR transmittance.

To evaluate the influence of the interface gap between the two materials on the IR transmittance, a measurement was done, and the results are presented in Figure 3.28. The sample used in the measurement has a HDPE layer thickness of 330 µm on the Si substrate and the gap width between them was 10 µm. In Figure 3.28, there is a significant loss of transmittance in all regions due to light diversion at the gap. These results corroborate Snell's law as mentioned in Section 3.4.2. The results again demonstrate the importance of fabricating the hybrid substrate without leaving any gap to prevent the losses of IR transmittance.

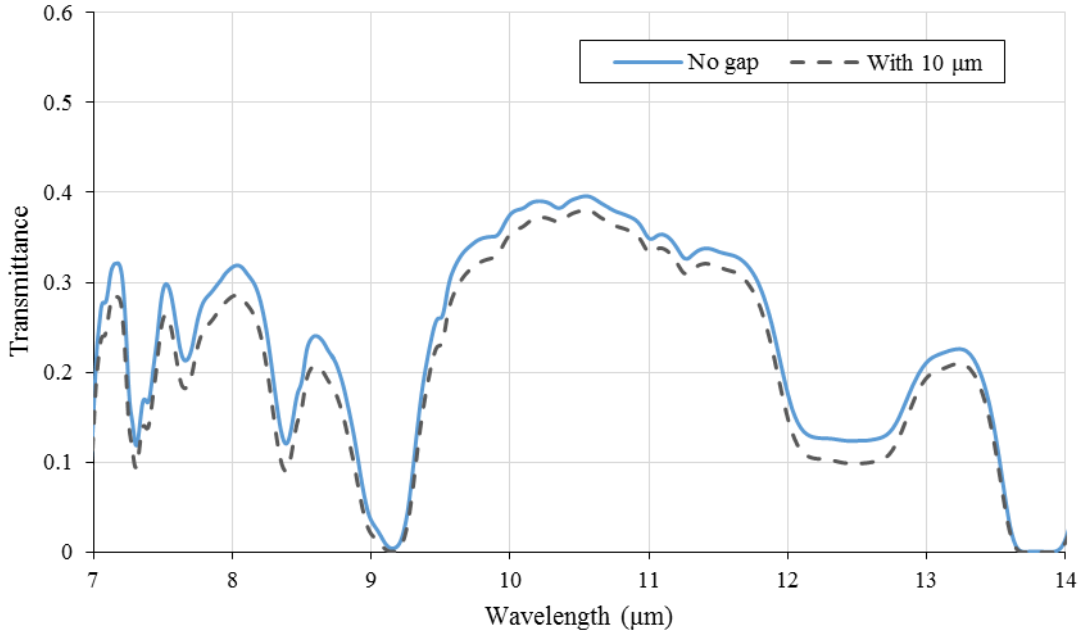

Figure 3.28: Effect of an interface gap on the IR transmittance of a hybrid substrate.

The press molding temperature is another important factor in polymer formation, as high temperature degrades the polymer property and affect the IR transmittance. High

temperatures may also result in the material being burned or degraded. To examine the effect of molding temperature on the IR transmittance, two Si-HDPE hybrid substrates molded at 140 and 200 °C, respectively, were each used for evaluation. Figure 3.29 displays the effect of temperature on IR performance. Here, the thickness of HDPE was 60 µm. It is clear that the IR transmittance was reduced significantly due to the degradation of the polymer at 200 °C. Therefore, it is important to use lower molding temperatures for a shorter period, to prevent the HDPE polymer from degrading during the press molding of the hybrid substrates.

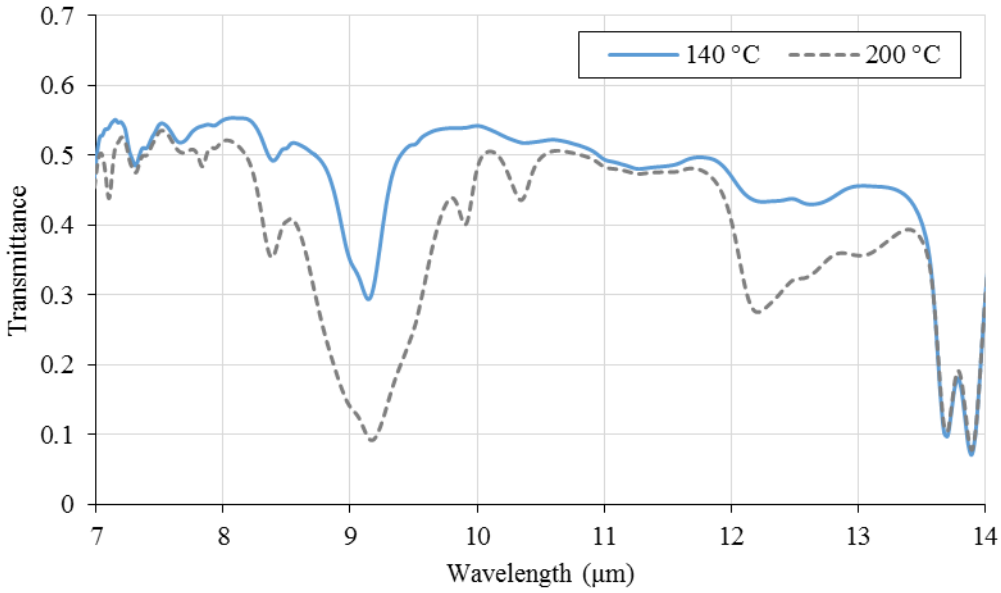

Figure 3.29: Effect of molding temperature on the IR transmittance.

3.6 Optical evaluation

3.6.1 Optical evaluation setup

IR images were captured using the Therm-App smartphone thermal camera (Opgal Optronic Industries Ltd.) with a resolution of 384 × 288 pixels. The spectrum range of the camera is for the long wave IR region from 7 to 14 µm and is supplied with a 19 mm focal length germanium lens. The camera was connected to an android smartphone to operating the

camera and to process the images. The setup for the image capturing is displayed in Figure 3.30.

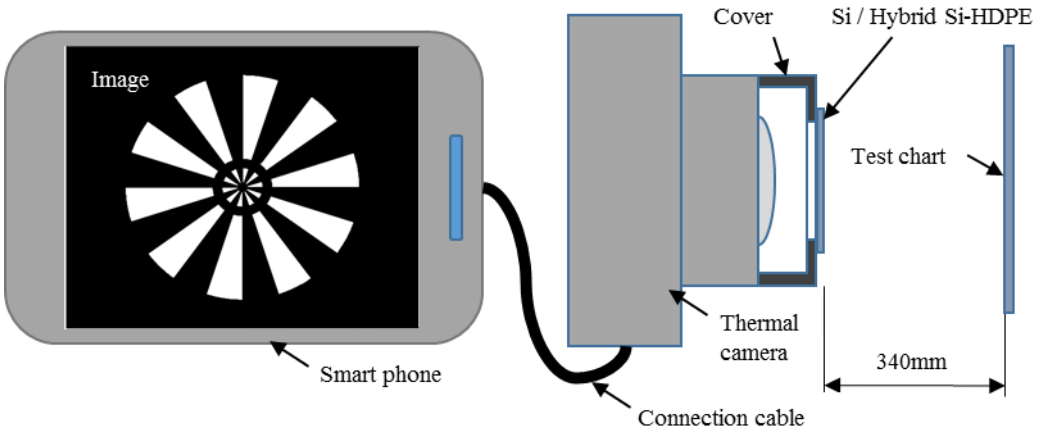

Figure 3.30: Camera setup with image chart for optical performance evaluations.

In order to capture the images of objects with varying materials and thicknesses, a cover with a Ø12 mm hole was placed in front of the camera lens. The Si-HDPE hybrid substrates were then placed at the hole, and a grayscale image was captured at a distance of 340 mm away. The object used for the imaging was a fan blade-shaped chart printed in black and white, on a piece of paper. The size of this chart is 100 mm × 120 mm and is composed of small and big fan shapes, which is used to evaluate the sharpness of the image. The small fan section was used to evaluate the smaller images whereas the big fan section evaluated the larger images. The sharpness of each captured image was analyzed with ImageJ software to measure the edge sharpness of each individual image.

3.6.2 Optical evaluation

Several evaluation methods were conducted to ascertain the optical capabilities of the Si-HDPE, with the aim of confirming that the hybrid substrate meets the standards of an IR lens. The evaluation comprised of three categories, namely the image chart, the image sharpness measurement, and the night mode imaging.

3.6.2.1. Image evaluation using chart

Figure 3.31 displays thermal images of the Si-HDPE hybrid substrates with varying film thicknesses at a resolution of 384 × 288 pixels. As reference, Figure 3.31(a) displays the grayscale image of the chart captured sans filter. When a 755 µm Si substrate was placed in front of the camera, the image became darker, and the contrast of the image was lower, as shown in Figure 3.31(b). This is caused by the reduced IR transmittance, due to the Si substrate being used. In this case, the small fan shape is still identifiable at the centre of the chart, along with the bigger fan shape. The image of the hybrid substrate with 50 µm HDPE in Figure 3.31(c) shows almost no difference compared to that in Figure 3.31(b).

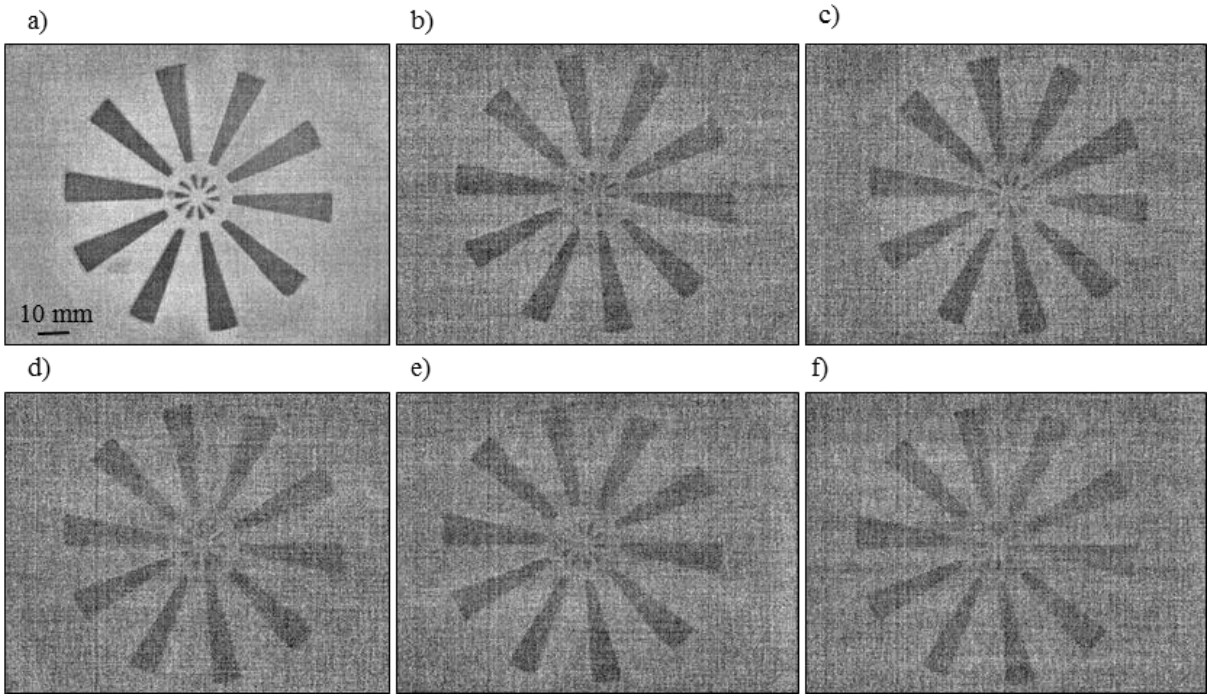

Figure 3.31: IR images without filter and images for different substrates: b) 755 µm Si, c) 50 µm HDPE + 755 µm Si, d) 65 µm HDPE + 755 µm Si, d) 75 µm HDPE + 755 µm Si, and f) 155 µm HDPE + 755 µm Si.

Compared to Figure 3.31(b), the shape of the small fan in Figure 3.31(c) appears more clearly, demonstrating that the IR transmittance and image quality of the hybrid lens is of an acceptable standard. As per Figure 3.24, i.e., a thin layer of HDPE applied to Si improves

transmittance of the IR light. Figure 3.31(d) displays the image when the HDPE thickness was increased to 65 μm. The image becomes dull and blur, especially where the small fan profile starts to lose its shape. This is due to an increase of the IR light absorption with the corresponding increment of the HDPE thickness. Figure 3.31(e) and (f) are the results obtained when the HDPE thickness was 75 μm and 155 μm, respectively. The images of the chart at these thicknesses become duller, whereby the small fan shape is hard to identify.

From these results, a strong dependence of image quality on the HDPE thickness is confirmed. In order to produce a clear image, the hybrid lens requires the HDPE film to be thinner than 100 μm. Under the present experimental conditions, a HDPE thickness of ~50 μm is found to be most suitable for the hybrid lens.

3.6.2.2. Image sharpness evaluation

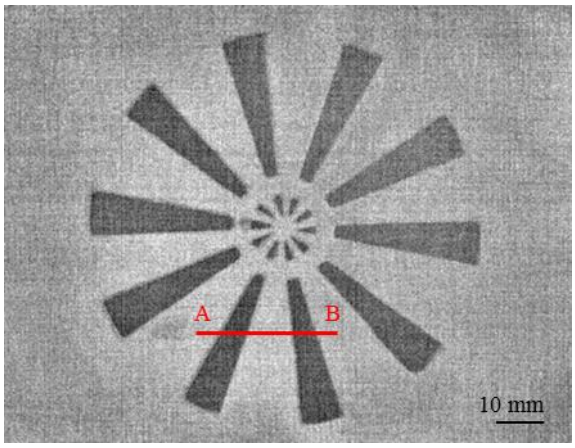

Figure 3.32: Image cross section for edge sharpness measurement.

ImageJ software was used to analyze the grayscale images obtained from the IR camera, by differentiating the gray values and the pixilation of the image, as presented in Figure 3.31. It was discovered that darker pixels result in a lower gray value. The distance between the image chart and the thermal camera was set to 340 mm. A key assumption made was that all the images have the same light illumination. As showed in Figure 3.32, a cross sections of the

images were made in areas indicated by the line A-B, and then the gray values were plotted in Figure 3.33.

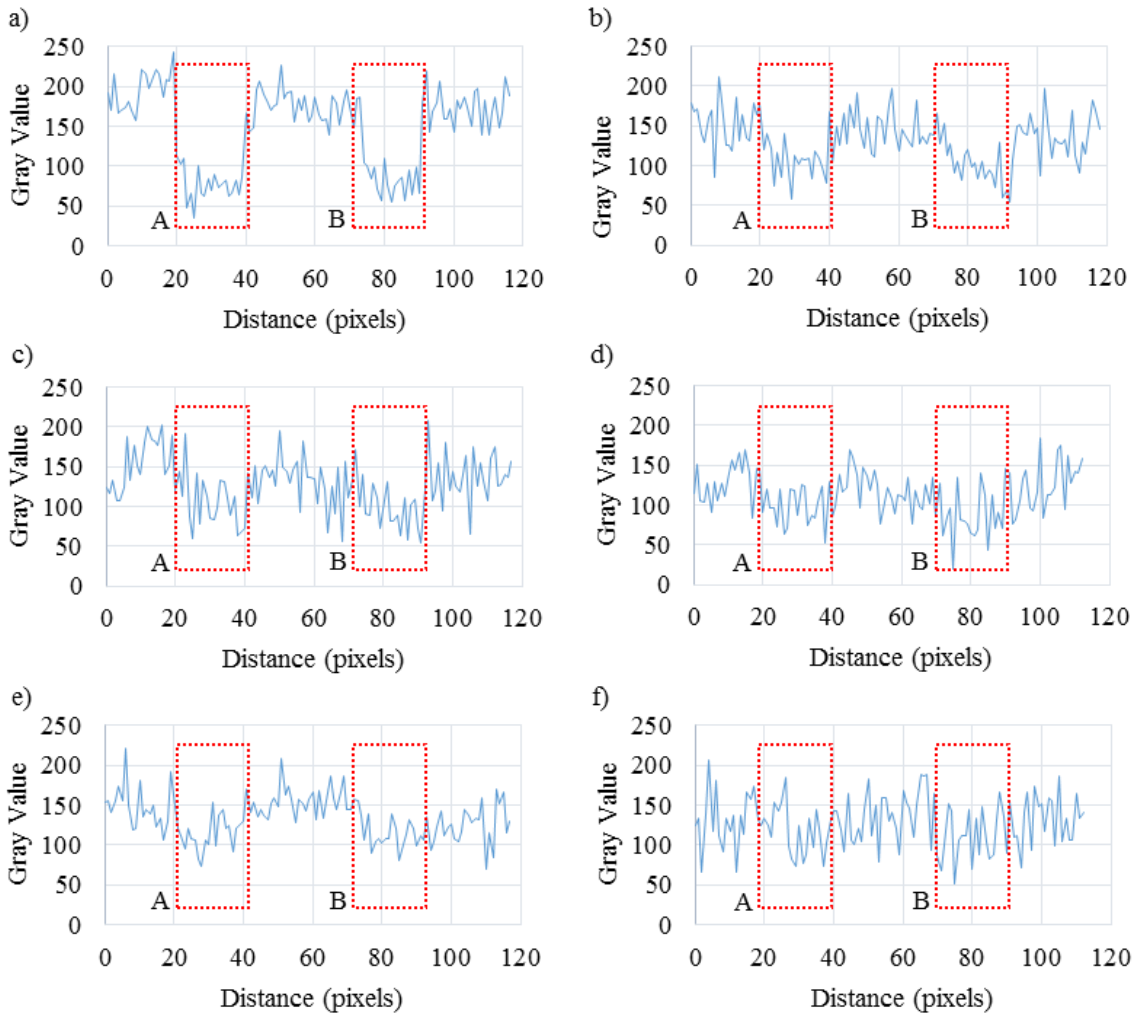

Figure 3.33: Image edge sharpness measurement: a) without filter, b) 755 µm Si, c) 50 µm HDPE + 755 µm Si, d) 65 µm HDPE + 755 µm Si, e) 75 µm HDPE + 755 µm Si, f) 155 µm HDPE + 755 µm Si.

As presented in Figure 3.33(a), when no filter is used, a sharp step is clearly identified at the edge of the image. The step height became smaller when a Si substrate (Fig. 3.33(b)) and Si-HDPE hybrid lenses (Fig.3.33 (c-f)) were placed in front of the camera. A dark image produces more noise. The noise level depends on the thickness of the HDPE. When a 50 µm HDPE was added to the Si substrate to form the hybrid lens (Fig.3.33 (c)), the resulting image edge sharpness is similar to that of the Si substrate only (Fig.3.33 (b)). For a very thick HDPE

film (115 μm), the edge of the image is hard to identify, as shown in Figure 3.33(f). In summary, the gray value of each Si-HDPE image cross section is plotted in Figure 3.34. A clear relationship exists between the gray value and the HDPE thickness. Therefore, the gray value increases with the increase of the HDPE thickness that laminates the Si substrate.

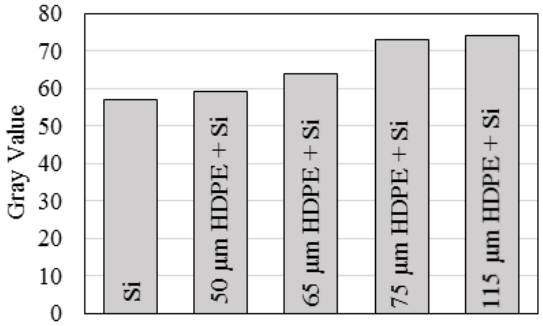

Figure 3.34: HDPE thickness effect on the image's gray value.

3.6.2.3. Night mode imaging evaluation

The grayscale image of a human face was captured using the 'night mode' setting, at the distance of 1 m to demonstrate the ability of the hybrid substrate to be used as the material for night vision infrared lenses. Figure 3.35(a) displays the image captured when the thermal camera was filtered by the 755 μm Si substrate, whereas Figure 3.35(b) displays the image filtered by a hybrid substrate with 50 μm HDPE. There is no significant difference between the two images. Therefore, results concur with the chart imaging evaluation as discussed in Figure 3.31, as well as the grey value measurement in Figure 3.33, whereby the thinner Si-HDPE substrate results in image qualities as good as when only Si is used.

In addition, an IR image utilizing only the HDPE filter was also done to compare image quality. In this imaging evaluation, 620 μm of HDPE was selected, and the image is presented in Figure 3.36. It is observed that the image becomes a blur, even though the thickness of HDPE is less than that of the 805 μm Si-HDPE hybrid substrate as discuss in Figure 3.35. This is due to the fact that HDPE has a lower IR transmittance, especially when it is successively thick.

Therefore, the Si-HDPE hybrid substrate can produce better image quality as compared to HDPE on its own.

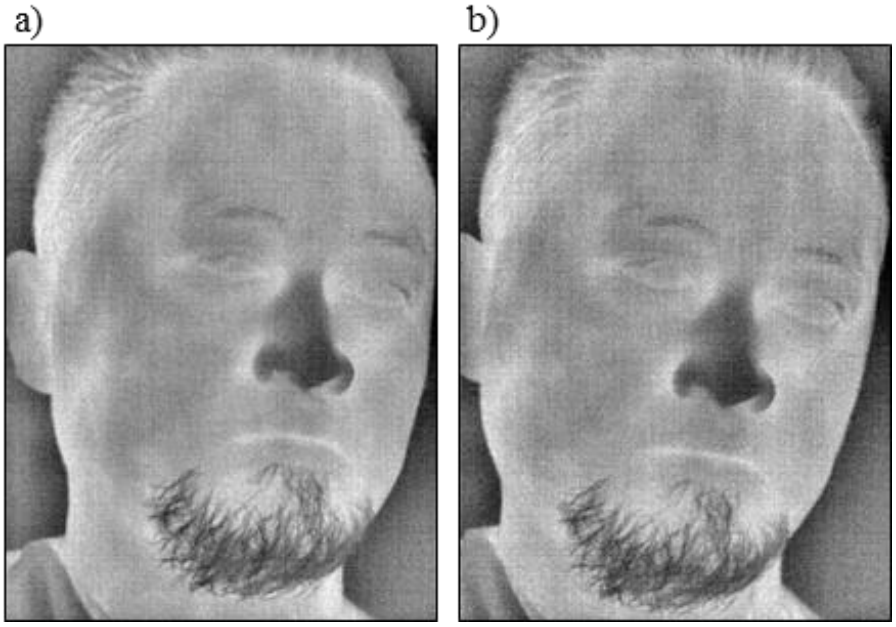

Figure 3.35: Night mode images obtained by different lens substrates: a) 755 μm Si, and b) 50 μm HDPE + 755 μm Si.

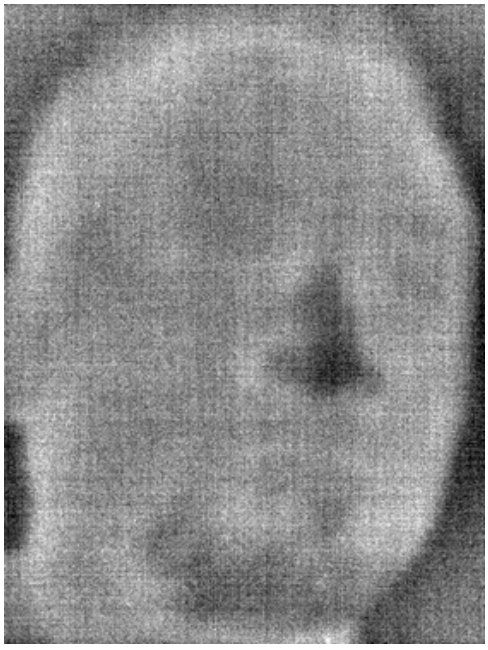

Figure 3.36: Night mode images obtained by 620 μm thick HDPE.

3.7 Chapter summary

Si-HDPE hybrid substrates have been manufactured using the press molding method. The IR optical properties of the fabricated substrates were then evaluated. The following conclusions are obtained:

1. Fabrication of the Si-HDPE hybrid substrates can been successfully performed via the press molding method. A set of molds were designed and fabricated, enabling high-precision forming of the Si-HDPE hybrid structures with mechanical locks.
2. The effects of some key factors in the press molding process, such as a molding temperature and heating time, were investigated. It is possible to create a strong adhesion of the two materials without leaving any interface gaps.
3. The Si-HDPE hybrid substrate has higher IR transmittance in wavenumber regions of ~7.4-8.8 μm and ~9.3-12 μm than that of Si substrate only. This interesting phenomenon is due to the HDPE itself acting as an anti-reflection coating for the Si substrate.
4. A successively thicker HDPE laminating reduces the image sharpness and IR transmittance. A Si substrate laminated with ~50 μm of HDPE, is able to produce images of the same image quality as that of Si on its own. Furthermore, the laminated hybrid substrate has improved the IR transmittance.

Therefore, the fabricated Si-HDPE hybrid lens substrates are usable for night mode IR imaging with satisfactory image quality.

CHAPTER 4

Microstructure forming on Si-HDPE substrate

In this chapter, microstructures were designed and fabricated on the HDPE layer of the Si-HDPE substrate. The microstructures consist of a micro lens, which is formed on an extremely thin polymer, mainly to actualize the use of Si-HDPE hybrid lens for IR application. Some issues during the fabrication will be investigated in this study, and the fabrication process will utilize press molding process as previously used in fabricating the Si-HDPE substrate.

In this study, two different lens designs or microstructures were selected. The first design was the micro-lens array, while the second design was the Fresnel lens. These two-lens design can be used for various IR applications. The micro lenses were selected due to the limited thickness of the HDPE layer of the Si-HDPE hybrid substrate. The HDPE layer needs to be formed on Si as thinly as possible to ensure that the IR transmittance of the hybrid substrate is within specifications.

4.1 Micro lens array

For the first micro lens fabrication study, a microstructure on the HDPE layer of the hybrid substrate was designed. The design of the microstructure consists of a plano-convex micro lens array. The moth-eye shape of the lens was designed to test the possibility of fabricating micro structured IR optics. The moth-eye shape lens design could be beneficial as the lens for IR application sensors. Furthermore, this shape may help miniaturize the imaging systems [58,59].

4.1.1 Micro lens array design

A plano-convex micro lens array with a Si-HDPE hybrid structure was designed as shown schematically in Figure 4.1. The lens curvature radius was 10 mm, the diameter 2 mm, and the sag height 46 μm. The total diameter of the lens area was 22 mm, and the formed area of the lens was 15 mm in diameter. The lens array parameters are detailed in Table 4.1. As per prior research in fabricating the Si-HDPE hybrid substrate, a mechanical lock was used to surround the Si edges, in order to improve the strength of the hybrid structure.

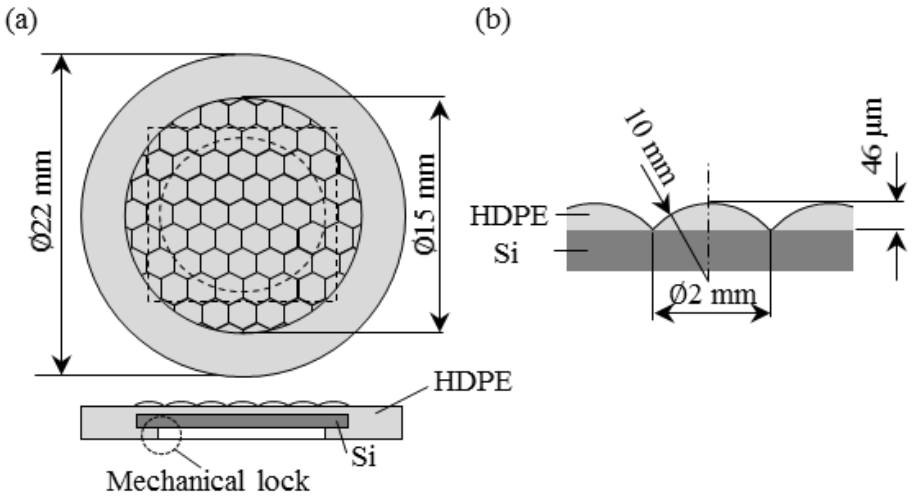

Figure 4.1: Schematic diagram of: (a) Si-HDPE hybrid lens array design, and (b) lens cross section.

Table 4.1: Plano-convex lens array design parameters.

Parameters	Value
Lens radius (R), mm	10
Lens pitch, mm	1.73
Lens height (H), μm	46
Lens diameter (D), mm	2
Total number of lens	61

4.1.2 Mold design and fabrication

In the present research, the upper mold comprised of two different designs. The first design did not include a plunger whereas the second design included it. The effectiveness of the different upper mold designs were compared in the experiments. The lower mold is fitted with an outer ring which functions as a mold cavity which holds the HDPE polymer during the molding process. However, the lower mold design is made differently from the lower mold design used in the previous experiment, when the Si-HDPE substrate was fabricated. Specifically, the ring of the lower mold is not attached to any spring or stripper bolt.

4.1.2.1. Mold without plunger

In the experiment, the first design of the upper mold, i.e. without the plunger features was fabricated. The outer surface of the lens array was flat, and at the same level with the lens array, as showed in Figure 4.2(a). The schematic diagram of the mold assembly is presented in Figure 4.2(b). The outer diameter of the upper mold is roughly the same as the diameter of the ring of the lower mold.

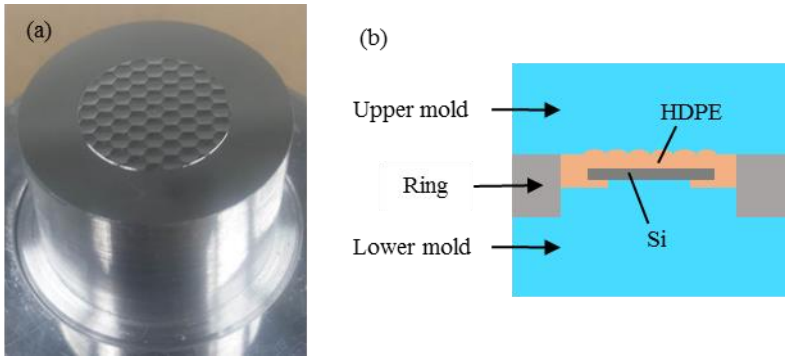

Figure 4.2: Upper mold design without plunger.

4.1.2.2. Mold with plunger

For the second upper mold design, a plunger feature was included and fabricated. The plunger diameter was set to be same as the lower mold cavity diameter, whereas the plunger

length is 2 mm. During the press molding, the plunger is plunged into the mold cavity, thus increasing cavity pressure. The plunger design of the upper mold is illustrated in Figure 4.3(a).

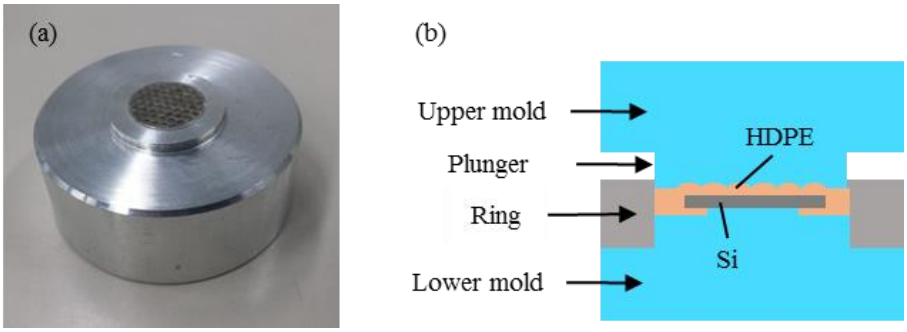

Figure 4.3: Upper mold design with plunger.

4.1.2.3. Lens array machining

The micro-lens array shapes were machined on an aluminium (Al) mold insert using an ultraprecision diamond lathe, NanoForm X (Ametech Inc., USA). The lathe is equipped with an air bearing spindle. A single crystalline diamond tool with a nose radius of 250 μm was selected for the micro-cutting process. A constant spindle speed of 2700 rpm was used to roughly cut the surface with an 18 mm/min feed rate and a rough-cut depth of 20 μm. The spindle speed was unchanged for the finishing cut. However, the depth of cut was reduced to 4 μm while the feed rate was slowed down to 3.6 mm/min.

A photograph of the mold insert and its three-dimensional topography are shown in Figure 4.4(a) and (b), respectively. Figure 4.5 shows a plot of form error distribution of a lens array, which is calculated by comparing the measured cross-sectional profile with the ideal lens profile. The peak-to-valley of form error was approximately 98 nm. Meanwhile, the surface roughness of the lens array of the mold was 3.3 nm Ra.

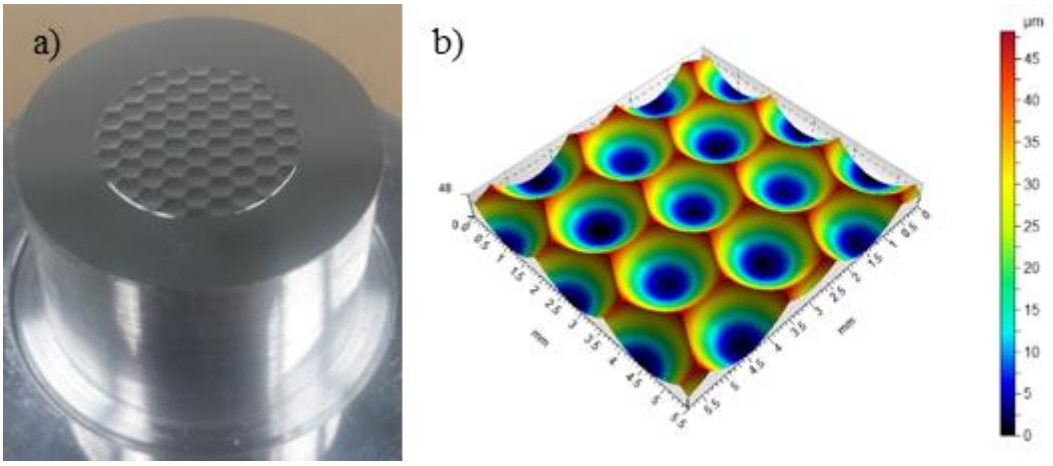

Figure 4.4: Photograph of (a) an aluminum mold insert with micro-lens array, and (b) three-dimensional topography of the mold.

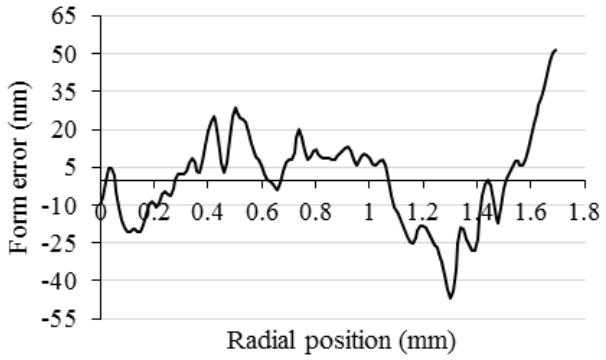

Figure 4.5: Form error profile of a micro-lens dimple on the mold insert

4.1.3 Press molding of micro lens array

To fabricate the micro-lens array of the Si-HDPE hybrid lens, a press molding process was used, where the process was similar to the press molding of the Si-HDPE hybrid substrate. During the press molding process, the optimum parameters of the process are decided. Same with the press molding of Si-HDPE hybrid substrate, the press molding of the micro lens array was also done in the molten state of the HDPE. The press molding in the molten state of the polymer will ensure that the HDPE can flow beneath the Si to form a mechanical lock for improving the Si-HDPE adhesion.

4.1.3.1. Molding conditions

In the experiments, the isothermal molding process used once again [60], and two different melting temperatures were used, 133 and 140 °C respectively. A temperature higher than 140 °C is not suitable because it will degrade the polymer and affect the IR properties [61]. A temperature of 133 °C has been selected again in this experiment even though it has been used during the Si-HDPE substrate fabrication, and showed weak bonding between Si and HDPE. This study attempts to demonstrate the effectiveness of selecting this temperature during the lens array forming.

The pressing forces used in the experiment were 0.2, 0.4, and 0.6 kN respectively. As the pressing force used during the Si-HDPE hybrid substrate press molding was kept to the minimum, it also needs to be kept at minimum during the press molding of the lens array. Primarily, this is to prevent the Si from the breakage during the press molding process.

The sag height of the lens for different molding conditions will be compared to determine the best molding process parameters. The surface of the lenses and coating were also examined. The molding experimental steps are described as follows:

1. Si substrate and a measured volume of HDPE pellets are placed into the mold cavity. The molding chamber is then closed.
2. The lower mold is raised closer to the stationary upper mold. A 2 mm gap is set between the two molds to enhance the heating process. To prevent mold oxidation during heating, the chamber is purged with nitrogen gas for 20 s.
3. Both the molds and the specimen are heated with an IR lamp from room temperature to the molding temperature (133 or140 °C) at a heating rate of approximately 0.6 °C /s.
4. The temperature is then maintained for 70 s, followed by the press molding until the mold is completely closed. The pressing force is set to 0.2, 0.4, and 0.6 kN.

5. The pressing force is maintained while nitrogen gas is introduced into the chamber again for cooling at a rate of approximately 0.3 °C /s, until the mold temperature is 80 °C. The pressing force is maintained during cooling to prevent shear deformation at the substrate interface, which would adversely affect the adhesion strength, while compensating for the shrinkage of HDPE.

Finally, the mold is opened and the molded Si-HDPE hybrid micro-lens is removed and naturally cooled to room temperature. The time taken for a complete cycle of the press molding process was approximately 370 s.

4.1.3.2. Demolding with uncoated mold

During the experiment, the HDPE polymer adhered to the mold surface and was difficultly removed from the mold. This is due to there being no coating applied on the mold surface. Demolding is very important when removing a lens from the mold. Excessive demolding force, caused by the sticking force between the mold and the polymer, can cause damage to the microstructures [62].

According to Omar et al., the demolding force occurs due to the friction, deformation, and the adhesion phenomenon [63]. However, in this research, as there is no draft angle on the lens array, the deformation and the friction force is neglected. The demolding force (F_d) calculation is as follows:

$$F_d = F_{ad} + F_{fr} \tag{4.1}$$

where F_{ad} is the adhesion force and F_{fr} is the friction force. In calculating the adhesion force, an equation developed by Kendall can be used to calculate the adhesion strength (σ_{ad}) at first [64]. The equation is as follows:

$$\sigma_{ad} = \left[\frac{2K}{t_p}\left(\gamma - \frac{t_p.K\varepsilon^2}{2}\right)\right]^{1/2} \quad (4.2)$$

where K is the bulk modulus, and ε is the coefficient of the thermal expansion of the polymer, both of which are multiplied with the temperature changes, ΔT whereas t_p is the polymer thickness. To complete the adhesion force calculation, the following equation can be used, whereby A is the surface area contact between the polymer and the mold:

$$F_{ad} = \sigma_{ad} \times A \quad (4.3)$$

In order to reduce the adhesion forces between the mold and the polymer, the mold release agent was applied to the mold surface before the press molding process itself and a silicone mold release agent was used. After the press molding process, the formed lens is easily detached from the mold as compared to the without the use of mold release agent. However, the silicone coating was found to be contaminating the mold surfaces as well as the formed lens, resulting in a dirty formed lens, as presented in Figure 4.6. The adhesion between the HDPE and Si was also not achieved. Therefore, the mold release agent coating is not suitable.

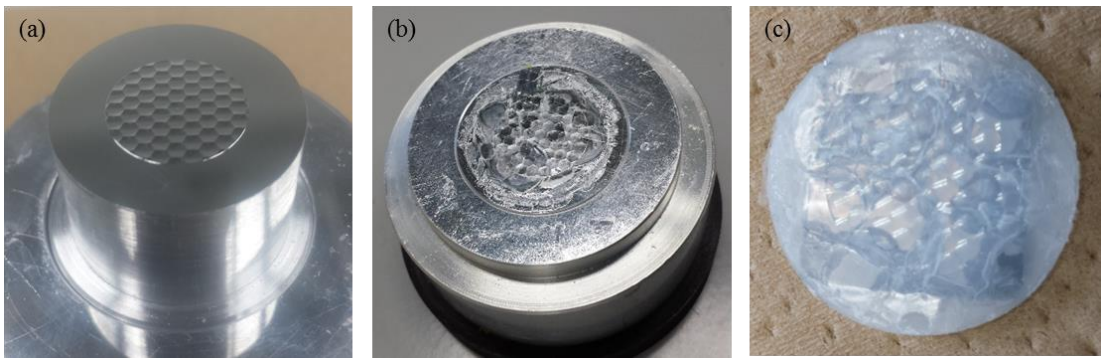

Figure 4.6: Photograph of: (a) lens array mold, (b) contaminated lens insert, and (c) contaminated formed lens.

The upper mold was further improved and modified as to compensate for the unsuitability of a mold release agent. The upper mold insert was modified and the stripper ring was added to it. The stripper ring is placed around the mold insert, as displayed in Figure 4.7.

The stripper ring ejects the fabricated lens after molding in the absence of the mold release agent.

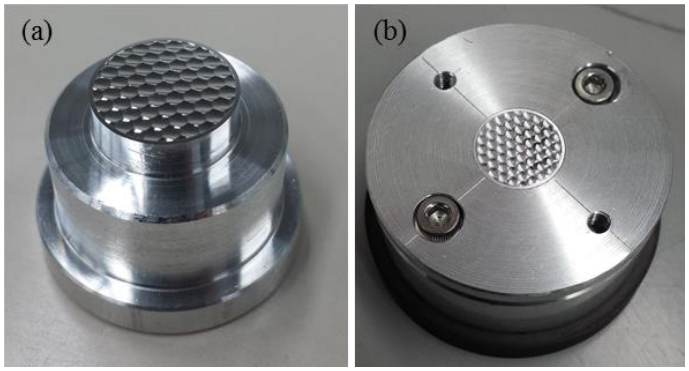

Figure 4.7: Photograph of (a) mold insert without coating, and (b) upper mold assembly with stripper ring.

A press molding experiment using the upper mold with the stripper ring was conducted. After the press molding process, the stripper ring was lifted up manually and was able to eject the lens from the mold. However, it was also found that the adhesion between the fabricated hybrid lens and the mold insert still persisted. The micro lenses were torn off from the lens, due to the adhesion phenomenon between the mold and the lens, as per shown in Figure 4.8(b). Due to the adhesion force after the molding process, the mold insert requires an anti-sticking mold coating.

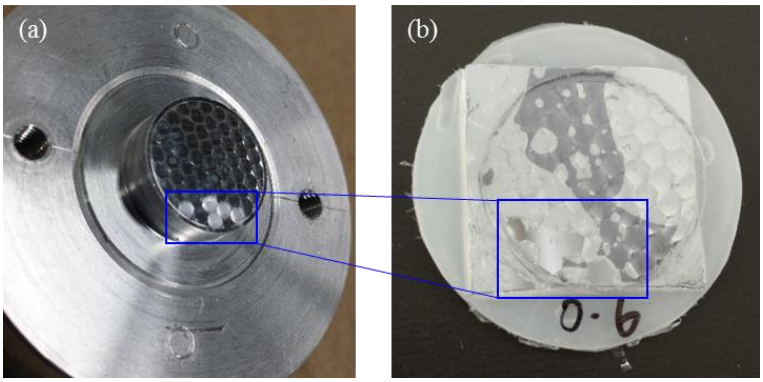

Figure 4.8: Photograph of (a) adhesion of HDPE on the mold insert, and (b) tear off lens.

4.1.3.3. Mold coating

To lower the adhesion force between the mold and the formed hybrid lens, the mold is coated with an anti-sticking layer. Several coating materials were considered, such as the diamond-like coating (DLC), nickel (Ni), and also polytetrafluoroethylene (PTFE). These coatings have been found by previous researchers to help demold the formed specimen [65]. The PTFE coating was selected to lower the surface adhesion energy during the demolding process, as the coating provides lubrication on the mold surfaces to ease the parts removal process [66].

To improve the coating strength, a Ni coating layer was first applied on the mold, followed by a SiO_2 layer [67]. The PTFE layer was then applied on the SiO_2 layer, whereby the bonding of both layers reacted with oxygen (O) and hydroxide (OH). The coating layer is illustrated in Figure 4.9. The thicknesses of the coatings were 20 nm, 10 nm, and one molecular layer, respectively, for the three coating materials. The coating process was performed by physical vapor deposition (PVD) in Geomatec Co. Ltd., Japan. The finished coats of the mold are presented in Figure 4.10.

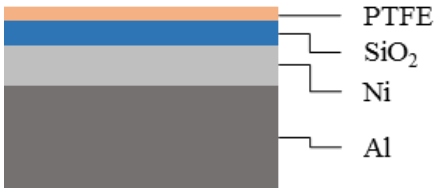

Figure 4.9: Layer structures of the mold insert coating.

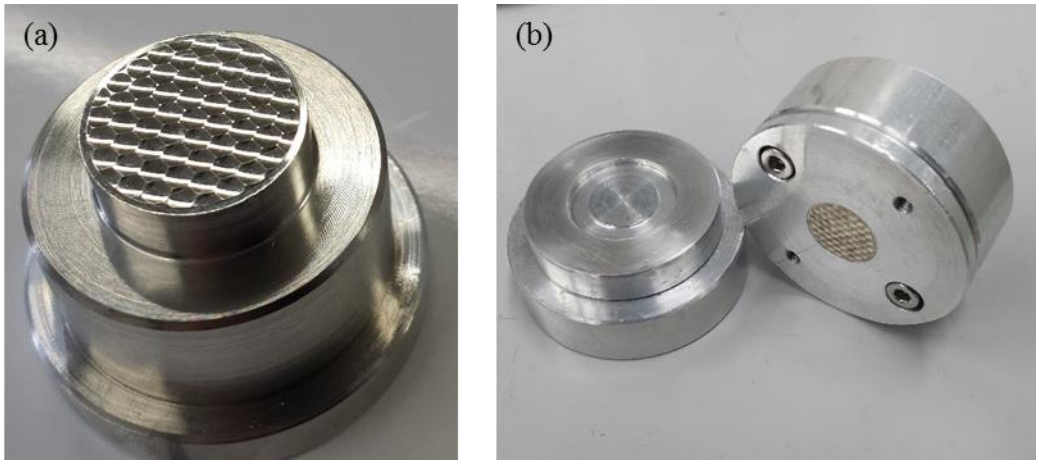

Figure 4.10: Photograph of (a) coated mold insert, and (b) mold assembly.

4.1.4 Form accuracy and surface integrity of micro lens array

The fabricated micro-lens array by press molding was measured after the molding process. This is carried out to evaluate the form accuracy and the surface integrity of the lens. The outcomes resulting from the measurement were compared to ascertain the best press molding parameters for the micro-lens array.

4.1.4.1. Form accuracy

The lens topography measurements were performed after the molding process using a non-contact measuring machine, NH-3SP (Mitaka Kohki Co, Japan), in order to avoid contact damage to the lens surfaces. The machine was equipped with a laser probe (semiconductor laser, wavelength 635 nm) which can scan the lens surfaces three-dimensionally. The vertical resolution of the machine is 1 nm, while the laser beam diameter is approximately 1 μm, to ensure the narrow edges of the lens surface can be precisely measured. During the lens surface measurement, a horizontal resolution of 10 μm was selected. The topography obtained was then analyzed using the Talymap software (Taylor Hobson Ltd.), during which the micro lens cross-section was obtained.

In this study, for the sake of simplicity, the form error of the molded lens was evaluated by measuring the lens sag height. The sag height of the lens molded at pressing temperatures of 133 and 140 °C and pressing forces of 0.2, 0.4, and 0.6 kN respectively are shown in Figure 4.11. Minimum force needs to be used to prevent the Si wafer from being broken.

In the experiments, the first upper mold design without a plunger was used. It was observed that the lens sag height depends on the pressing temperature. Figure 4.11(a) demonstrates that the average sag height is about 43 µm at the pressing temperature of 133 °C. At a temperature of 140 °C, the sag height of the lens decreases to 42 µm, as shown in Figure 4.11(b). The sag height difference was caused by polymer shrinkage during the cooling stage. The higher the molding temperature is, the larger the shrinkage rate is during the cooling stage [47].

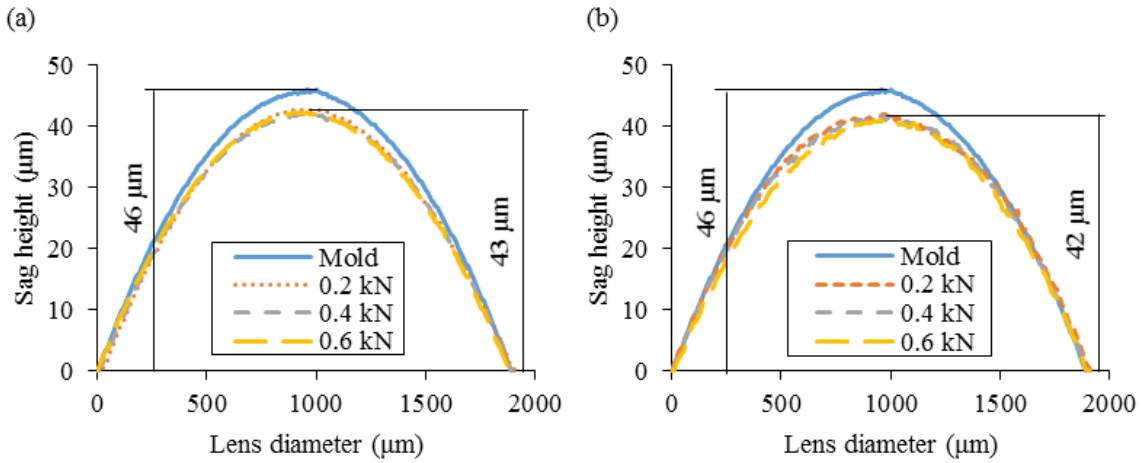

Figure 4.11: Sag heights of lenses formed at different molding forces and different temperatures: (a) 133 °C, and (b) 140 °C, using the upper mold without a plunger.

In Figure 4.11, it was discovered that at both temperatures, the pressing force had no significant effect on the lens sag height. This is because when the molds are closed, the upper mold and the ring on the lower mold come into contact, thus preventing them from further movement during cooling, to compensate for the HDPE shrinkage. Hence, the mold without a

plunger is unsuitable for improving the lens form accuracy. The second design of the mold, which contains a plunger, was then used for comparison.

Figure 4.12(a) displays the lens sag heights formed at a temperature of 133 °C under different pressing forces. The sag height was measured at 44 µm with the pressing force of 0.2 kN. The increase of the pressing force to 0.4 and 0.6 kN further reduced the sag height to 43 and 41 µm, respectively. The reasons for sag height errors in Figure 4.12(a) involve two aspects: air trapping at the apex of the lens during molding, and polymer shrinkage during cooling. The latter is not affected by pressing force, but the former is strongly affected by the pressing force.

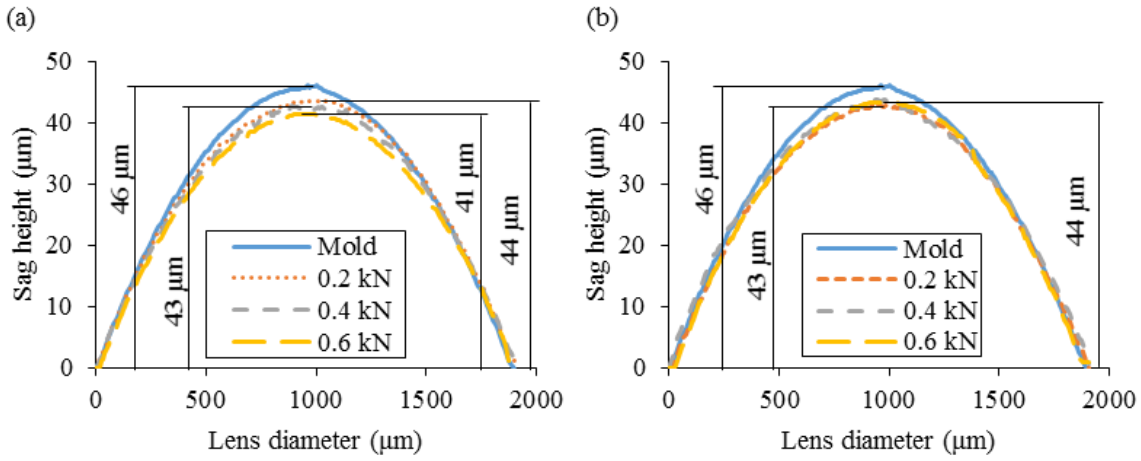

Figure 4.12: Sag heights of lenses formed at different molding forces and different temperatures: (a) 133 °C, and (b) 140 °C, using the upper mold with a plunger.

At low temperatures, which causes high polymer viscosity, a higher pressing force causes a thicker air trap, as displayed in Section 4.1.4.4. As a result, an increase of the pressing force reduces the sag height. It is due to trapped air exerting a uniform cavity pressure on the cavity boundary, as demonstrated in the schematic diagram in Figure 4.13(b). This is also due to the fact that the molding process is done in a non-vacuum environment. Figure 4.14, demonstrates the air trapping phenomenon on the lens apex surface.

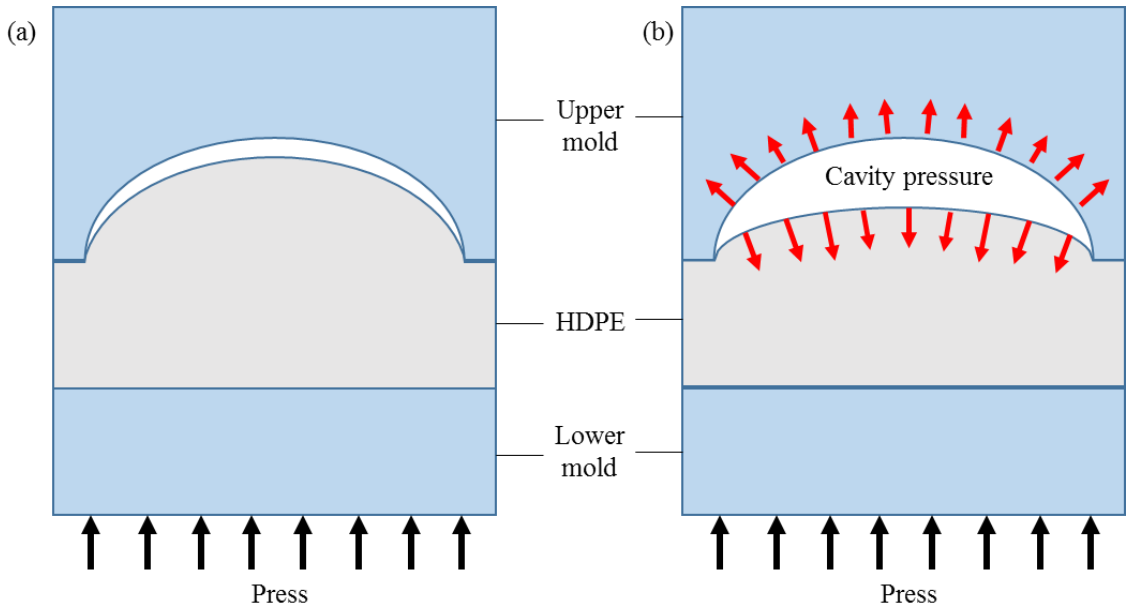

Figure 4.13: Schematic diagram of: (a) press molding in a vacuum, and (b) press molding in a non-vacuum environment.

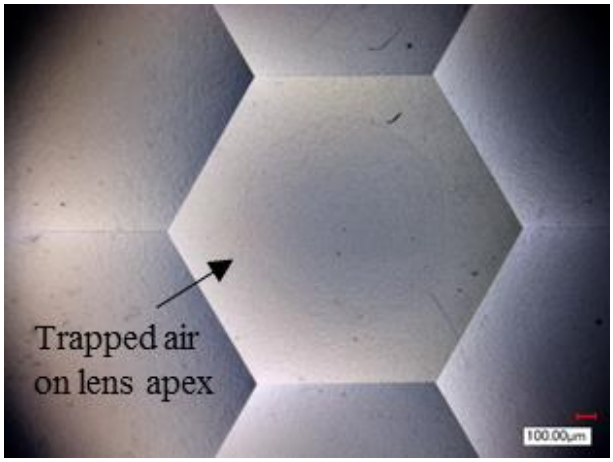

Figure 4.14: Air trapping on lens apex.

As shown in Figure 4.12(b), the sag height was measured at 43 µm when forming at a temperature of 140 °C with the pressing force of 0.2 kN. As the pressing force increased to 0.4 and 0.6 kN, the sag height accuracy slightly increased to 44 µm. At this temperature, the polymer viscosity is reduced, and the different pressing forces significantly affect the sag height. An increase in the temperature helps to decrease the viscosity of the polymer, thus improving the filling of the cavities [68]. The second design of the mold with a plunger is

suitable because it increases the cavity pressure during the pressing process. The plunger also provides additional movement during the cooling stage to compensate for polymer shrinkage.

Meanwhile, as the press molding was done under the molten state of the polymer, it found that the changes of the temperatures were not giving any improvement on the form accuracies. The maximum achievable sag height is 44 μm. This is due to the polymer is subjected to the shrinkage factor after the cooling process.

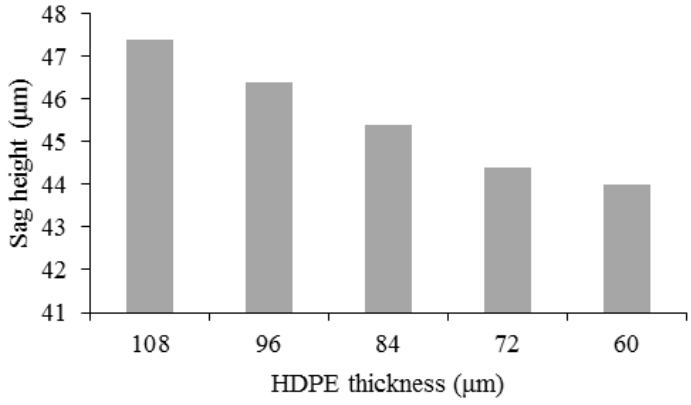

Figure 4.15: Lens sag heights for different HDPE thicknesses.

Furthermore, the sag height of the lens decreased with the reduction of the HDPE thickness on the Si substrate, as shown in Figure 4.15. The phenomenon might be due to the retarding flow of HDPE as the cavities become narrower [69].

4.1.4.2. Viscosity measurement

A viscosity measurement was conducted to evaluate the viscosity of the HDPE at the different temperatures. The measurements was done at Shimadzu Co., Japan, and the equipment used was flow-tester capillary rheometers (CFT 500-EX). The measurement parameters are provided in Table 4.2. During the testing, two different temperatures were used, 133 and 140 °C, whereby both temperatures were maintained during the testing.

Table 4.2: Viscosity measurement parameters.

Parameters	Value
Extrusion pressure, MPa (kgf/cm^2)	4.903 (50)
Die shape:	
Die diameter, mm	1
Die length, mm	1
Temperature, °C	133, 140
Preheating time, min	10
Piston stroke, mm	3~7

To calculate the viscosity of the polymer at a different temperature, the following equation can be applied:

$$\eta = \frac{\pi D^4 P}{128 L Q} \times 10^{-3} (Pa.s) \tag{4.4}$$

where D is the die diameter, P is the test pressure, L is the die length, and Q is flow rate. The schematic diagram of the viscosity measurement unit is showed in Figure 4.16. To calculate the flow rate, the following equation can be used:

$$Q = A \times \frac{S_2 - S_1}{10 \, \Delta \, t} (cm^3/s) \tag{4.5}$$

where A is the piston cross section area, S_2 is calculation start point, S_1 is calculation end point, and Δt is piston travel time from S_2 to S_1.

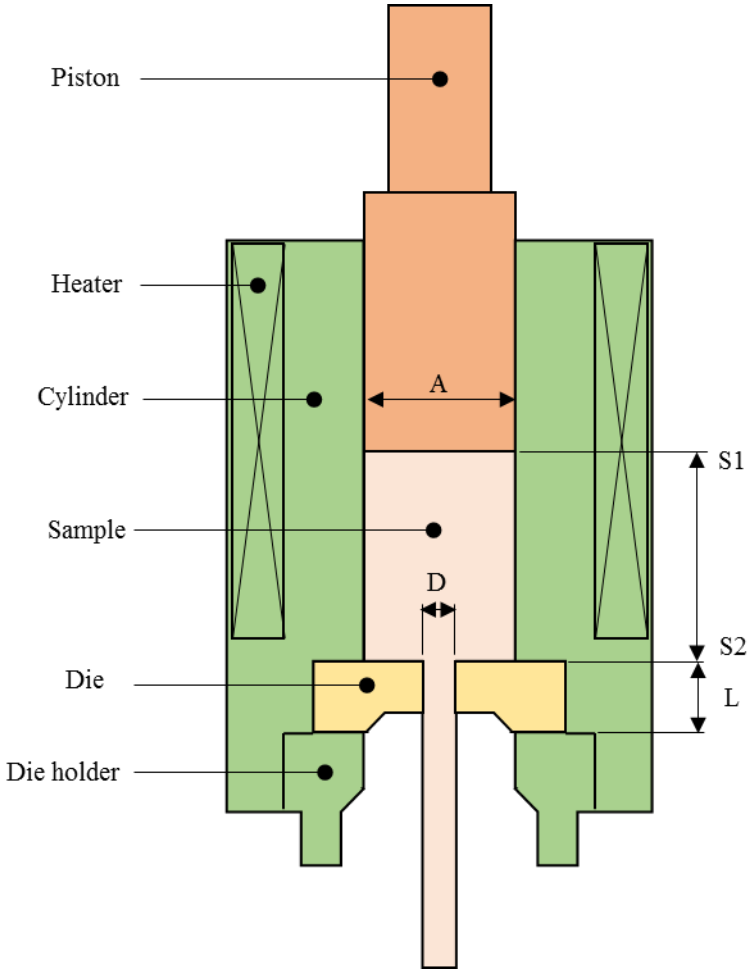

Figure 4.16: Schematic diagram of a viscosity measurement unit.

From the viscosity measurement, it is observed that the viscosity of the HDPE at 133 °C was 4.699×10^3 (Pas), whereas it decreases to 3.689×10^3 (Pas) when the temperature is increased to 140 °C. As such, the viscosity decreases at the higher temperatures, and this will help improve the form accuracy of the micro lens.

4.1.4.3. HDPE plate as raw material

An experiment involving the use of a HDPE plate, instead of HDPE granules as a raw material, was done. This was done to test the effect of the HDPE raw shape to its form accuracy. In the experiments, a HDPE circular plate with the diameter of 15 mm and the thickness of 3

mm was used. However, as no silane-cross linkable HDPE were available in the market, the HDPE plate was molded from the HDPE granules, in Figure 4.17.

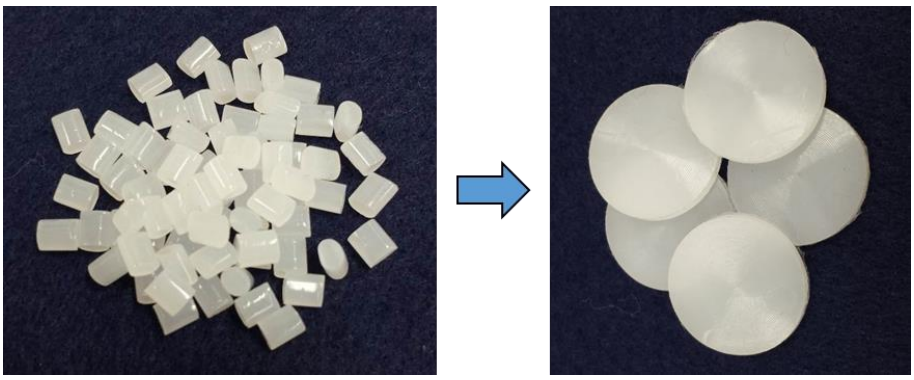

Figure 4.17: HDPE pellets to circular plate.

To form the HDPE plate, an aluminium mold was fabricated with the circular shape cavity, as displayed in Figure 4.18. The lower mold consists of a mold cavity, 15 mm in diameter, which is fabricated on the circular stripper ring to permit easy part removal after the press molding process. Meanwhile, the upper mold contains a plunger and is designed with the same diameter of the lower mold cavity.

The press molding process was used to form the HDPE circular plate, which is where the HDPE pellets are inserted into the mold cavity. The process was continued by heating the mold and polymer to the melting temperature of HDPE (133 °C), followed by pressing. Finally, after the cooling stage, the plate was removed from the mold.

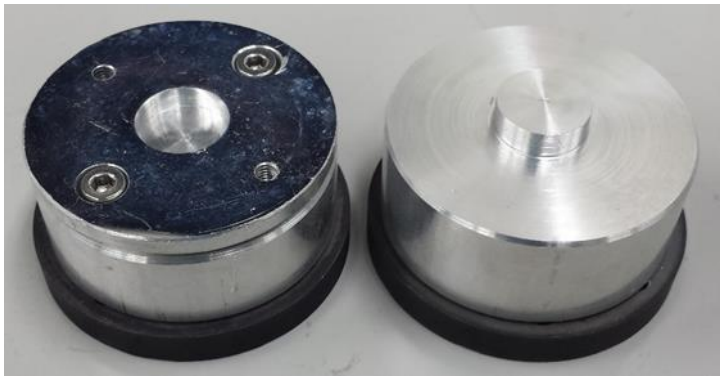

Figure 4.18: HDPE circular plate mold assembly.

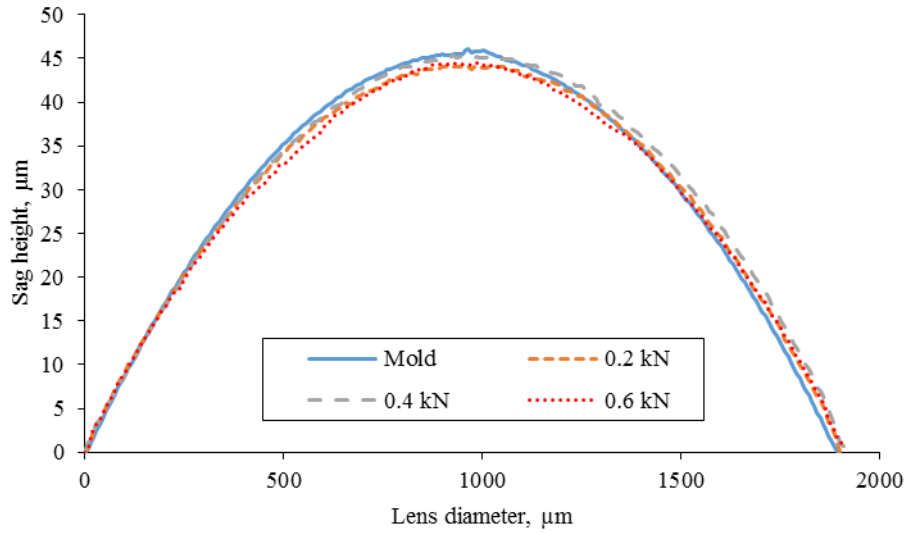

Figure 4.19: Sag heights of lenses formed at different molding forces using a HDPE circular plate.

Press molding experiments were carried out using the HDPE plate as the raw material. The polymer plate was inserted into the mold, heated to 140 °C and pressed. After cooling, the plate was removed from the mold to be measured. The measurements demonstrate that the sag height of the lens improved, compared to the used of the HDPE pellets, as discussed earlier in the previous section. The sag height was measured at 44-45 µm with different pressing forces. As per the results in Figure 4.19, it is clear that the HDPE plate would improve the sag height form accuracies. This is because the void for air trapping to occur is reduced. However, melting the HDPE plate again, during the press molding of lens arrays will cause deteriorations of the polymer properties [70].

4.1.4.4. Surface integrity

In press molding and hot embossing of microstructures, air trapping is a critical issue which greatly affects the surface integrity of the final component. The trapped air prevents the polymer from completely filling up the cavities of the mold [71]. The trapped air been reported to form a pattern on the formed surface [72]. In press molding of Si-HDPE hybrid lenses in a non-vacuum environment, it is also observed that the presence of air trapping induces surface

defects on the pressed lenses, which in turn creates the interface gap between the Si-HDPE substrates. However, the formation mechanism of air trapping is not clear yet. The present study used HDPE pellets instead of a polymer plate, the latter of which had been used in hot embossing, but the impact of the use of polymer pellets as raw materials on air trapping has not yet been investigated extensively.

To solve the problem of air trapping, usually evacuation tools are required for the air to escape, and these tools are often used in micro-injection molding [73,74]. Micro-aspiration mold cavities are also useful for air trap ventilation [75]. However, it is not clear whether there are other methods to eliminate air trapping, such as by vacuum molding and/or by controlling other molding conditions.

When the molding test was done in a non-vacuum environment, trenches occasionally formed on the lens surface, as displayed in Figure 4.20(a), leading to severe surface unevenness as shown in Figure 4.20(b). The images of the lens surfaces which are formed at different molding temperatures and pressing forces are illustrated in Figure 4.21. As a general trend, air trapping and trenching occurs in the centre region at a low pressing force, and in the outer area of the lens array at high forces, as presented in Figure 4.21(a)–(c). An increase of pressing force causes the movement of trapped air from the centre of the lens array to the outside area of the lens during pressing. The results in Figure 4.21 also indicate that the use of a small pressing force (0.2 kN) is better than a high pressing force (0.6 kN) to reduce the area of trapped air. In addition, as shown in Figure 4.21(d)–(f), air trapping and trench formation are reduced when the lens is formed at a higher temperature (140 °C). An increase in the temperature lowers the influence of molecular weight, and in turn, the reduces the viscosity of the polymer, thus suppressing the formation of trenches [69,76].

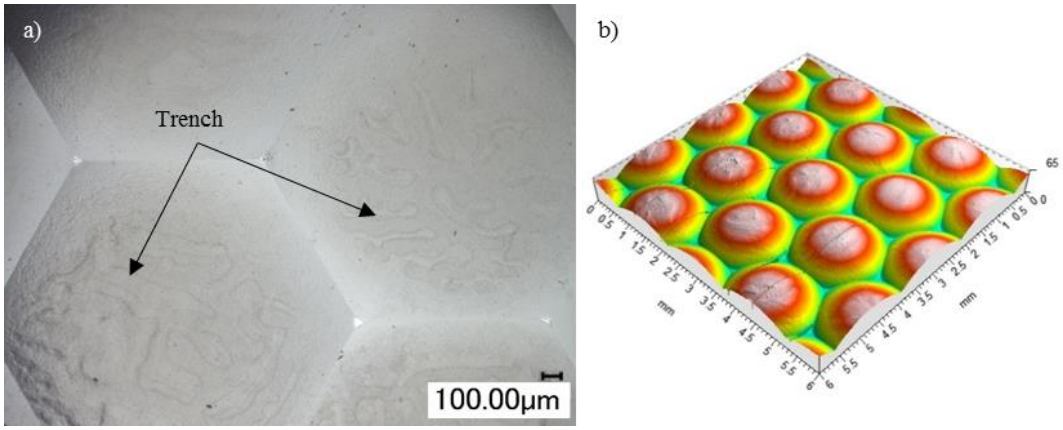

Figure 4.20: (a) Photograph of trench formation on a lens surface and (b) three-dimensional topography of a Si–HDPE hybrid lens, showing an uneven lens surface.

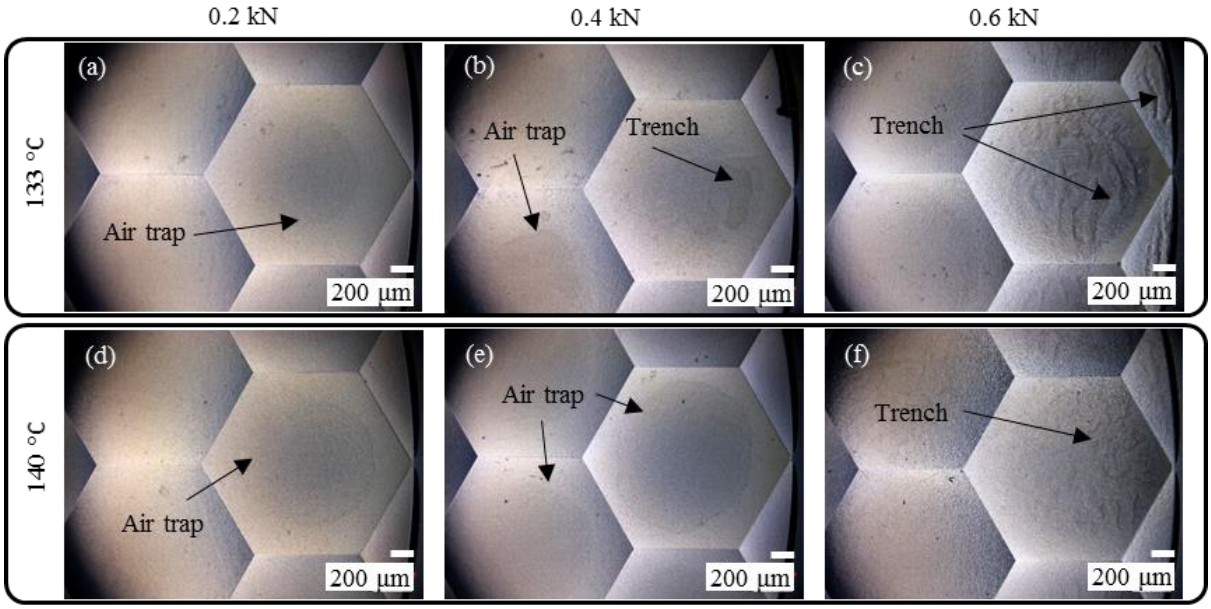

Figure 4.21: Air trap and trench formation under different pressing forces and temperatures.

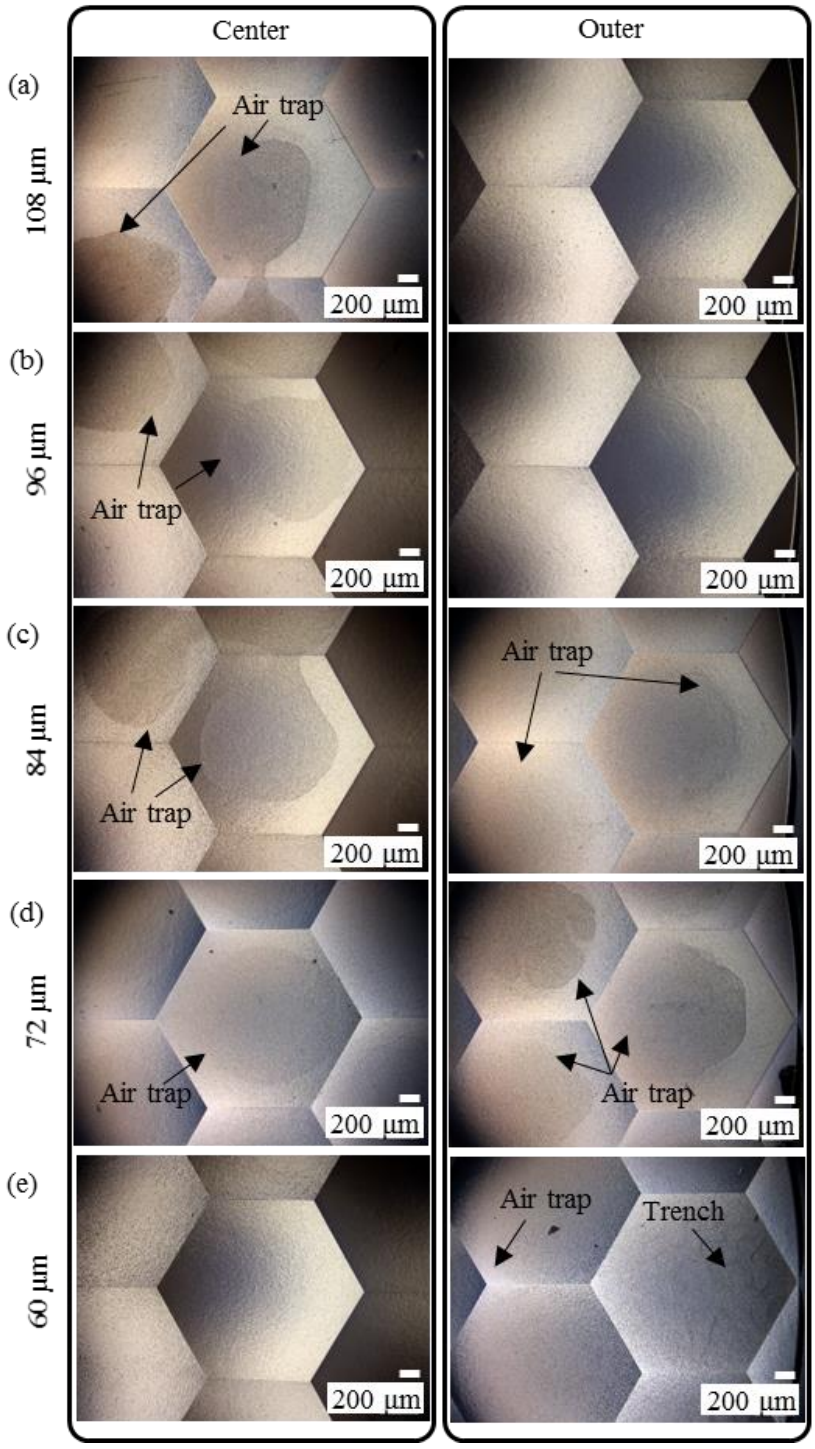

Figure 4.22: Air trapping phenomena at different HDPE thicknesses.

The air trapping phenomenon was further investigated by pressing HDPE into different thicknesses. The images of the centre and outer areas of the lens array obtained at various HDPE thicknesses are illustrated in Figure 4.22. As shown in Figure 4.22(a) and (b), an air trap occurs at the centre of the lens array when HDPE had pressed thicknesses of 108 and 96 µm

respectively. When the HDPE is pressed further, the trapped air moves from the centre to the outer lens arrays, as shown in Figure 4.22(c) and (d). As the HDPE is pressed to 60 μm thick, the trapped air moves entirely to the outer area of the lens array and tends to escape from the lens array area. The remaining air at the outer area receives the molding pressure, and trenches are created on the top of the lens surface, as shown in Figure 4.22(e).

4.1.5 In-situ observation

A finite element analysis (FEA) can be to predict the flow of the polymer during press molding or hot embossing [77]. Many types of FEA simulation software are reported to analyse the polymer flow. They include MoldFlow, Abaqus, Deform2D, as well as Ansys. The software will predict the result of the polymer flow based on numerical calculation.

Finite element simulation is used extensively to predict the behaviour of the air trap during the molding process [39,78]. However, presently, there are few experimental studies on real-time direct observation of the air trapping phenomenon during press molding [68,79]. As of yet, the effects of trapped air on the performance of mold coating have not yet been clarified. In this study, an in-situ real-time observation system was constructed for clarifying the air trapping phenomenon during the press molding of the Si-HDPE hybrid lenses.

An in-situ observation allows real-live direct monitoring to be carried out. The real-live event can be captured with a camera wherein the actual trapping phenomenon can be captured. As the HDPE material used in the experiment is in the form of pellets, it is very important to observe how the pellets mix among each other

4.1.5.1. Experimental setup

To investigate the air trapping phenomenon during the pressing process, a mold with a cross-sectional slice were designed and fabricated, to observe the HDPE pellets flow during

pressing. As shown in Figure 4.23, the mold was cut in half and included a slot feature. A glass plate was then attached into the slot, and a digital camera was used to record the flow of the polymer during the pressing process through the glass plate. To begin the in-situ observation, both the mold and the specimen were heated inside the quartz chamber to the required temperature. Once the temperature was reached, the chamber was opened immediately, enabling the pressing step to be captured.

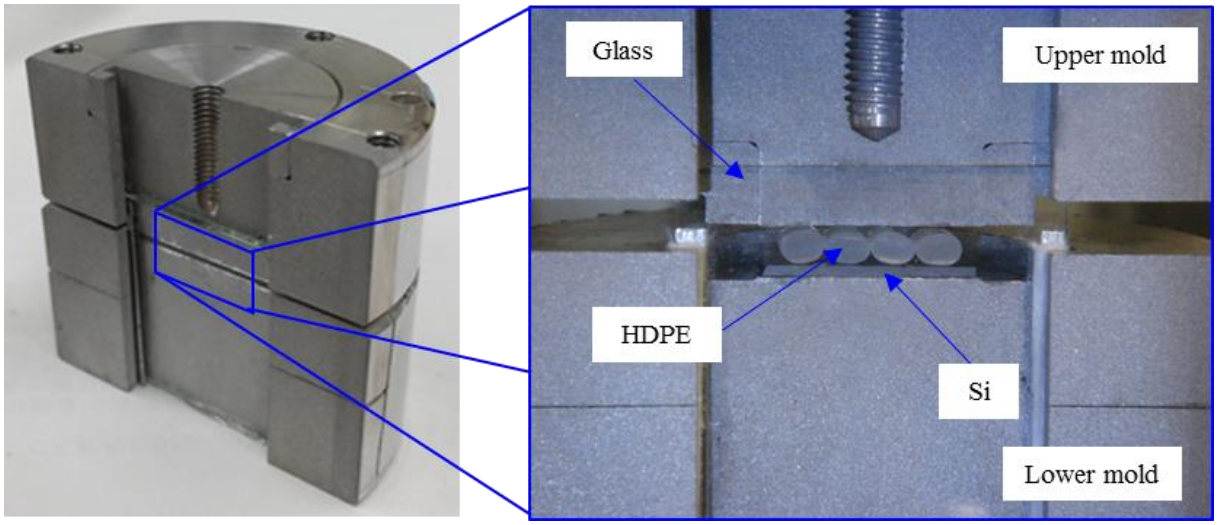

Figure 4.23: Photograph of a cross-section of sliced molds.

4.1.5.2. In-situ observation

To investigate the air trapping phenomenon during the press molding, an in-situ observation was performed using the newly developed observation unit. The images of the in-situ observation at a temperature of 133°C are illustrated in Figure 4.24. Figure 4.24(a) displays air pockets being formed at the boundaries between HDPE pellets and the upper mold as well as between the Si substrate and the HDPE pellets. Furthermore, weld lines are formed at the boundaries between the HDPE pellets. During pressing, the air pockets become smaller and are flattened, as shown in Figure 4.24(b)–(e). As a result, trapped air channels are formed on the lens surface. However, when the pressing continues, the trapped air escapes and vanishes

as shown in Figure 4.24 (f). Due to excessive pressing, an overflow of the HDPE is seen inside the gap between the glass plate and the mold.

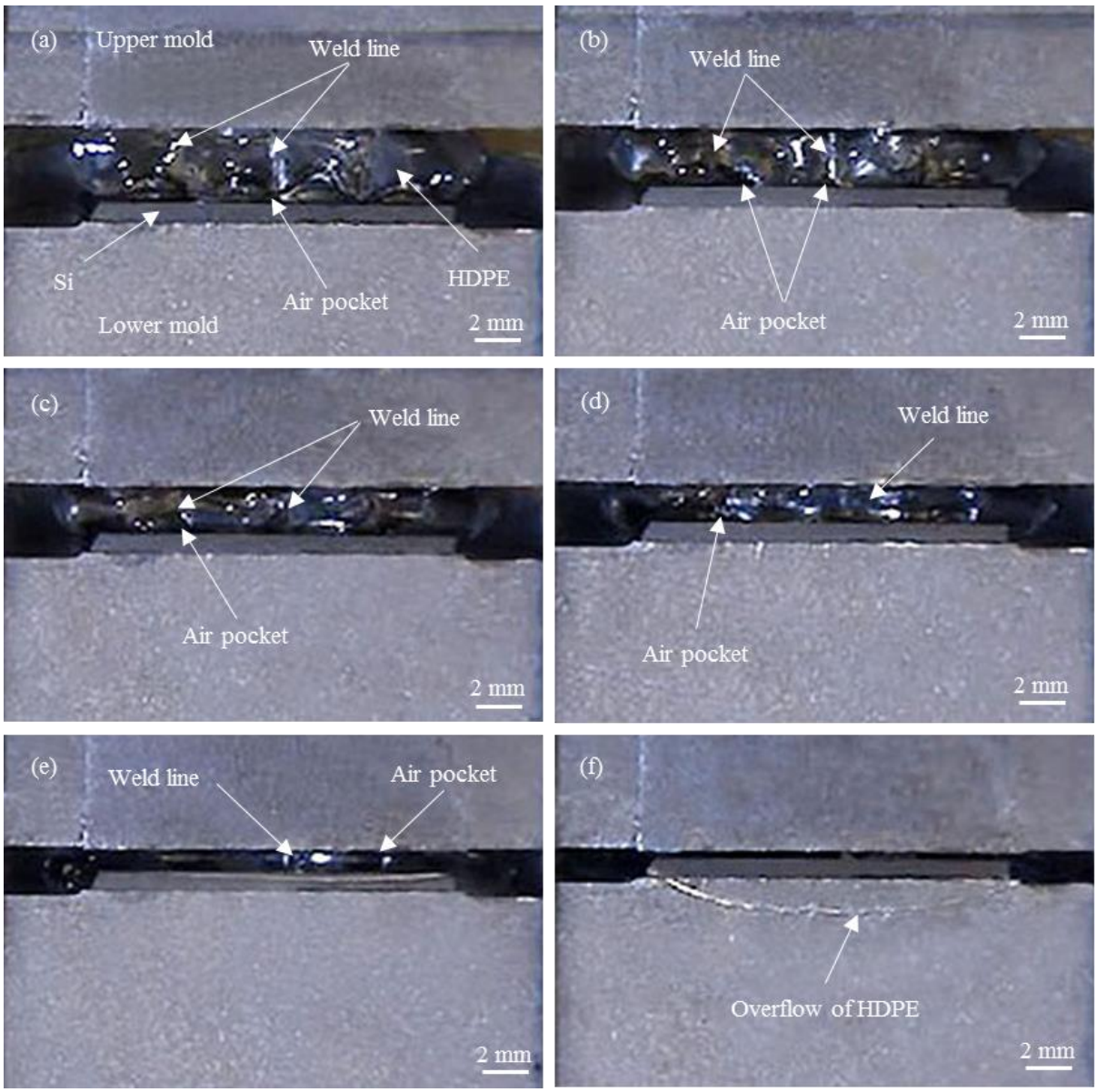

Figure 4.24: In-situ air trapping observation results at 133 °C.

The images of the in-situ observation at a temperature of 140 °C are illustrated in Figure 4.25. Weld lines are seen among the pellets but they are less obvious than those in Figure 4.24. This is due to the decrease of HDPE viscosity with the temperature rise. However, air pockets still exist among the pellets, as shown in Figure 4.25(a). When the HDPE pellets are further pressed, the weld lines started to vanish, and the air pockets size was reduced, as shown in

Figure 4.25(b) and (c). Air pockets cannot be clearly seen in Figure 4.25(d). Then, with further pressing, the air pockets vanished completely along an overflow of HDPE, as shown in Figure 4.25(e) and (f).

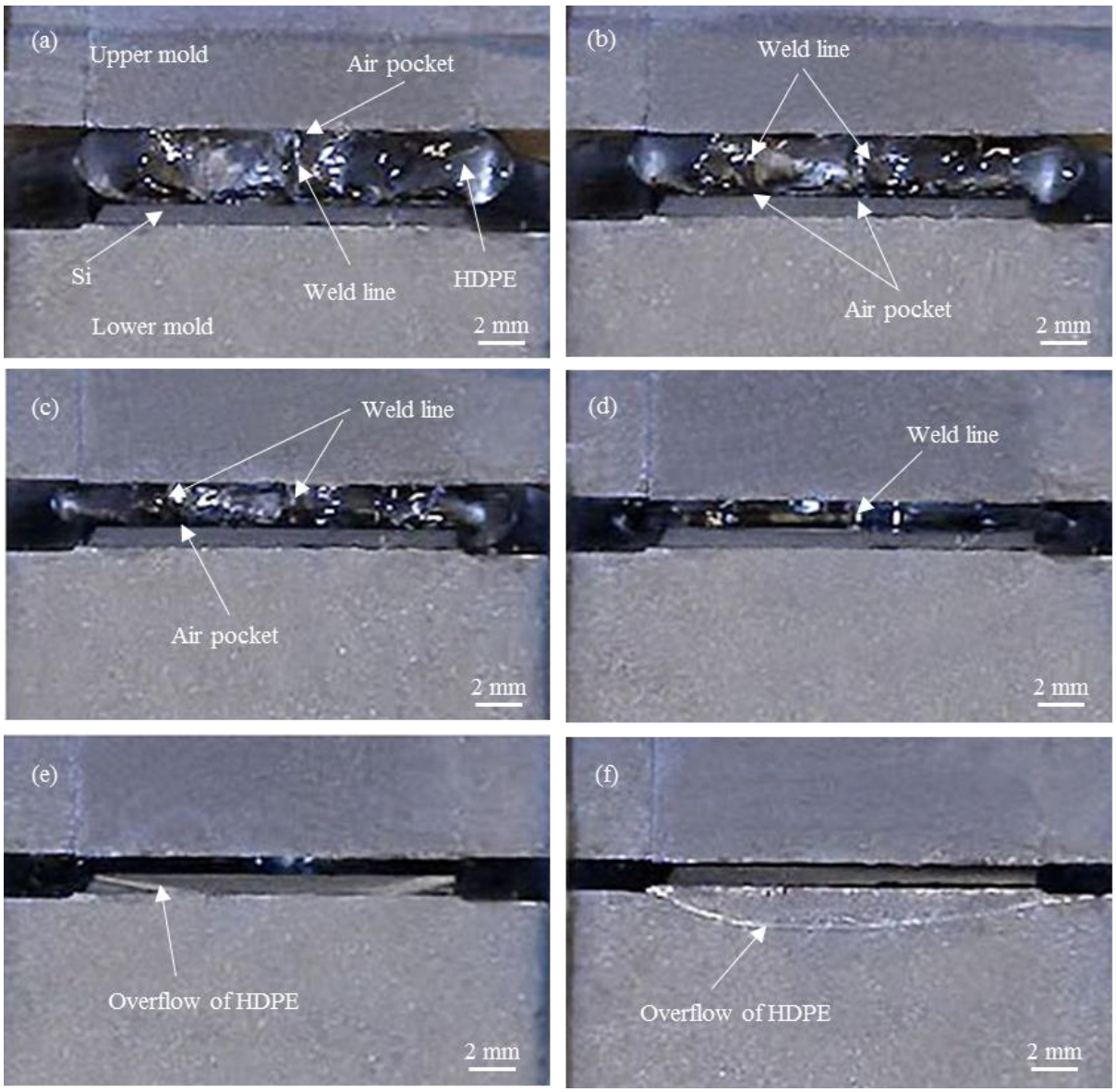

Figure 4.25: In-situ air trapping observation results at 140 °C.

Based on the above observations, Figure 4.26 displays the schematic diagram of the air pocket formation. It is demonstrated that the HDPE pellets contribute to the air trapping phenomenon. This differs from plastic injection molding, wherein pellets are heated and mixed inside a barrel before being injected into the mold. In the present study the pellets need to be

mixed during pressing. Weld lines and air pockets occur among the pellets which lead to air trapping.

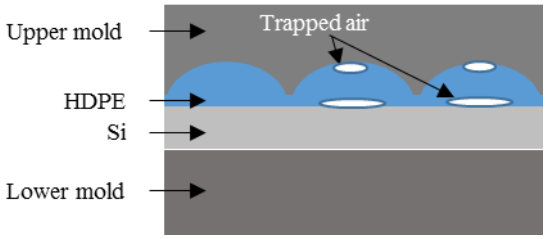

Figure 4.26: Schematic diagram of air trapping formation.

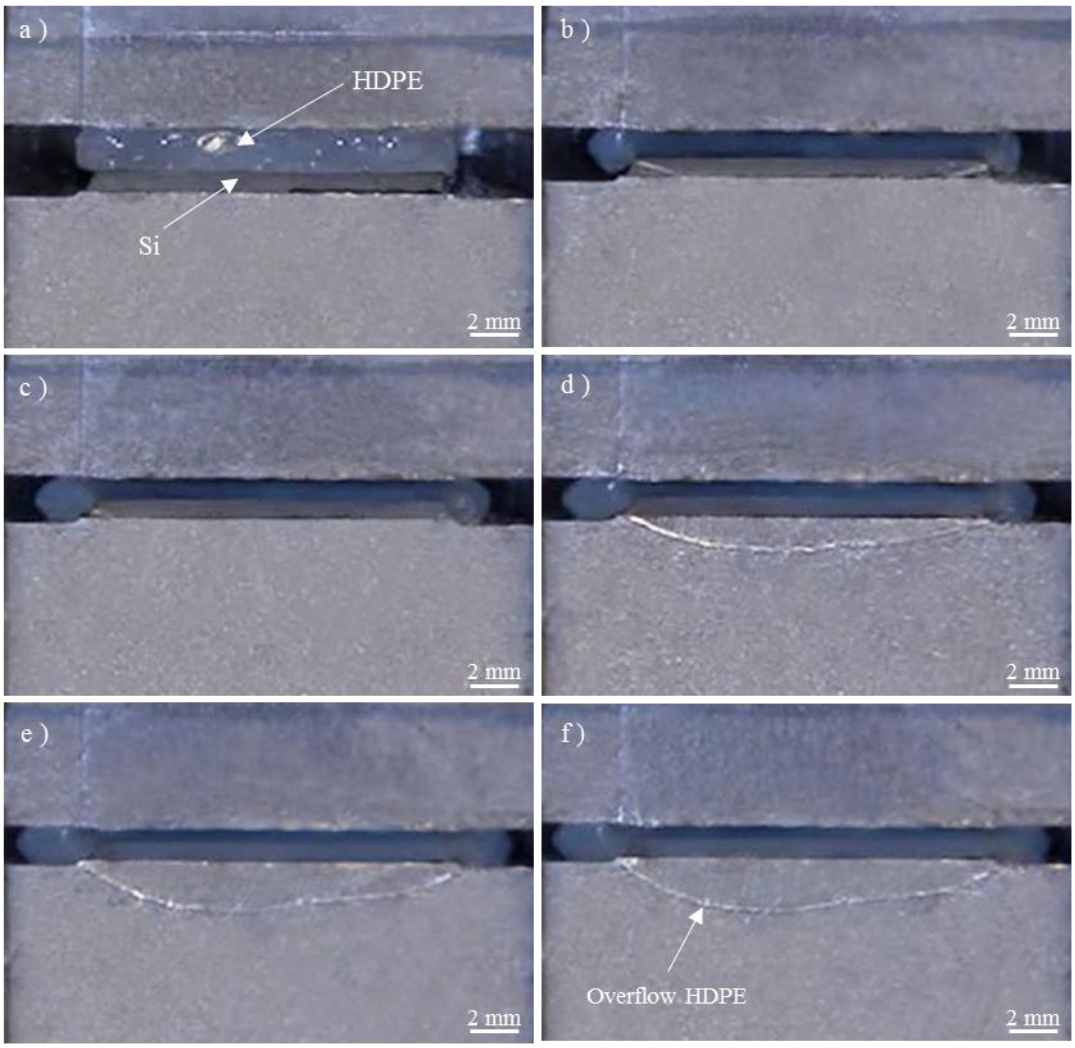

Figure 4.27: In-situ air trapping observation for a flat shaped HDPE.

The in-situ observation also indicates that the temperature plays important role during the pressing as the pellets need to be mixed with each other during the press molding process.

The lower the viscosity of the polymer, the greater the reduction of the weld lines, thus the pellets are more easily be mixed.

To further clarify the effect of specimen shape on air trapping, instead of HDPE pellets, a flat HDPE plate with a diameter of 15 mm and a thickness of 1.5 mm was used for press molding at a temperature of 140 °C. The in-situ observation results using the HDPE plate as the raw material is displayed in Figure 4.27. In this case, no weld line nor air pockets were found. Thus, in preventing air trapping, a plate shaped specimen is better than pellets.

4.1.6 Numerical simulation of pellets press molding

A numerical simulation was done to investigate the flow of the polymer during the press molding. In this simulation, the flow was observed. However, a polymer data from Jha et al. was referred [80], due to insufficient HDPE stress-strain data being available. The press molding condition was considered a vacuum condition. Meanwhile, two HDPE resin in the simulation is at first slightly attached each other's as a one body to permit the simulation to be run. A two-dimensional analysis was conducted within an asymmetrical condition. Figure 4.28 illustrates the schematic diagram of the simulation setup. In detail, a slip condition of 0.2 was used for both upper and lower boundary, and a two dimensional (2D) setting was also used.

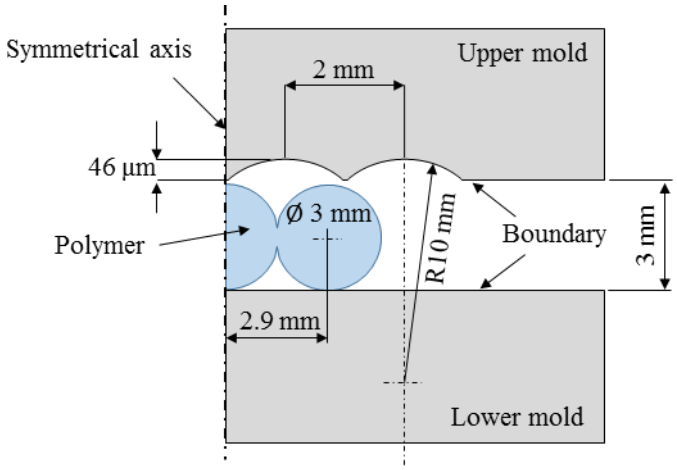

Figure 4.28: Schematic diagram of the pellets press molding simulation setup.

To perform the simulation, a DEFORM (Scientific Forming Technologies) software was selected. It was a commercial software used to analyse the metal forming process, especially when it involved large deformation. A polymer data was inserted into the software to enable the flow analysis of the polymer. During the simulation, only press molding was simulated in which the polymer were assumed to have uniform density and temperature distribution.

The upper and lower mold were set as a rigid body, while the polymer was set as plastic. In defining the flow stress of the polymer, a tabular data was used [80]. The polymer data was obtained from the reference, which is tabulated in Table 4.3.

Table 4.3: Stress-strain tabular data (Stress: MPa).

T (°C)	95		100		140		250	
$\epsilon \rightarrow$	0.000	1	0.0001	1	0.0001	1	0.0001	1
$\dot{\bar{\epsilon}} \downarrow$ (s^{-1})	1							
0.05	28	31	5.5	5.5	0.06	1.16	0.006	0.006
0.5	21	24	5.5	5.5	0.06	1.16	0.006	0.006
1	55	58	5.5	5.5	0.06	1.16	0.006	0.006

Meanwhile, the creep of polymer was neglected because it was considered as viscous flow of non-Newtonian flow fluid. The governing equation for the tabular data of the polymer was stated as follows:

$$\bar{\sigma} = \bar{\sigma}\left(\bar{\epsilon}.\dot{\bar{\epsilon}}.T\right) \tag{4.6}$$

where $\bar{\sigma}$ represents the flow stress of the polymer, $\bar{\epsilon}$ represents the effective plastic strain, $\dot{\bar{\epsilon}}$ represents the effective strain rate, and T represents the temperature. For the conservation of the mass, a continuity equation was used as follows:

$$\frac{\partial \rho}{\partial t} + \nabla.(\rho v) = 0 \tag{4.7}$$

where ρ denotes the polymer density and v denotes the velocity. To describe the relationship between the momentum transfer and conservation, a Navier-Stokes momentum was applied in the simulation. The below equation describes the momentum.

$$\frac{\partial v_i}{\partial t} + \mathrm{v}_j \frac{\partial v_i}{\partial x_j} = \frac{1}{\rho}\frac{\partial \sigma_{ij}}{\partial x_j} + f_i \tag{4.8}$$

where the force per unit mass is defined by f_i. As the in-situ observation used two different temperatures, the same pressing temperature of 133 and 140 °C was applied in the simulation.

From the simulation, the resin was found to receive stress when it was pressed with a temperature of 133 °C. The simulation process can be observed in the images in Figure 4.29. Due to higher viscosity of the polymer, a high level of stress was also recorded in this temperature. Similar to the in-situ direct observation discussed in the previous section (Section 4.1.5.2), a weld line existed between the pellets as shown in Figure 4.29 (c) and (d). The weld lines are defined when the two resins meet during pressing. When the mold closing distance reduced, the resin started to mix each other, and subsequently caused some stress at the weld line boundary. The simulation result demonstrated that when the pressing distance increased, the weld line between the HDPE resins shrunk. It can be seen in Figure 4.29(e). It was noticed that the air pocket between the pellets flattened as the pressing continued.

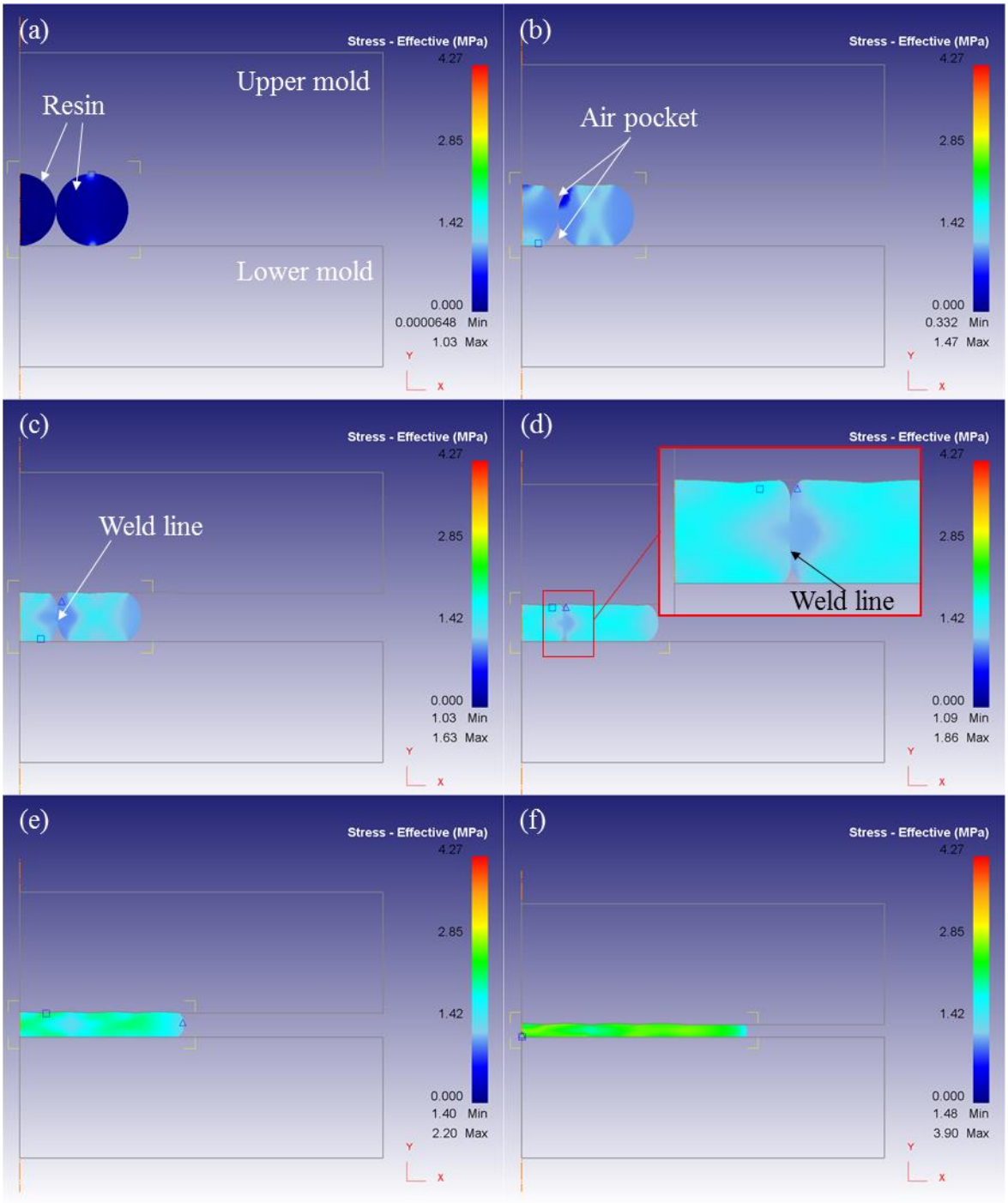

Figure 4.29: Press molding simulation at the pressing temperature of 133 °C.

According to Figure 4.30, on the other hand, the pressing stress reduced when the pressing simulation was formed with a temperature of 140 °C due to lower viscosity. The weld lines can be observed in Figure 4.30 (c) and (d). However, as the pressing distance increased,

a lower level of stress was recorded between the pellets when they were mixed. This phenomenon occurred because of the lower viscosity with a higher pressing temperature.

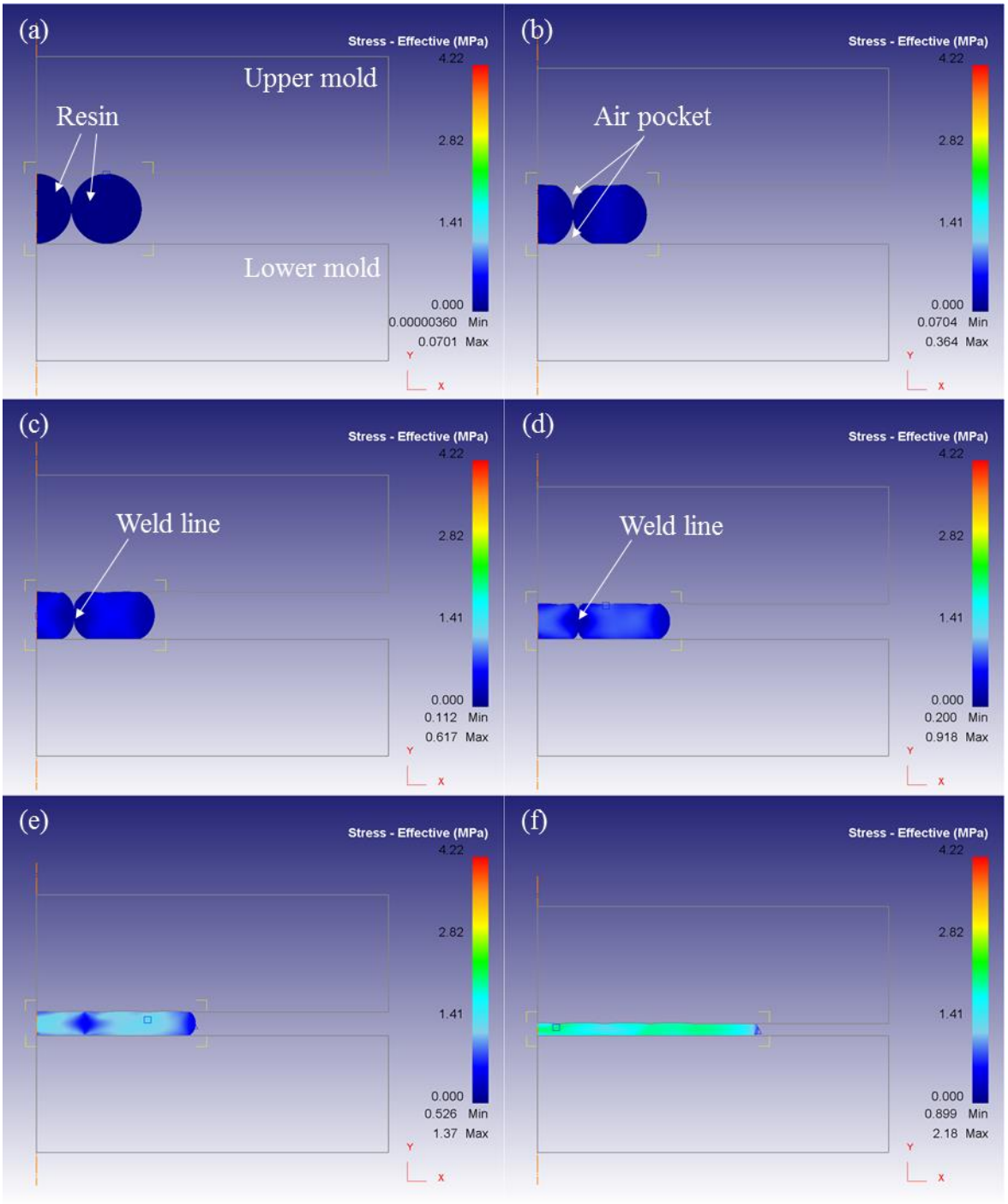

Figure 4.30: Press molding simulation at the pressing temperature of 140 °C.

Both simulation results were in line with the in-situ observation discussed in Section 4.1.5.2. Based on the observation, it was important to control the press molding temperature to

ensure that the HDPE pellets were mixed. In fact, press molding with a higher temperature could lower the stress of the polymer.

4.1.7 Trench formation on coating surface

It has been known that the mold coating will wear out due to the alternating stress during a hot embossing and press molding process [81]. In this study, the mold coating surface was examined after 80 cycles of press molding to investigate the impact of trapped air on the coating. Figure 4.31 displays scanning electron microscope (SEM) images of the mold coating surfaces. Trenches, which have similar patterns as those on the lens surfaces (see Fig. 4.20), are also formed on the mold coating surface. This fact indicates that the trenches formed on the lens surface due to the trapped air have affected the mold coating. The trapped air creates a non-uniform distribution of contact pressure, which consequently creates stress concentrations in the coating. Repetition of these non-uniform contact cycles will peel off the coated layer, thus creating trenches.

In addition to the trenches, the coating was also partially worn out, as illustrated in Figure 4.31(c). HDPE adhesion to the mold coating was also confirmed, as shown in Figure 4.31(d). Figure 4.32 presents the error distribution profile of the mold, after being used for 80 cycles. An average error of approximately 500 nm was formed relative to the original mold profile. This is caused by trench formation, coating wear, and HDPE adhesion.

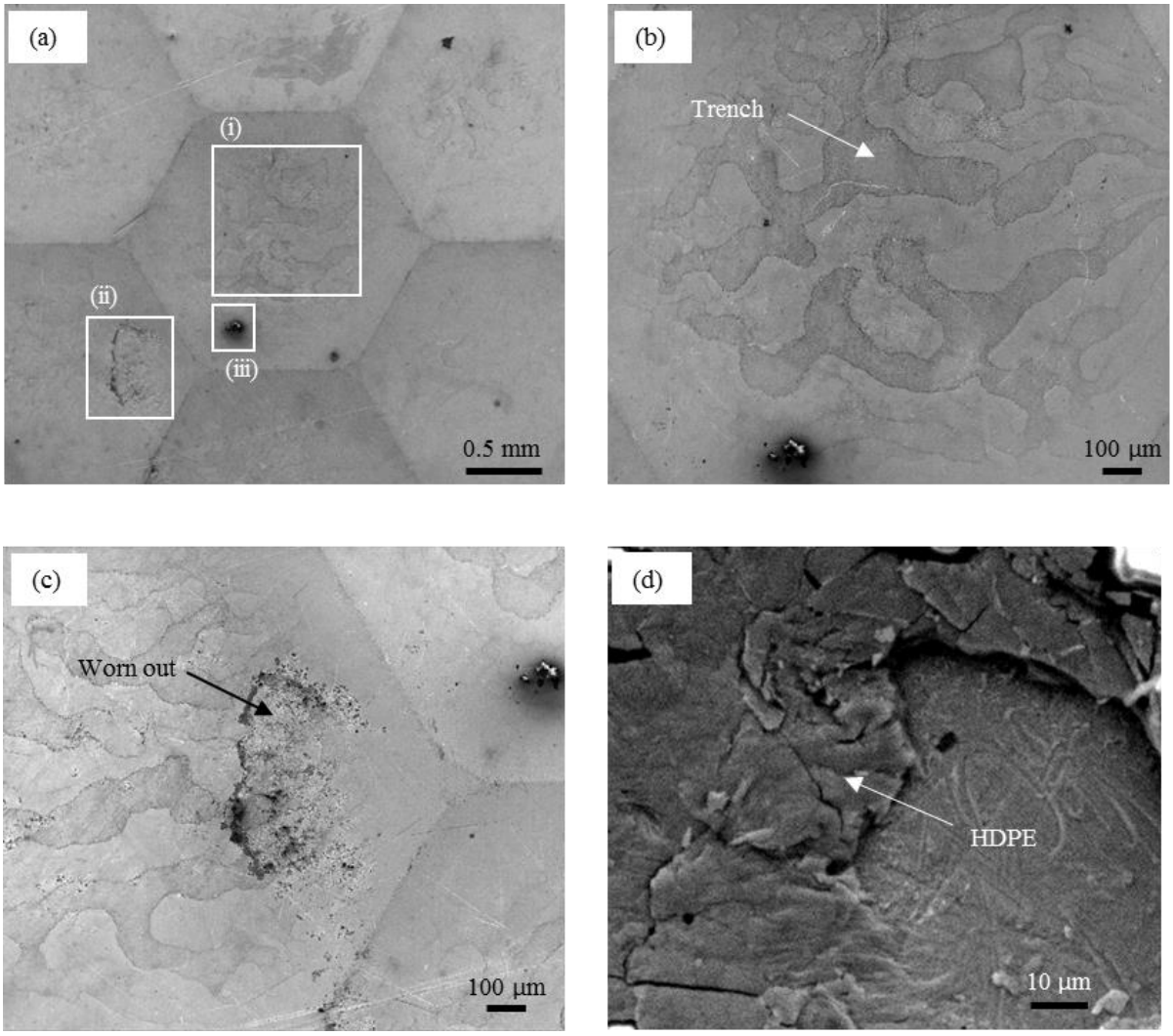

Figure 4.31: (a) Surface of mold coating; (b) magnified view of rectangle (i) showing trench formation; (c) magnified view of rectangle (ii) showing worn out of coating; (d) magnified view of rectangle (iii) showing HDPE adhesion.

The wearing out phenomenon might have been caused by the HDPE polymer and the coating itself. The HDPE used in the experiments contained silane, which is used to achieve adhesion between HDPE and Si. However, there have been reports that silane can be used to strengthen the bonding of PTFE to its substrate [82]. Therefore, the silane-crosslinked HDPE may have created an adhesion with the PTFE layer during molding. The repetition of contact and adhesion between the HDPE and the coating causes the wearing of the coating, especially during demolding. Silane may also react with the SiO_2 layer after the peeling off of the PTFE layer, because the wear resistance of the PTFE itself is limited [83]. Figure 4.33 presents the

worn out phenomenon of PTFE/SiO_2 coatings. In some areas of the figure, the PTFE/SiO_2 layer has been removed, leaving the exposed Ni mold surface.

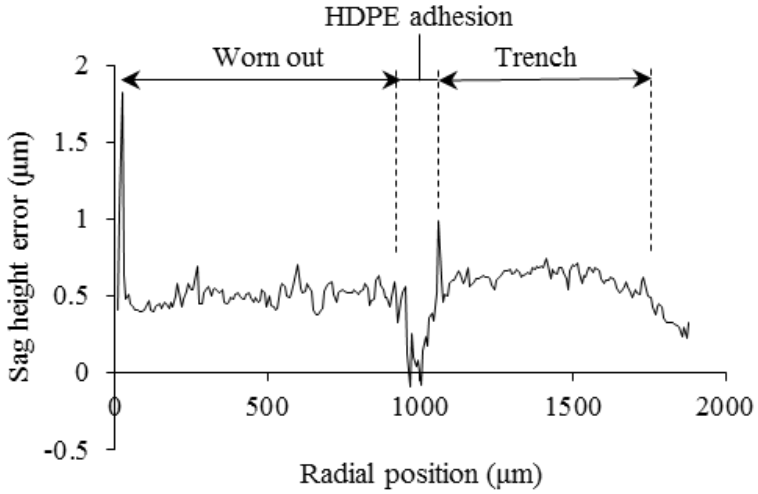

Figure 4.32: Cross-sectional profile of a micro-lens dimple on the mold, showing worn out, HDPE adhesion, and trench formation areas.

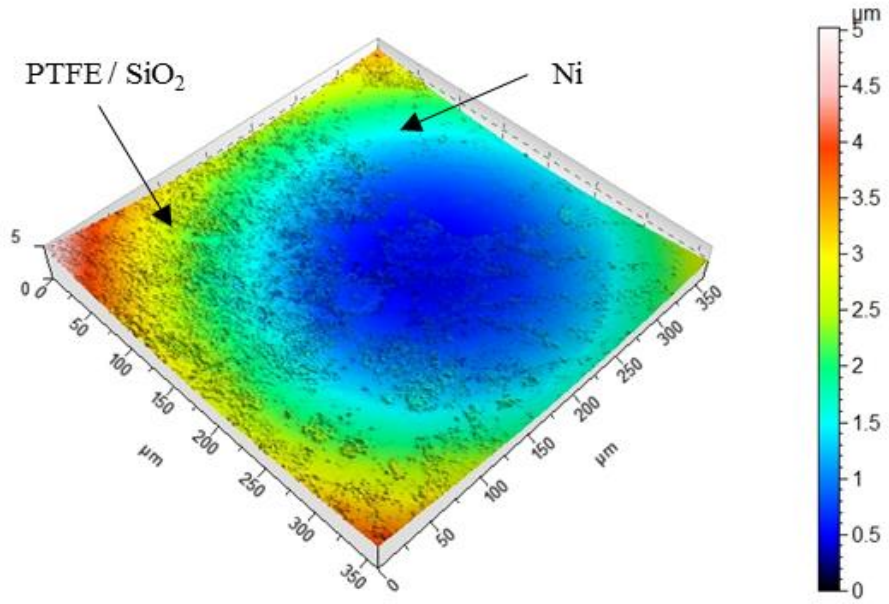

Figure 4.33: Three-dimensional topography of mold surface showing the wearing out of coating.

Meanwhile, a composition of the coating material has also been measured by energy-dispersive X-ray (EDX), as showed in Figure 4.34. The peak of PTFE (F), SiO_2, and Ni exist

in the spectra. However, the peak of Al is recorded as higher, demonstrating that most of the coating layer has worn out, and that the Al substrate was exposed.

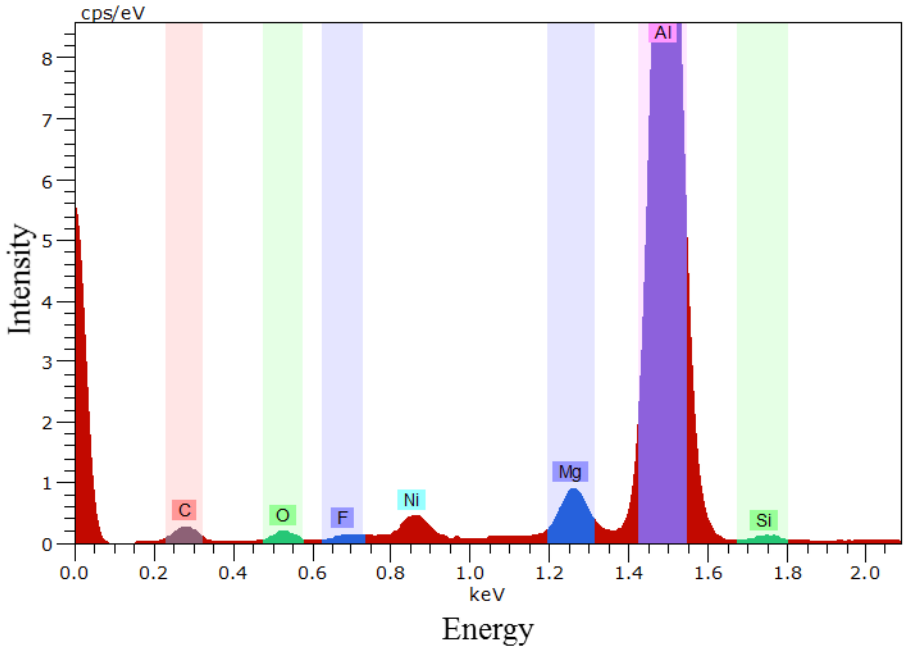

Figure 4.34: Energy-dispersive X-ray fluorescence of coated mold insert.

4.1.8 Press molding in vacuum environment

In order to resolve the air trapping problem, a press molding experiment was conducted in a vacuum environment using a newly developed press molding machine GMP-311V (Toshiba Machine Co. Ltd. Japan) that was equipped with a vacuum system. The pressing temperature was set to 140 °C while the pressing forces were set to 0.2, 0.4, and 0.6 kN respectively. The vacuum pressure was set to 0.1 Pa while the vacuuming time was 60 s. The rest of the press molding parameters were the same as the previous experiment in a non-vacuum environment.

In the vacuum condition, as no air pockets are formed among the HDPE pellets during molding, no air trapping-induced surface defects were observed on the lens surface, as shown in Figure 4.35. The press molded micro-lens array in Figure 4.35(c) displays perfect surface

topography. These results indicate that the press molding in a vacuum environment is crucial for achieving a high surface integrity without air trapping, even when using HDPE pellets as raw material.

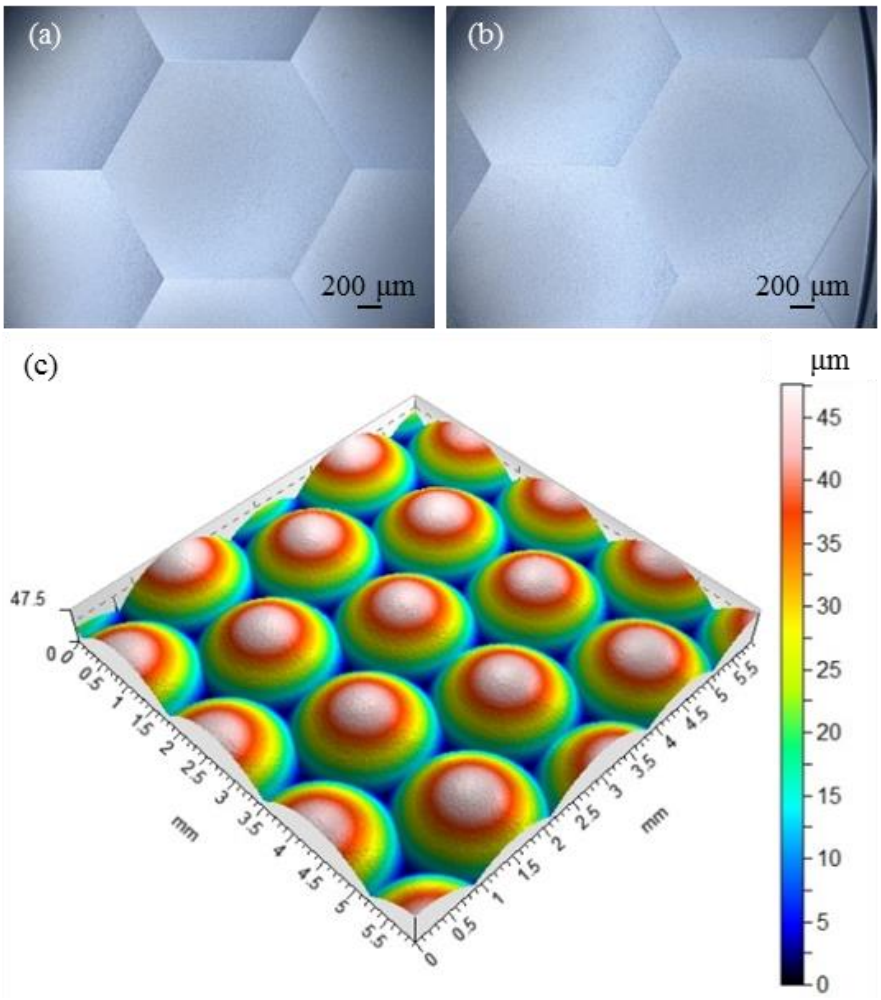

Figure 4.35: A press molded Si–HDPE hybrid lens array in a vacuum environment: (a) center region, (b) outer region, (c) three-dimensional topography.

4.1.9 Form accuracy improvement by shrinkage compensation

Finally, to further improve the form accuracy of the lens array, by achieving the targeted lens sag height (46 μm), HDPE shrinkage compensation was included in the mold sag height during mold design. From the result in Figure 4.12(b), it can assumed that the average sag height is 43.67 μm. From the mean result, the shrinkage value of the HDPE can be calculated. The shrinkage (*S*) value can be calculated using Equation 4.9:

$$S = (H - h)/H \tag{4.9}$$

where S is the shrink rate, H is the sag height, and h is the formed sag height. In this equation, the H is considered as 46 µm and h to be 43.67 µm. The following equation (Eq. 4.10) can be used to calculate the new sag height (S_n) of the new mold insert:

$$S_n = H/(1 - S) \tag{4.10}$$

Using this equation, the new sag height dimension for the new mold insert is calculated to be 48.5 µm (rounded-up to 49 µm). The new mold is fabricated with the sag height of 49 µm. Thus, when the lens is press molded with a new mold which included the shrinkage compensation, and formed in a vacuum condition, the target sag height of 46 µm is obtained, as presented in Figure 4.36.

As demonstrated in Figure 4.36, the lens sag height was improved to 46 µm, meeting the targeted value. The use of different pressing forces 0.4, 0.6, and 0.6 kN had no significant effect on the lens sag height. Figure 4.37 shows a photograph of pressed Si-HDPE hybrid lens arrays in the present study. The fabricated hybrid lens will be evaluated for IR imaging capabilities and this will be discussed in Chapter 5.

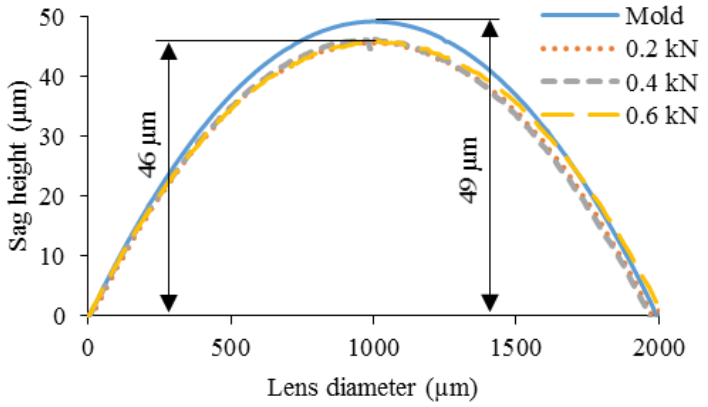

Figure 4.36: Lens sag height obtained at different pressing forces in a vacuum environment.

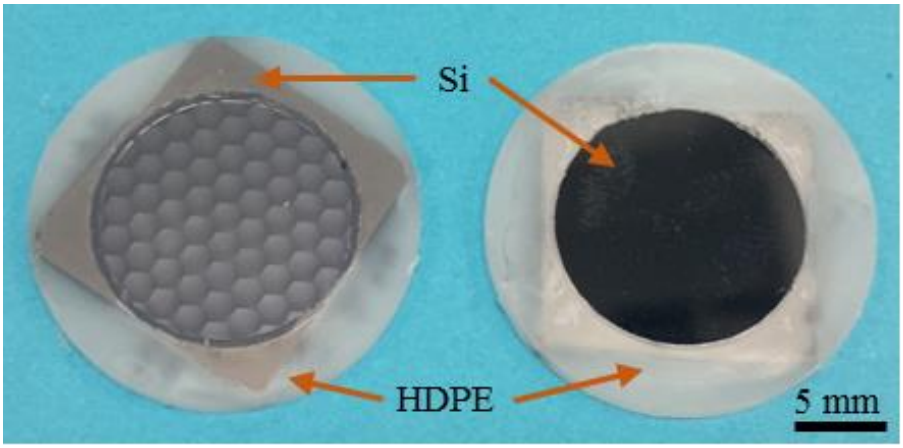

Figure 4.37: Photograph of two pressed Si-HDPE lens arrays, showing different sides.

4.2 Fresnel lens

A diffractive optics or Fresnel lens was created in 1665 by Francesco Maria Grimaldi and continues to be used in the optics design today [84]. It can also be used as the light collimator or concentrator, as well as in broadband IR optics [85,86]. Using the Fresnel shaped lenses is a cost effective method to produce a light weight lenses [15,87]. In the Fresnel lens design, the spherical or aspherical lens was cut into a series of a concentring rings, as demonstrated in Figure 4.38, but during which the lens characteristics are still maintained.

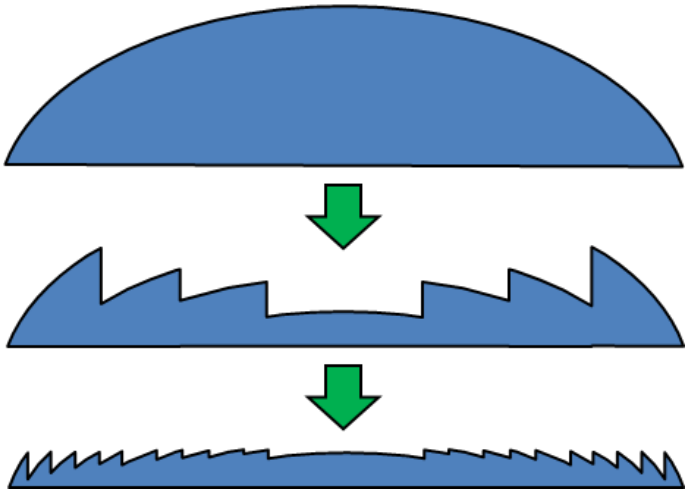

Figure 4.38: Collapsing spherical shaped lens into Fresnel shaped lens.

The used of the Fresnel lens design is also beneficial to this research, as the HDPE layer of the hybrid substrate is extremely thin, and thin lens needs to be formed. The Fresnel lens can be designed and formed on the hybrid substrate.

4.2.1 Fresnel lens design

A double lens system, which consists of a spherical and an aspherical plano-convex Fresnel lens, was designed using a Si-HDPE hybrid substrate. A two-side polished Si wafer with a thickness of 755 μm was cut into 15 × 15 mm squares, while the thickness of the HDPE laminating one side of the Si was 80 μm, making the total thickness of the hybrid substrate 835 μm. The thickness of HDPE needed to be maintained as thinly as possible to reduce IR absorbance.

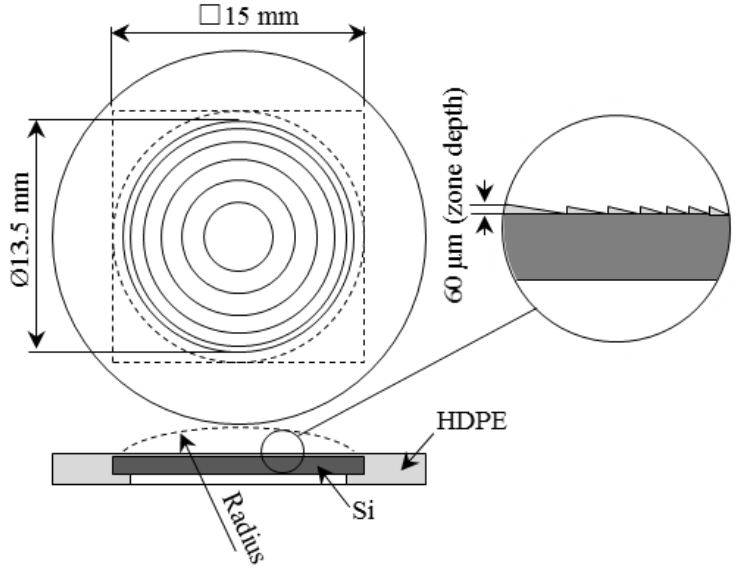

Figure 4.39: Si-HDPE hybrid Fresnel structures.

The first lens (Lens 1) was set to have a spherical shape with a lens curvature radius of 11.636 mm. Meanwhile, the second lens (Lens 2) of an aspherical shape was set to have a radius of 11.034 mm. Both lenses with the Fresnel structure diameter of 13.5 mm were formed on an 80 μm thick HDPE layer of the Si-HDPE hybrid substrate. The Si-HDPE hybrid micro

Fresnel lens structure design is shown schematically in Figure 4.39, and its parameters summarized in Table 4.4.

Table 4.4: Double Si-HDPE hybrid lens design parameters.

Parameters	Value
Lens radius (*R*):	
Lens 1 (Spherical) (mm)	11.636
Lens 2 (Aspherical) (mm)	11.034
Lens 2 conic constant (*k*)	– 2.813
Lens diameter (*D*) (mm)	13.5
Fresnel zone depth (*h*) (μm)	60
HDPE thickness (μm)	80
Si thickness (μm)	755

Figure 4.40 shows schematically the geometry of the surface of the Fresnel lens. The even aspherical lens curvature can be calculated using the aspheric lens equation, Equation 4.11, to define the profile, as follows:

$$Z(s) = \frac{Cs^2}{1 + \sqrt{1 - (1 + k)C^2 s^2}} + A_4 s^4 + A_6 s^6 + A_8 s^8 \qquad (4.11)$$

where *Z* is sag of the surface parallel to the Z axis, *s* is a radial distance from the optical axis, *C* is lens curvature (inverse of radius), *k* is the conic constant, and A_4, A_6, A_8 were the order of aspheric terms. In this study, A_4, A_6, A_8 were set to zero, and the conic constant (*k*) for the aspherical Fresnel lens of Lens 2 was set to – 2.813.

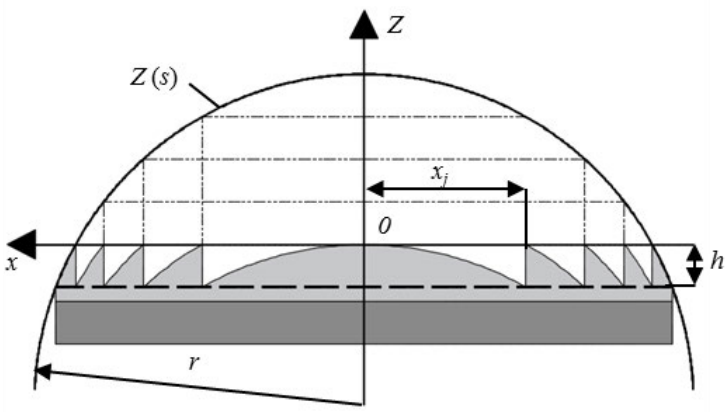

Figure 4.40: Schematic diagrams of Fresnel structure surface geometry.

The lens surface was divided into concentric rings by cylindrical surfaces at the zone steps. The radial coordinate (x_j) of each ring can be calculated using the following equation, Equation 4.12:

$$x_j = \sqrt{j.h\left(\frac{2}{C} - j.h\right)} \tag{4.12}$$

where j is the sequential number of the Fresnel zone counted from the centre of the lens axis (z), and h is the zone depth. In this case, h was set to 60 μm. Meanwhile, to prevent light reflection at the Fresnel zone side wall, no draft angle was designed. The lens design will be further discussed in Chapter 5.

4.2.2 Mold design and fabrication

The Fresnel lens structures were machined onto an aluminum mold insert using an ultraprecision diamond lathe, NanoForm X (Ametech Inc., USA), which was equipped with an air bearing spindle. A sharply pointed V-shaped single crystalline diamond tool with an angle of 60° was selected for the cutting process. A constant spindle speed of 2700 rpm was used to roughly cut the surface with a 2.7 mm/min feed rate and a rough-cut depth of 10 μm, in which six roughing tool passes were used. The spindle speed and feed rate were unchanged for the

semi-finishing cut, but the depth of cut was reduced to 4 µm. The feed rate was then reduced to 0.15 mm/min for finishing. Both the spherical and an aspherical Fresnel molds used the same cutting parameter. A photograph of both mold inserts is presented in Figure 4.41. Meanwhile, the surface roughness of the mold was 4.82 nm Ra, which was measured by using white light interferometer and TalyMap software.

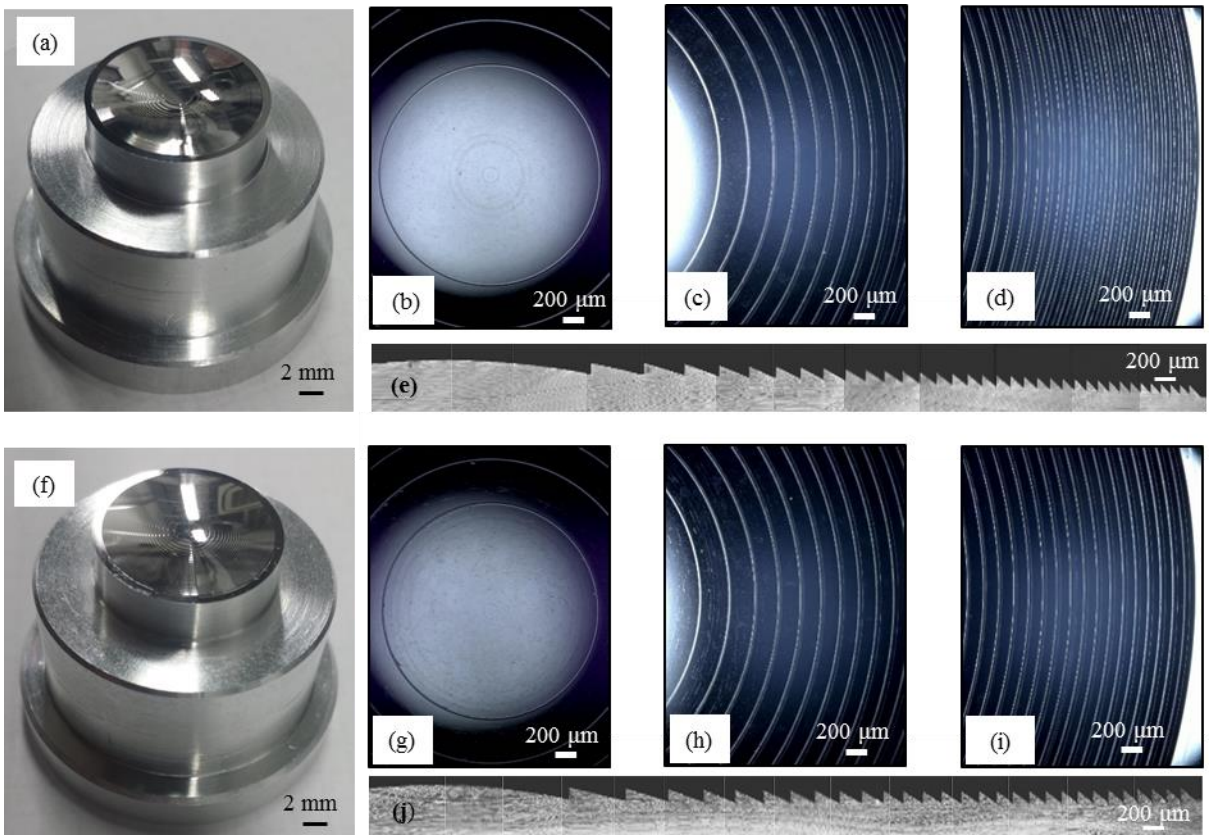

Figure 4.41: (a) Photograph of an aluminum mold insert with a spherical Fresnel structure, (b)-(d) microscope images of the spherical Fresnel structure, (e) mold insert cross section of a spherical Fresnel structure obtained by UV curing, (f) photograph of an aluminum mold insert with an aspherical Fresnel structure, (g)-(i) microscope images of an aspherical Fresnel structure, and (j) mold insert cross section of an aspherical Fresnel structure obtained by UV curing.

The sharp ridges of the Fresnel zone caused an error during the cross-sectional profile measurement using a laser measuring system, as displayed in Figure 4.42. It is also due to a spot at the bottom area of the Fresnel which cannot be reached by laser. Hence, the use of the laser measuring system is not suitable for measuring the mold.

When the Fresnel lens structures were machined on the mold, an ultraviolet (UV) curing resin was used to replicate the mold surface, as showed in Figure 4.43, and a cross-section cut was performed on the replicated resin for profile observation using a violet laser scanning microscope, VK-9700 (Keyence Co, Japan). It was equipped with a violet laser probe (wavelength 408 nm), which can scan surfaces three-dimensionally, while the vertical and horizontal resolutions are both 1 nm. The cross sections for both lens molds are provided in Figures 4.41(e) and (j). From the cross-sectional observations the Fresnel structure was found to be accurately fabricated using an ultraprecision diamond lathe with the zone depth of 60 µm.

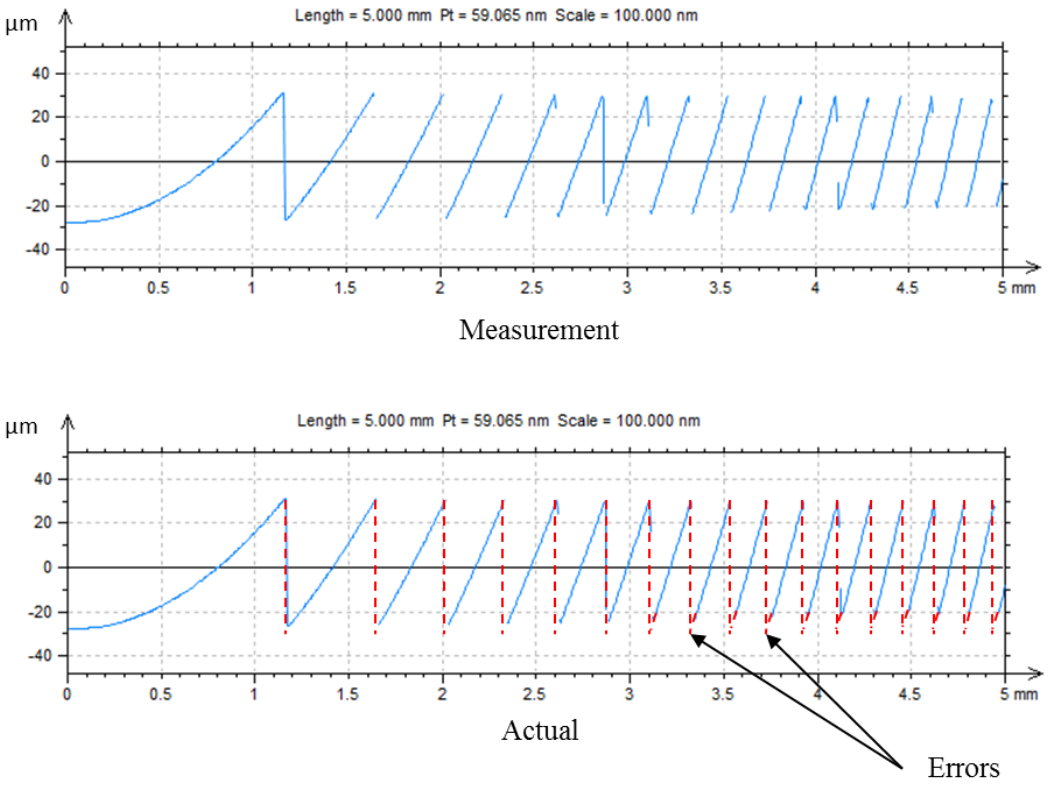

Figure 4.42: Measurement errors using non-contact measurement.

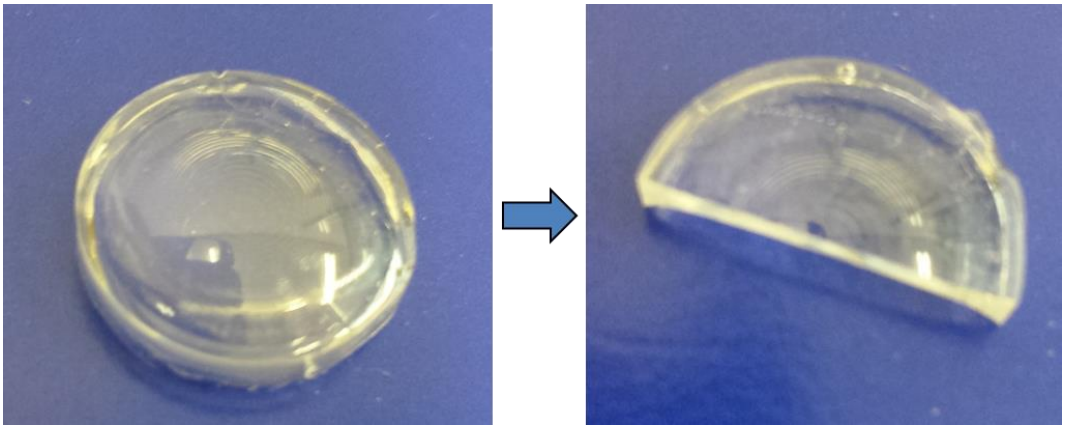

Figure 4.43: UV curing replication process and cross-sectioning method.

4.2.3 Press molding of Fresnel lens

4.2.3.1. Experimental setup

In the experiments, two steps of press molding were done as illustrated in Figure 4.44. The first step (Step 1) was pre-forming a flat Si-HDPE hybrid substrate using the same method as the previous discussion in Section 3.41 [61], as illustrated in Figures 4.44(a)-(c). In this way, the thickness of HDPE can be controlled up to ~80 μm. In the second step (Step 2) of press molding, the preformed hybrid substrate is heated above the glass transition (T_g) of HDPE, and the pressing process will take place.

The Step 2 processes are illustrated in Figures 4.44(d)-(f). Using this two-step method, the air trapping phenomenon that affects the resulting lens surface integrity can be minimized, as per previous research [88]. Air pockets were formed at the boundaries between the HDPE pellets and the Si substrate when the HDPE pellets were used in press molding. Thus, the use of flat-shaped HDPE is preferred.

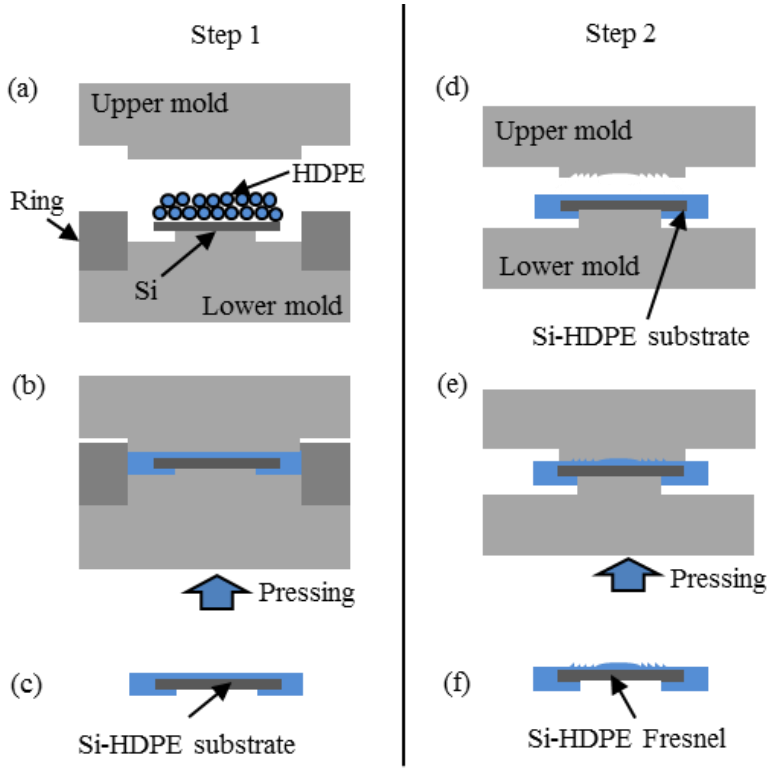

Figure 4.44: Press molding process of a Si-HDPE hybrid lens: (a)-(c) hybrid substrate press molding, and (d)-(f) press molding of the Fresnel structure.

4.2.3.2. Molding conditions

In Step 2, three different pressing temperatures were used (125, 128, and 130 °C respectively). A minimum pressing force of 0.2 kN was used to determine the best pressing temperature. Once the temperature was decided, the pressing force was varied from 0.4 to 1.2 kN. The zone depth of the Fresnel lens undergoing different pressing forces was compared to determine the best molding process parameters. In this study, the isothermal molding method was used, where both the mold and molded materials were heated to the same temperature [60]. The molding steps are summarized as follows:

1. A Si-HDPE substrate is placed into the mold cavity. The molding chamber is then closed.
2. The lower mold is raised closer to the stationary upper mold. A 2 mm gap is set between the upper mold and the hybrid substrate to enhance the heating process. To prevent

mold oxidation during heating, the chamber is purged with nitrogen gas for 20 seconds prior to pressing.

3. Both the mold and specimen are heated by an IR lamp at room temperature to the molding temperature at a heating rate of approximately 0.6 °C/second.
4. The temperature was then maintained for 100 seconds, followed by pressing until the mold is completely closed. The pressing force is set between 0.4 to 1.2 kN.
5. The pressing force is maintained while nitrogen gas is introduced into the chamber again for cooling at a rate of approximately 0.3 °C/second until the mold temperature was 90 °C. The pressing force is maintained during cooling.
6. Finally, the mold is opened and the molded Si-HDPE hybrid Fresnel lens is demolded and naturally cooled to room temperature. The time taken for a complete cycle of the press molding process is approximately 420 seconds.

4.2.4 Form accuracy evaluation

The Si-HDPE Fresnel lens was formed using press molding under different pressing temperatures. After demolding, the formed lens was replicated using a UV curing process to evaluate the accuracy of press molded microstructures. A cross-section cut was made to the replicated sample from which the Fresnel zone depth was measured. The variations of the zone depth molded at the pressing force of 0.2 kN and pressing temperatures of 125, 128, and 130 °C respectively are illustrated in Figure 4.45. As expected, higher press molding temperatures resulted in higher Fresnel zone depth because of the reduction of HDPE viscosity. The zone depth was measured at 10 ±0.309 and 16 ± 0.779 μm at the temperature of 125 and 128 °C, respectively. As the temperature increased to 130 °C, the zone depth increased to 20 ±0.682 μm. The result showed that 130 °C might be the suitable temperature for the present study. The higher the molding temperature, the better the form of accuracy [89].

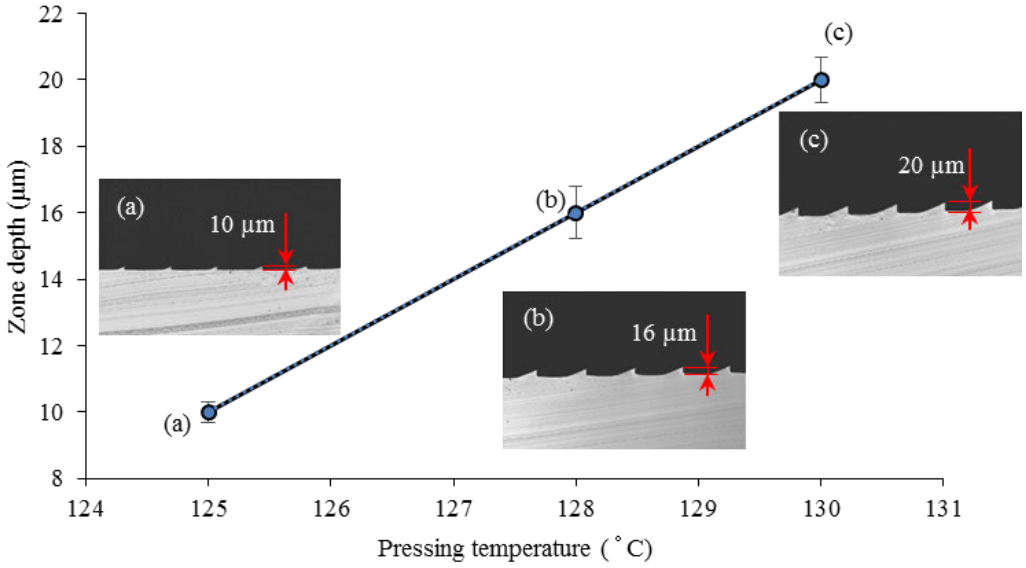

Figure 4.45: Zone depth change of the Fresnel structure for different temperatures under the pressing force of 0.2 kN.

Under the 130 °C pressing temperature, a series of press molding experiments was done using the pressing force varying from 0.6 to 1.2 kN. The microscope images of the formed Fresnel lenses are illustrated in Figure 4.46, where the images were divided into three sections: top views of centre and the outer region, as well as the cross-section view of the lens. In Figures 4.46(a)-(d), it was found that the centre area of the lens was incompletely formed for all pressing forces and an unformed area was observed. Also, rounded Fresnel edges were noticed at the outer area, as displayed in Figures 4.46(e) and (f), when it was formed at the pressing forces of 0.6 and 0.8 kN. This phenomenon might be due to insufficient pressing force and polymer recovery [90]. The increase of pressing force to 1.0 and 1.2 kN improved the lens structures, and rounded edges were eliminated, as illustrated in Figures 4.46(g) and (h).

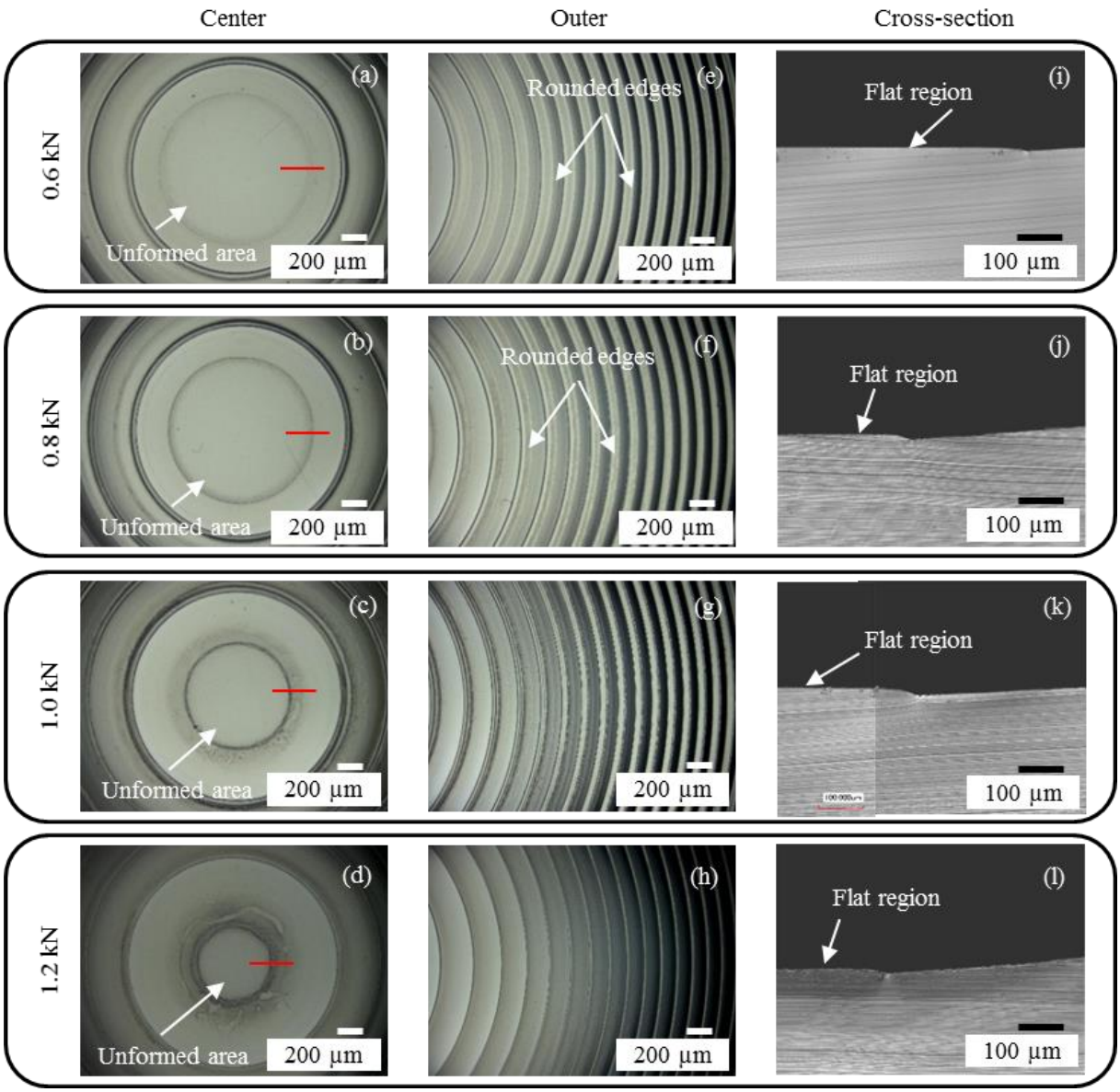

Figure 4.46: Microscope images of formed Fresnel lens under different pressing forces at a temperature of 130 °C.

For further investigations, the cross section of the centre area was made and illustrated in Figures 4.46(i)-(l). From these cross-section observations, it was found that some of the center areas remained flat for all pressing forces. As expected, the flat area decreased gradually when the the pressing force was increased. However, the increase of pressing forces up to 1.2 kN did not eliminate the flat area. This is due to insufficient pressing temperature.

To evaluate the dimensional accuracy of the press molded lens under 130 °C, a cross-section measurement of zone depth was done, and the results were plotted in Figures 4.47. The zone depth was measured at 22 ±0.339 and 46 ±0.141 µm when it formed at a pressing force of 0.6 and 0.8 kN respectively. As the pressing force increased to 1.0 and 1.2 kN, the zone depth increased to 53 ±0.230 and 54 ±0.304 µm. Although the pressing force increased, the target zone depth of 60 µm was not achieved. From this outcome, the pressing temperature of 130 °C is unsuitable for achieving form accuracy.

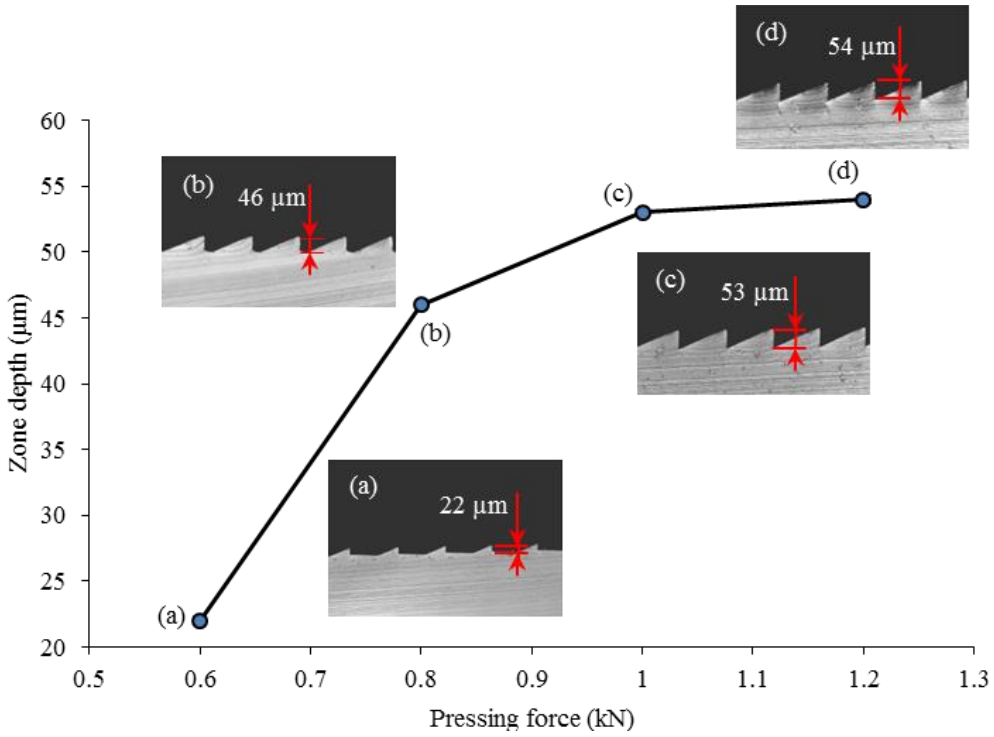

Figure 4.47: Zone height of the Fresnel under different pressing forces at a temperature of 130 °C.

Next, the pressing temperature was increased slightly to 131 °C, and a press molding experiment was performed. The temperature (131 °C) was selected as the usage of higher temperatures resulted in higher polymer shrinkage, thus the form accuracy will be affected [47]. Figure 4.48 shows microscope images of the Fresnel formed at the pressing forces of 0.4 to 1.0 kN. The rounded edges were significantly reduced for all pressing forces compared with previous experiments (see Fig. 4.46). This phenomenon is due to the low

viscosity of the polymer, which allows the polymer to flow smoothly inside the cavity [47]. Meanwhile, an unformed area persisted at a pressing force of 0.4 kN, as shown in Figure 4.48(a). The unformed area was reduced by gradually increasing the pressing force to 0.6 and 0.8 kN respectively, as illustrated in Figures 4.48(b) and (c). The unformed area was completely eliminated when 1.0 kN of pressing force was used, as demonstrated in Figure 4.48(d). This was also confirmed by the cross-section observation in Figure 4.48(l), whereby the Fresnel curvature was obtained and the flat area was eliminated.

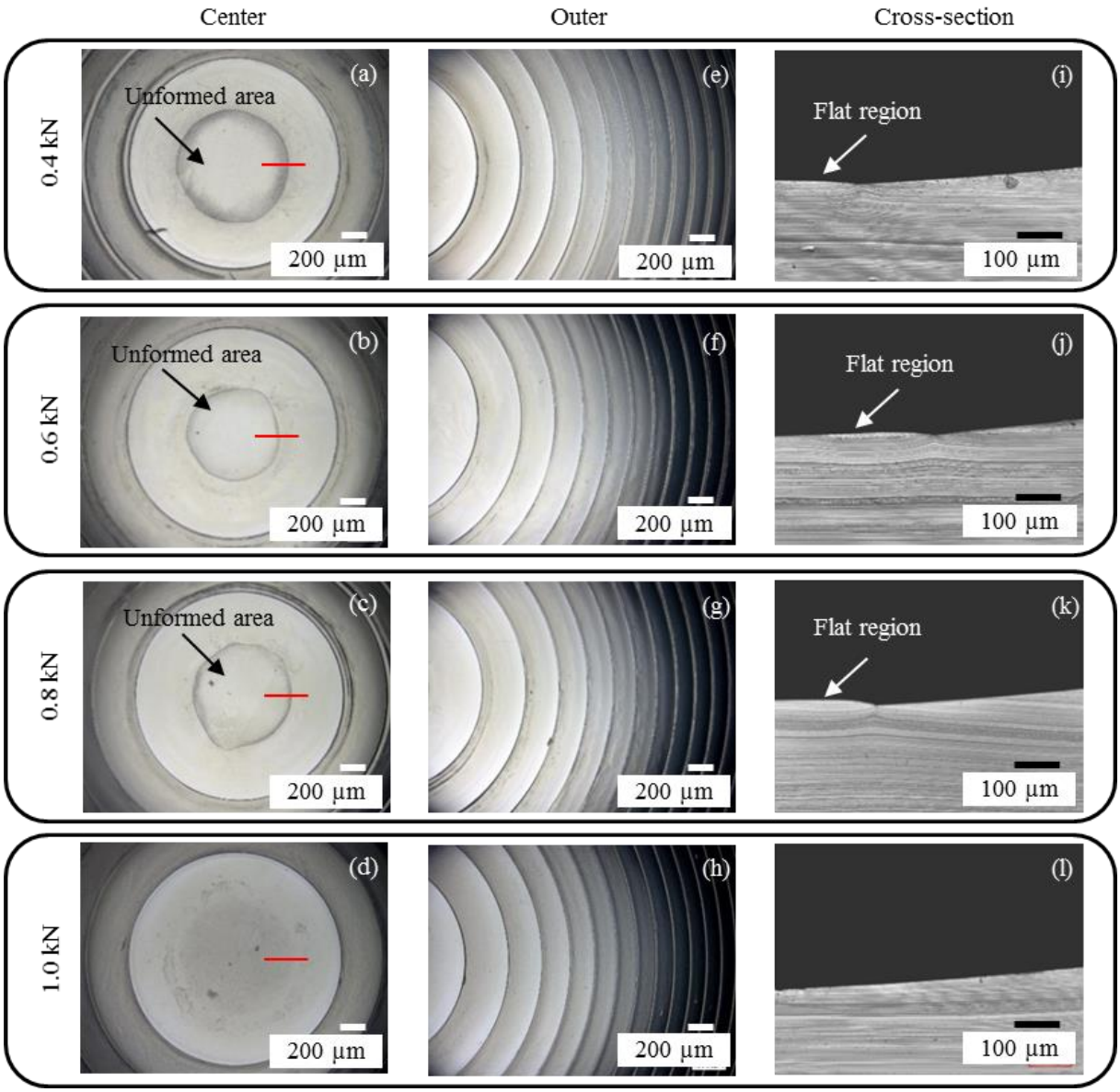

Figure 4.48: Microscope images of formed Fresnel lens under different pressing forces at a temperature of 131 °C.

Figure 4.49 shows the change of the zone depth of the Fresnel lens formed at the pressing temperature of 131 °C. The zone depth was 57 ±0.158 and 57.6 ±0.083 µm when the pressing force was 0.4 and 0.6 kN. As the force increased to 0.8 kN, the zone depth increased to 58.3 ±0.070 µm. The Fresnel lens was accurately formed at the pressing force of 1.0 kN, and the zone depth of 60 ±0.083 µm was obtained precisely. These results demonstrate that the form accuracy depends on the pressing temperature, similar to hot embossing [89]. Figure 4.50(a) displays the cross-sectional profile of the formed Fresnel. It can be seen that the lateral structures of the lens were also formed precisely. Based on these results, it is estimated that the press molding temperature of 131 °C and the pressing force of 1.0 kN are the optimal molding parameters for the Fresnel lens in this research. Under such conditions, the surface roughness of 6.78 nm Ra was achieved on the molded lens. Figure 4.50(b) is a photograph of a formed Si-HDPE hybrid Fresnel lens and a coin for comparison of size.

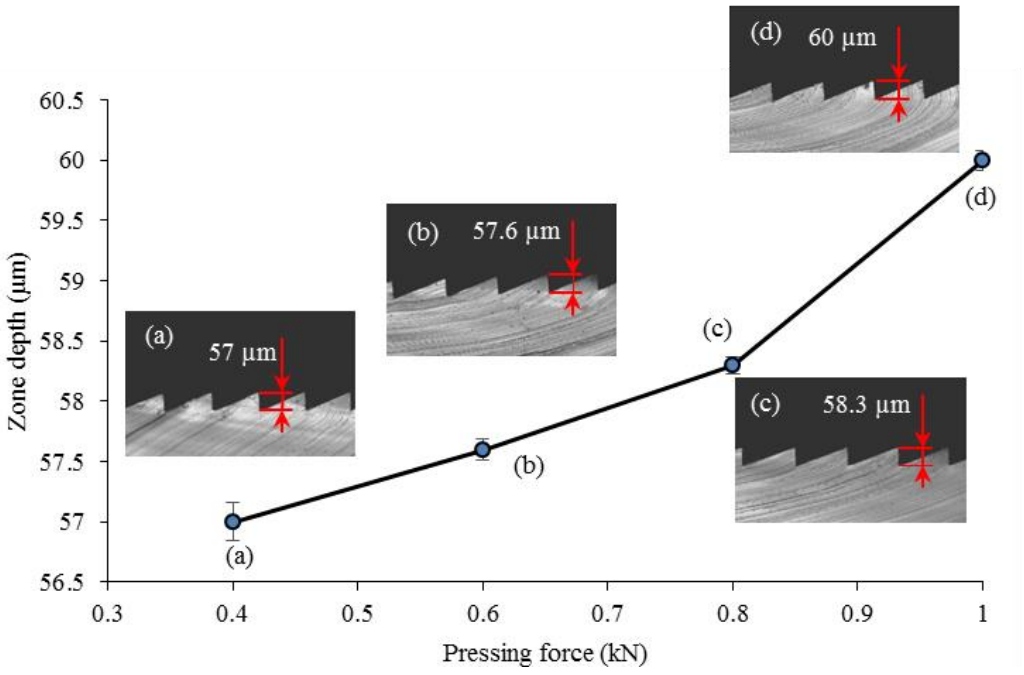

Figure 4.49: Zone height of the Fresnel under different pressing forces at a temperature of 131 °C.

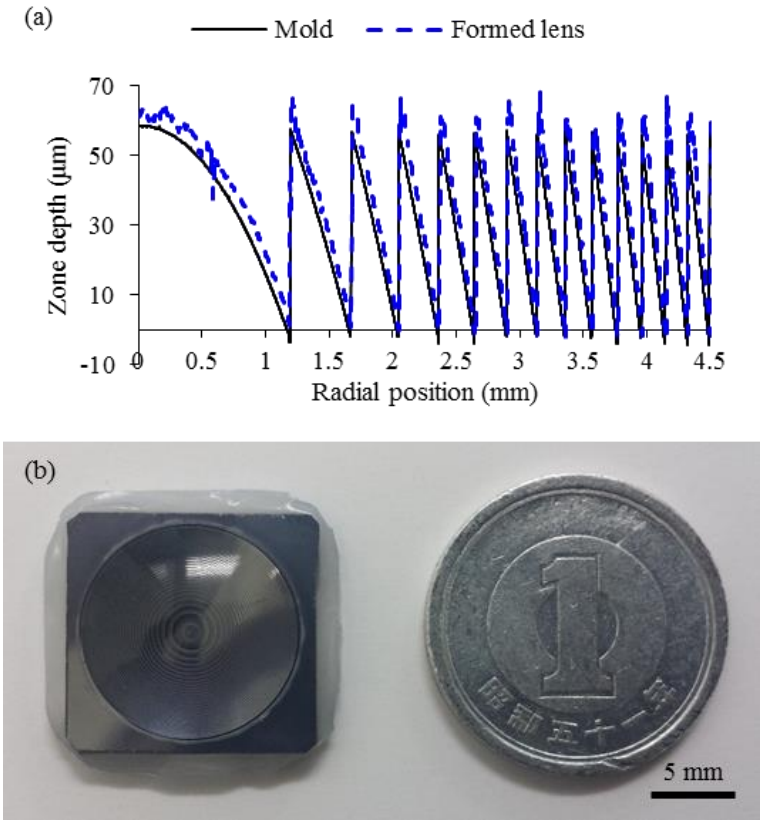

Figure 4.50: (a) Cross-sectional profile of lens geometry, (b) a press molded Si-HDPE hybrid Fresnel lens and a Japanese coin.

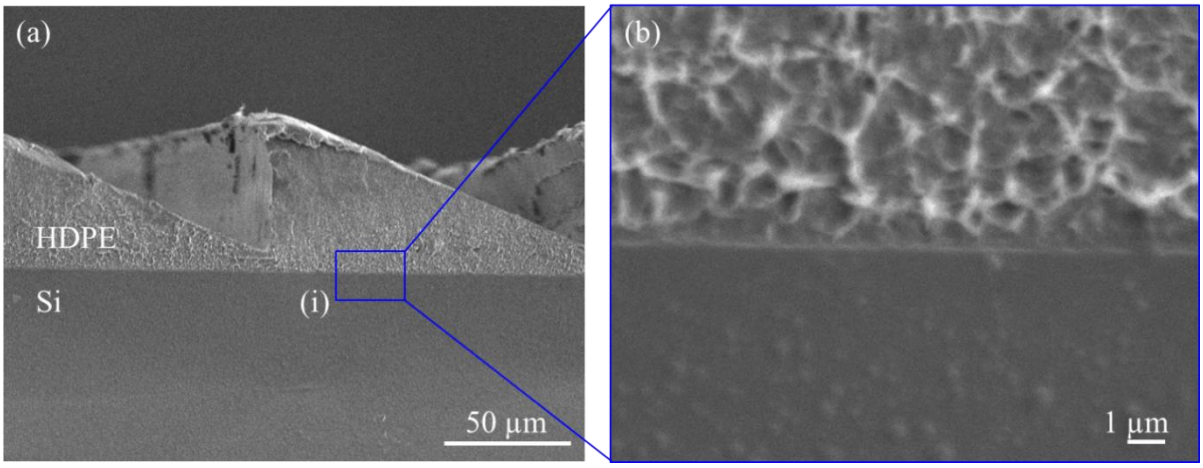

Figure 4.51: (a) Cross-sectional SEM images of a Si-HDPE Fresnel lens; (b) magnified view of rectangle (i) showing the interface.

To examine the interface between Si and HDPE after press molding, a press molded Si-HDPE Fresnel lens cross-section was observed using a scanning electron microscope (SEM). Figure 4.51 shows the cross-sectional SEM images of the sample. No gap is seen between the

two materials, which demonstrates that the HDPE has bonded directly to Si during press molding by crosslinking binding [61].

4.2.5 Numerical simulation of Fresnel press molding

A numerical simulation was conducted to investigate the flow of the polymer during the Fresnel press molding. Another purpose of this simulation was to examine the formation of the flat region area on the lens centre. The same numerical method of press molding simulation as discussed in sub-section 4.1.6 was applied in this simulation. Figure 4.52 illustrates the schematic diagram of the simulation setup.

In the simulation, the boundary between the HDPE and the Si was considered as non-slip condition since the HDPE was adhered to the Si. As shown in Figure 4.52, the radial coordinate, x_j, was calculated according to the Eq. 4.12. Meanwhile, a radius of 0.1 µm was added to the sharp ridges of the diffractive edges to ensure the smoothness of the simulation. At the same time, a pressing temperature of 131 °C was applied.

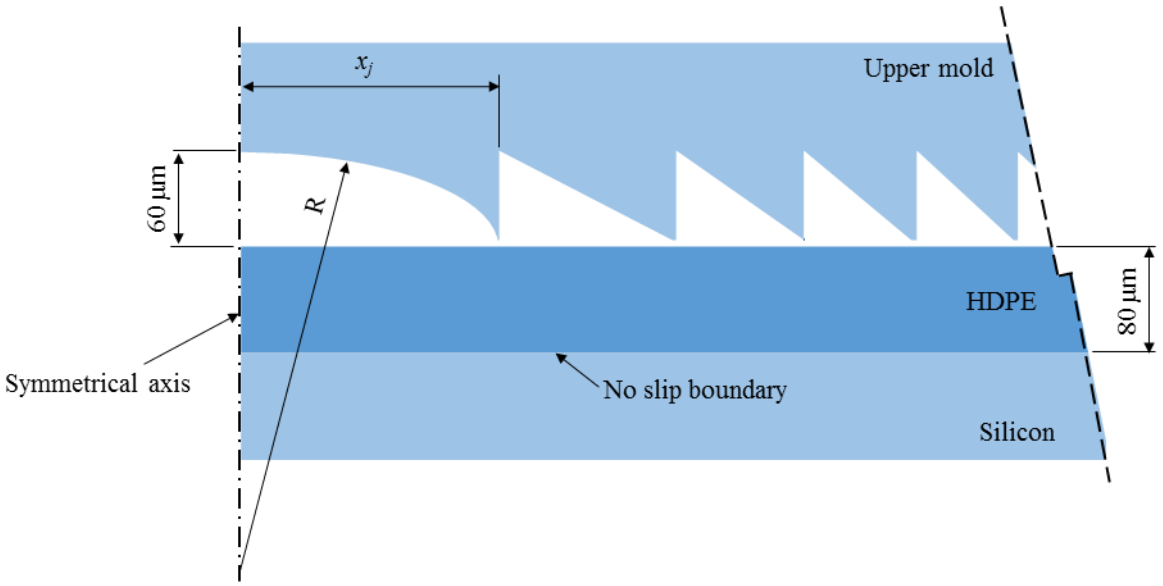

Figure 4.52: Schematic diagram of Fresnel press molding simulation setup.

Based on the numerical simulation, as the pressing took place, the polymer started to fill the diffractive area. Figure 4.53(a) portrays the polymer flew inside the diffractive cavities. It was also noticed that the rounded edges at the Fresnel edges were formed when the pressing continued as pictured in Figure 4.53(b). This phenomenon was closely related to the rounded edges of the cross-sectioned images, where the radius was formed when pressing temperature and force were inadequate.

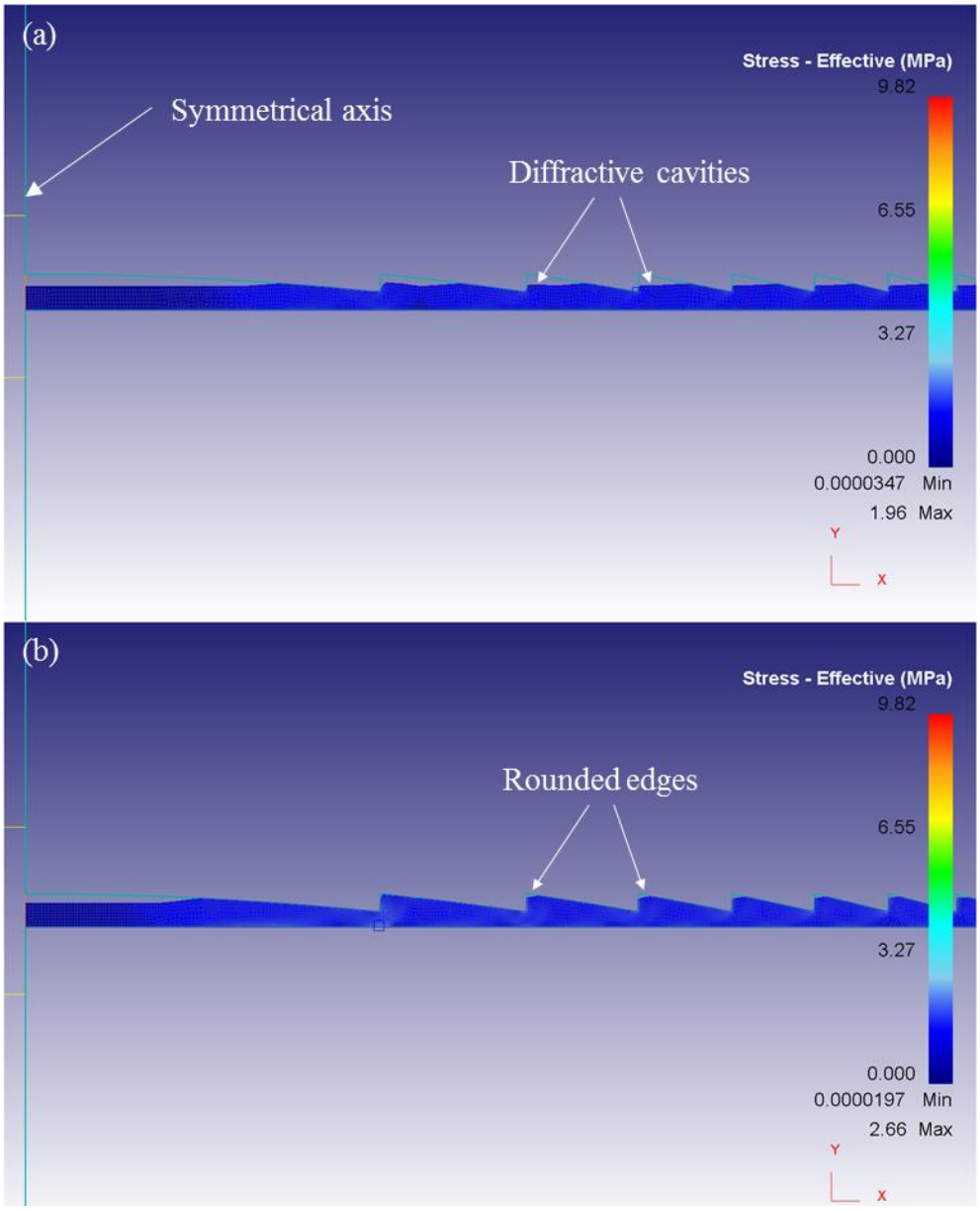

Figure 4.53: Cavities filling of the Fresnel during initial press molding step.

In the meantime, when the distance between the upper and lower mold reduced, the rounded corner of the diffractive edges gradually reduced and became sharper as described in Figure 4.54. The polymer completely filled the diffractive cavities at this stage of press molding, but the centre area of the Fresnel remained flat. Furthermore, a higher level of stress was also observed, which was likely to cause incomplete filling at the centre area. This phenomenon took place when a lower pressing force and temperature were utilised during press molding.

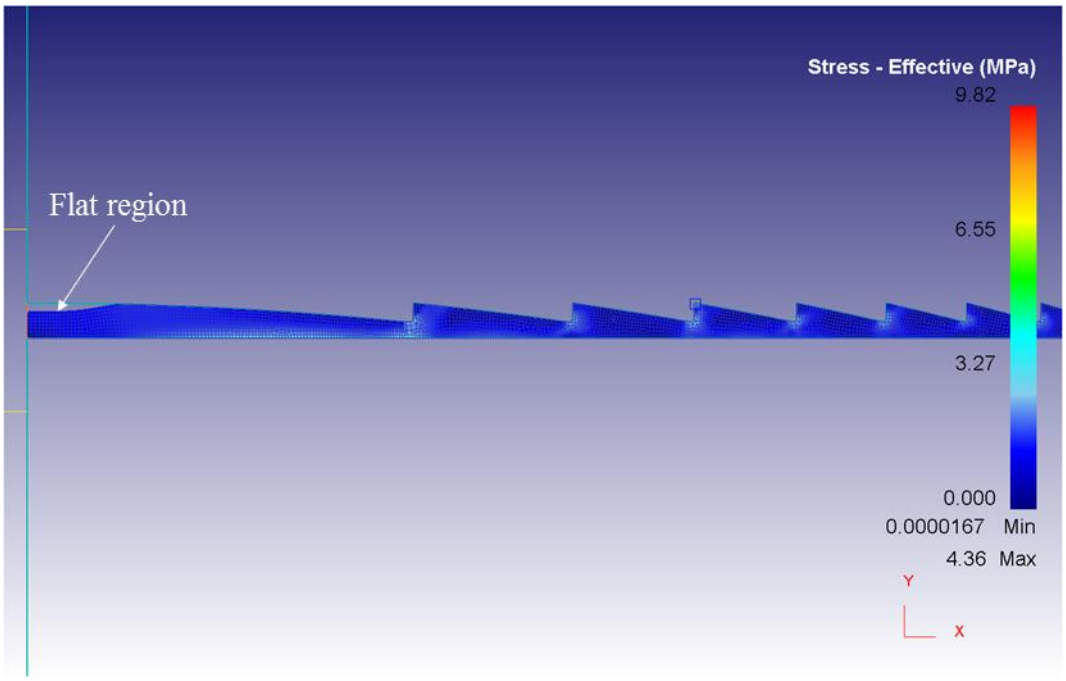

Figure 4.54: Flat region formation of the Fresnel during press molding.

When the pressing continued, the polymer completely filled the centre cavity of the Fresnel lens as portrayed in Figure 4.55. This condition could be obtained with higher pressing force and temperature as discussed in the previous section (Section 4.2.4). Based upon this simulation result, the behaviour of the polymer flow was apparent during the experimental condition.

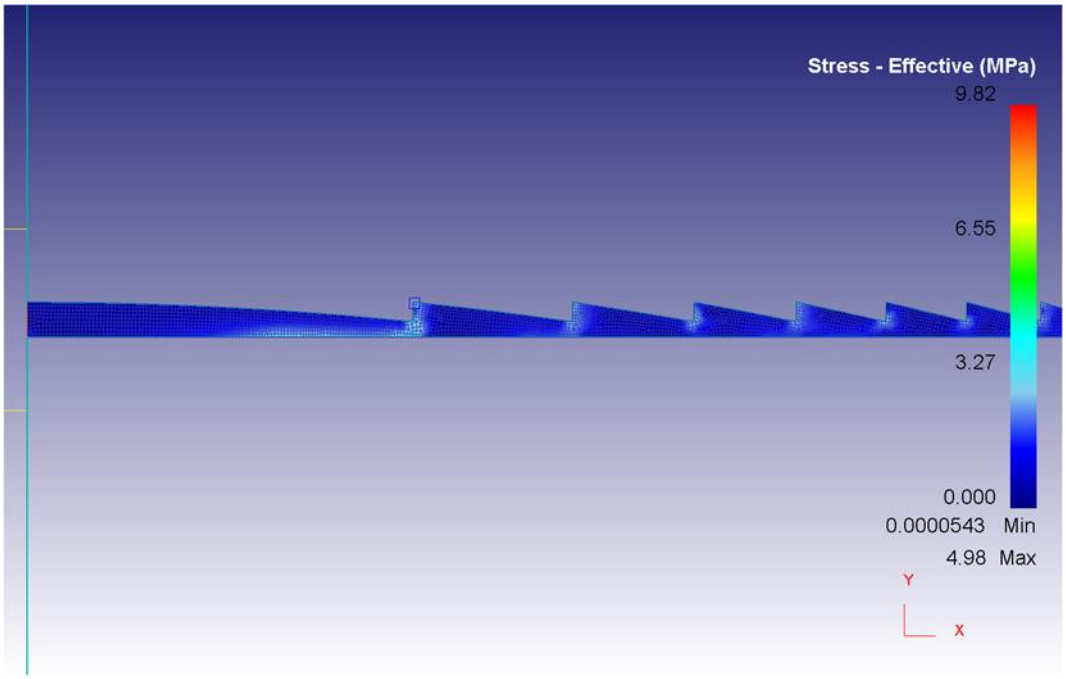

Figure 4.55: Complete filling of the Fresnel cavities.

4.3 Chapter summary

Si-HDPE hybrid micro-lens arrays and Fresnel lens were formed by press molding under various conditions, and the form accuracy and the surface integrity of the fabricated lenses were evaluated. The following conclusions were obtained:

1. The mold with a plunger helps to improve the lens form accuracy. The plunger increases the cavity pressure and contributes to compensate for HDPE shrinkage during the cooling stage.
2. Air trapping and trench formation occur in the centre region at a low pressing force, and in the outer area of the lens array at high forces. They are reduced when the pressing temperature increases.
3. By using the developed in-situ direct observation unit, the air trapping phenomenon during press molding was investigated. Air pockets were formed at the boundaries between the HDPE pellets and the Si substrate, and are flattened during the pressing

process, forming trenches on the lens surface. Weld lines are formed at the boundaries among the HDPE pellets when pressing at 133 °C. Increasing the temperature to 140 °C minimizes the weld lines. A good agreement also presented with the numerical simulation result and the formation of the weld lines also clearly indicated in the simulation.

4. Air trapping in molding press greatly affects the mold coating surface. Trench formation, wear marks and HDPE adhesions occur on the mold coating surface.
5. Molding a Si-HDPE micro-lens array in a vacuum environment helps to improve the lens surface integrity by completely eliminating air trapping and trench formation.
6. By compensating the HDPE shrinkage in the mold shape design, the lens form accuracy is greatly improved.
7. Fresnel structures were precisely formed on an 80 μm-thick layer of HDPE to form an ultrathin Si-HDPE hybrid infrared lens, which has a total thickness of ~800 μm. Such a thin IR lens has not yet to be reported in the literature.
8. The lens form accuracy depends on pressing force and temperature. Increasing both parameters improves the Fresnel shape transferability. A molding temperature of 131 °C and a pressing force of 1.0 kN were the optimal molding parameters for the Fresnel lens under the present experimental conditions. The numerical simulation conducted also explained the phenomenon during the pressing, where the flow behaviour of the polymer is studied.

CHAPTER 5

Infrared imaging evaluation

In this chapter, the fabricated micro lenses that were discussed in the previous chapters are analysed to investigate the applicability of the lenses for IR technology. Specifically, this research aims to evaluate the applicability of the Si-HDPE hybrid micro lens during IR imaging. Several tests and evaluations were conducted, including the lens analysis using optical design software, and conventional lens measurement.

An optical design software is proven in simulating and assisting the lens design performance. Several types of optical design software with different capabilities were considered. In this research, version 14 of Zemax OpticStudio (Zemax) software was chosen. It is a versatile software and is able to simulate the designed lens system's performance. Utilizing the software, the lens performance such as the ray trace, aberration, and contrast was analysed. The simulation data obtained from the software were also compared with conventionally measured lens performance.

In order to evaluate the IR imaging capabilities of the designed and fabricated lens, the lenses were assembled with a home built IR imaging system. A unique design of IR imaging systems is mainly to determine the utility of Si-HDPE hybrid in standard IR imaging, night mode IR imaging, as well as thermography imaging.

5.1 Micro lens array

The first IR imaging evaluation is conducted with the Si-HDPE micro lens array previously fabricated. If the micro lens design is to be used as an IR sensor, the abilities of the lens need to be evaluated. However, the used of the micro lens array for night mode imaging might be inappropriate due to the small size of the lenses. Thus, for this first lens design, that aspect of the evaluation will receive less emphasis.

5.1.1 Lens design evaluation

The micro lens array was designed to have a 10 mm radius and a 2 mm diameter. The sag height of the lens is 46 μm. The focal length of the micro lens array was calculated before it was attached to the imaging equipment. This is done to ensure that the lens is positioned at the actual focal length position during the IR imaging.

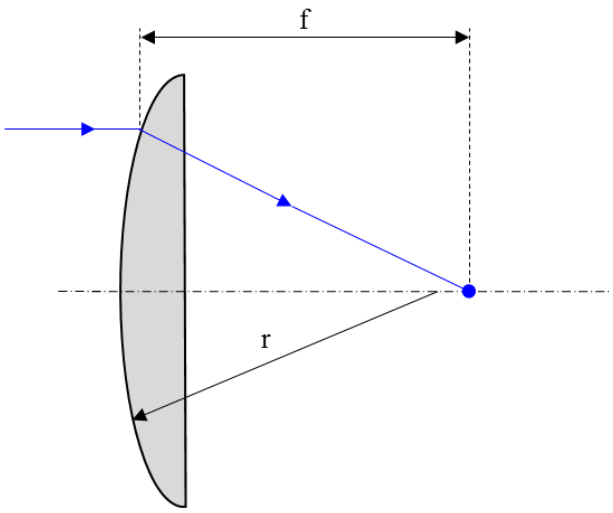

Figure 5.1: Schematic diagram of focal length.

Generally, the focal length is the distance from the lens to where an idealized collimated input beam converges to a point. To calculate the focal length, a thin lens maker formula (Eq. 5.1) was used as follows and illustrated in Figure 5.1:

$$\frac{1}{f} = (n_{lens} - 1)\left(\frac{1}{r}\right) \tag{5.1}$$

where n_{lens} represents the refractive index of the lens material, and r is the radius curvature of the lens. In the calculation, only the refractive index of HDPE is considered. This is due to the Si used being flat shaped, and thus powerless in this respect. The focal length of the micro lens by calculation is ~20 mm.

The lens design was also analysed with the Zemax software, to investigate the light's characteristics when it passes through the lens. The ray trace of the lens was illustrated in Figure 5.2. From the figure, it can be seen that the ray was well pointed to the focal point. However, the other lens characteristics are not given priority in this lens design.

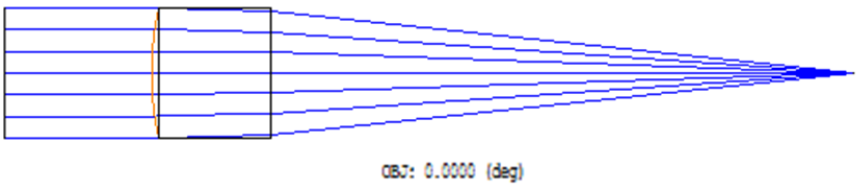

Figure 5.2: Ray trace of microlens array.

5.1.2 Imaging setup and image evaluation

To evaluate the Si-HDPE micro lens array application for IR imaging, a home built IR imaging instrument was designed as displayed in the schematic diagram of Figure 5.3. The instrument consists of an IR camera, an adjustable single axis linear table, and an IR emitter. The Si-HDPE micro lens array fabricated in the experiment was attached to the linear axis table in order to obtain the required focal length during the imaging, which is 20.95 mm. The linear axis table can be moved along the equipment table. In the imaging evaluation, a letter 'E' was used as the image mask and cut from 80 µm aluminum, and attached to 755 µm Si.

In order to capture the 'E' letter image, the Therm-App smartphone thermal camera (Opgal Optronic Industries Ltd.) with 384 × 288 pixels of resolution, and equipped with a 17

μm thermal detector. On the opposite side of the IR camera, an IR emitter (IR 43, Hawkeye Technologies, USA) with Ø12.7 × 16.4 mm parabolic reflectors was used, and placed behind the image mask. The wavelength of the emitter was in between 2-20 μm and powered by 9 volts power. The distance between the image mask and the camera was set to 134 mm. The actual setup for the imaging instrument is shown in Figure 5.4.

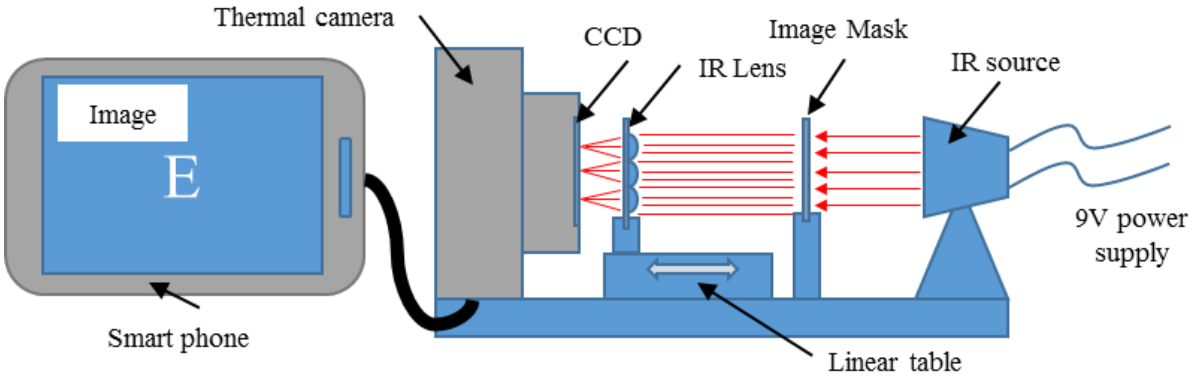

Figure 5.3: Microlens array imaging stage setup.

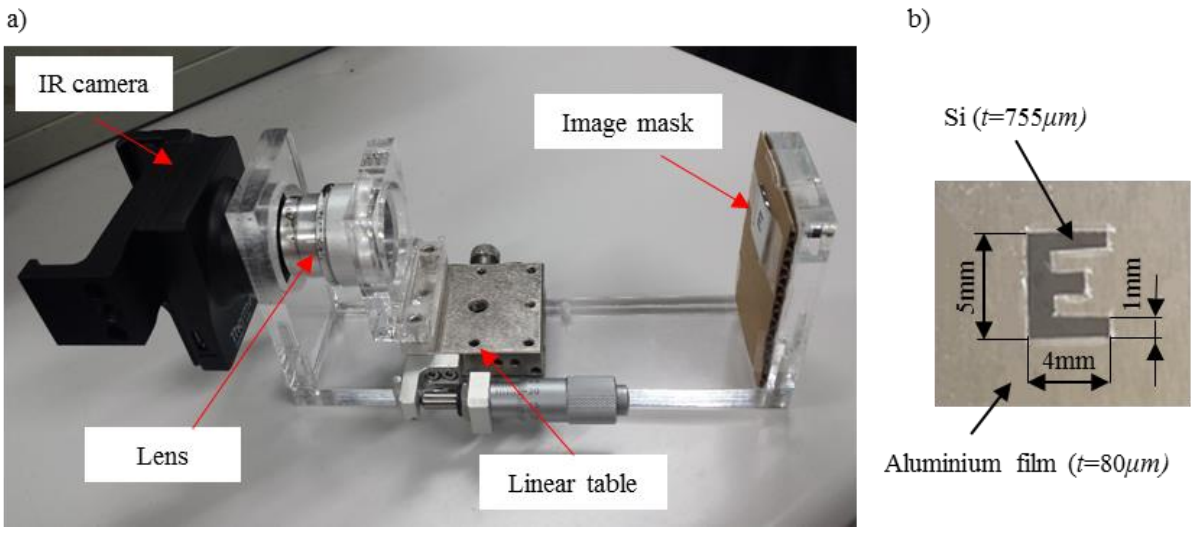

Figure 5.4: Photograph of (a) IR camera attached to the imaging stage, and (b) letter 'E' image masking.

5.1.2.1. Image evaluation

An IR imaging was conducted using home built IR imaging equipment, and the images of the ‘E’ letter were captured and illustrated in Figure 5.5. The image was obtained after the linear table of the imaging equipment was adjusted manually to the required focal length. From the figure, it can be observed that the IR image of the image mask is clearly identified and visualized. With the imaging result, the applicability of the Si-HDPE hybrid micro lens array was confirmed.

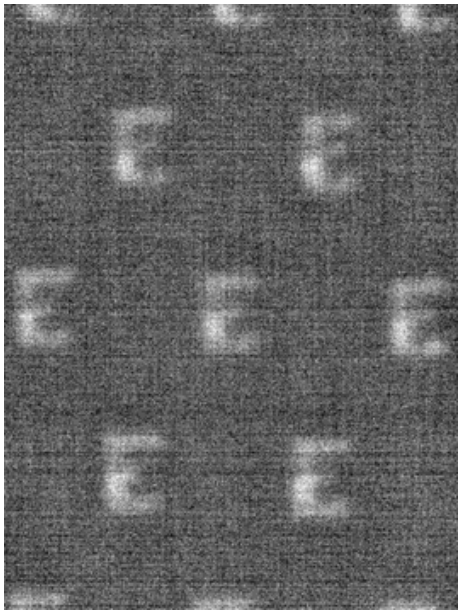

Figure 5.5: Image of ‘E’ letter captured by using Si-HDPE micro lens array.

5.2 Double Fresnel lens

The second lens design, the double Fresnel lens imaging system are designed and evaluated in this study. This lens design is mainly focused on night mode IR imaging and thermography. The used of the double Fresnel lens is due to the used of single Fresnel lens will contribute to the image aberrations [24]. The light enters the Fresnel structures are subjected to the reflection especially at the wall and the diffractive surfaces. To overcome the problem, multiple lenses is designed [91].

The Si-HDPE hybrid Fresnel lens in the system compromised a two different lens design. The first lens is set as the spherical lens while the second lens is an aspherical lens. As the first lens is subjected to the image aberration, the second aspherical shape lens can correct aberration. The addition of the second lens to the lens systems also can make the focal distance shorter compared to the single lens, thus higher image resolution can be achieved.

5.2.1 Determination of refractive index

During the initial stage of the lens design, it is very important to define the refractive index of the material. The refractive index will differ from one material to another, and it will indicate how the light bends and passes through the lens material.

The refractive index is an important factor in lens design. The refractive index of Si was obtained from the Zemax software library and presented in Table 5.1. However, no refractive index data could be found for HDPE. Thus, in this study, the HDPE refractive index was referred from [92]. For comparison, a Conrady fitting tool was used to calculate the refractive index (n) of HDPE for the wavelength region of 8-13 μm, as follows:

$$n = n_0 + \frac{a}{\lambda + \mathrm{b}} / (\lambda^{3.5}) \tag{5.2}$$

where n_0 =1.20048915, a = 4.52708247, b = -387.18421, and λ is the wavelength. These default dispersion data were obtained from Zemax software. The results of the calculated refractive index of HDPE for different wavelengths are illustrated in Figure 5.6. A good fit between the reference and calculated data were confirmed. The refractive index data was then entered into the Zemax software for lens design and analysis.

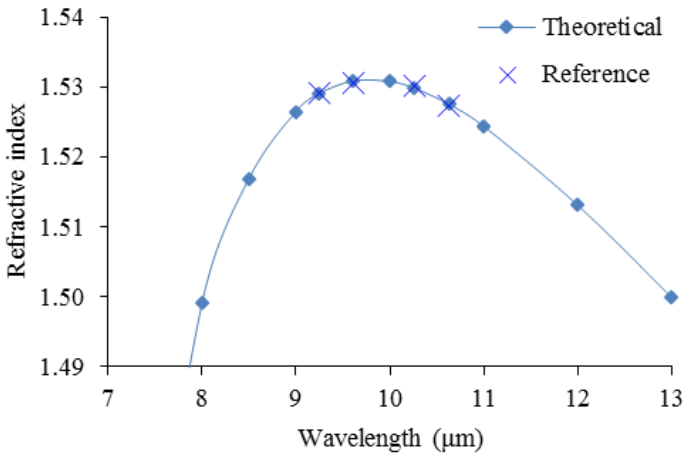

Figure 5.6: Refractive index of HDPE for different IR wavelengths.

Table 5.1: Refractive index of Si

Wavelength (μm)	Refractive index
8.5	3.418315
10	3.417762
12	3.417317

5.2.2 Evaluation of lens design

Double lenses consisting of the spherical (Lens 1) and an aspherical lens (Lens 2) were fabricated as discussed in Chapter 4. The lens performance was evaluated to ensure the usability of the designed lens for IR imaging. The lens system was designed with the maximum total angle of lens being set at 30°. These two lenses will be combined into one set of lens setup.

The thin lens maker's formula, Equation 5.1, was used to calculate the focal distance (*f*) of the lens. The refractive index of the lens material will vary for different wavelengths [41]. The wavelengths selected were between 8.5 to 12 μm of the IR region due to the accuracy of

the fitted data. Meanwhile, the focal length (f_T) of the combined lens can be calculated using the following equation, Equation 5.3:

$$f_T = \left(\frac{f_1 . f_2}{f_1 + f_2 - d}\right) \tag{5.3}$$

where f_1 is the focal length of Lens 1, f_2 is a focal length of Lens 2, and d is the distance between the two lenses. The combined focal length calculated by the Zemax software was 10.982 mm. The focal length of the lens will determine the angle of view of the lens. The lower the focal length, the wider the angle of view and the greater the area captured by the lens.

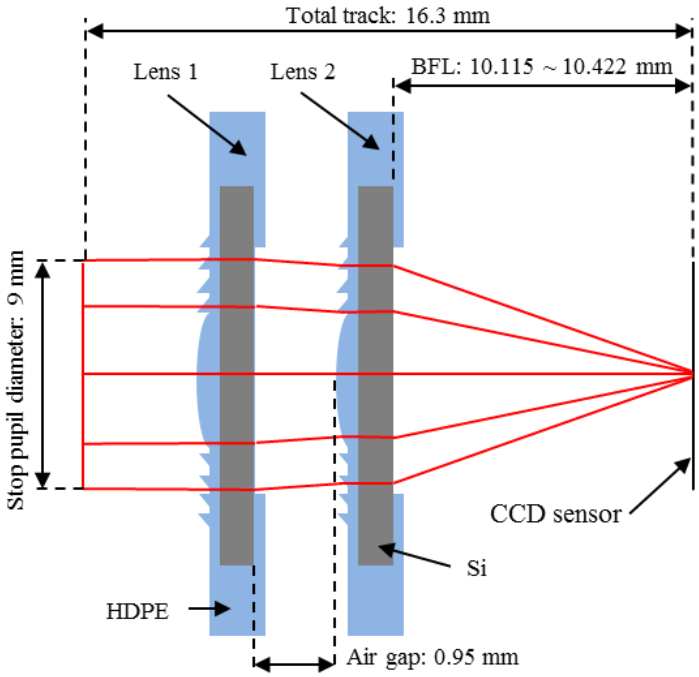

Figure 5.7: Schematic diagram of a double Si-HDPE hybrid Fresnel lens system.

After obtaining the lens parameters, these parameters were entered into Zemax software for design analysis and optimization. Figure 5.7 displays the lens structure design by the software. For lens optimization, the stop pupil diameter was set to 9 mm in the 13.5 mm diameter Fresnel region. The ratio of the lens focal length to the diameter of the stop pupil diameter (F-number) of the lens can be calculated using the following equation, Equation 5.4:

$$F = \frac{f}{D} \tag{5.4}$$

where f is the focal length, and D is the entrance/stop pupil diameter. The air gap between the two lenses was 0.95 mm, while the back focal length (BFL) calculated by the Zemax software was between 10.115 to 10.422 mm for the infinite and 400 mm object distance, respectively. The total track from the entrance pupil to the image surface of the design was 16.3 mm. The final design parameters of the lens systems are summarized in Table 5.2.

Table 5.2: Design results of lens unit.

Parameters	Value
Wavelength range (μm):	8.5-12
Principal wavelength (μm):	10
Effective focal length (mm):	10.98
Back focal length for ∞ (mm):	10.11
Entrance pupil diameter (mm):	9
F number:	1.29
Field of view (FOV) (degrees):	30
Total track (mm):	16.3

Figure 5.8 shows the ray trace of the lens design by Zemax software at the pupil diameter of 9 mm. The blue, green, red, and yellow lines indicate the incident angles of 0, 7.5, 10.5, and 15°, respectively. As the light incident angle increases from 7.5 to 15°, it is observed that the light was not distributed evenly at the focal point, which adversely effects image sharpness. From the analysis, it was found that the lens design had aberrations at the angles of 10.5 and 15° as compared to smaller angles. This can be observed more clearly in Figure 5.9, which shows rather bigger coma aberrations of the mentioned angles.

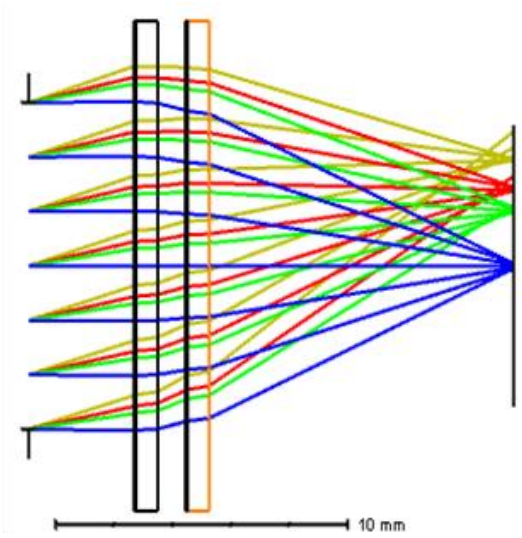

Figure 5.8: Ray trace of the lens systems.

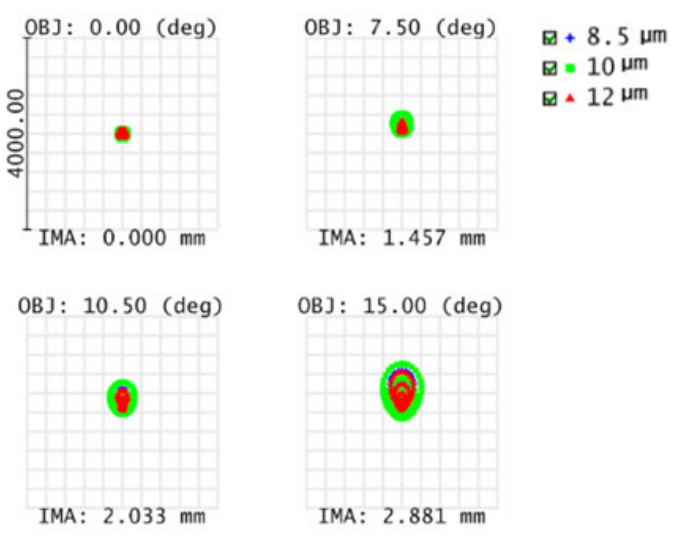

Figure 5.9: Spot diagram at lens focal point.

Figure 5.10 displays tangential (P_y) and sagittal (P_x) ray aberrations as functions of pupil coordination on different object angles and wavelengths. In the case of an ideal lens system, where the paraxial optical model is working, all lines at P_y and P_x are zero. Different wavelengths bend at different angles as the light passes through the lens medium. It can be seen from the graph, where the ray fan of 8.5, 10, and 12 µm wavelengths start to become off-axis at the incident angle of of 7.5° at the P_y axis. As the angle increases to 10.5° and 15°, the off-

axis of the ray aberration increased. Meanwhile, at the P_x axis, an off-axis of the ray aberration is only apparent at 15°.

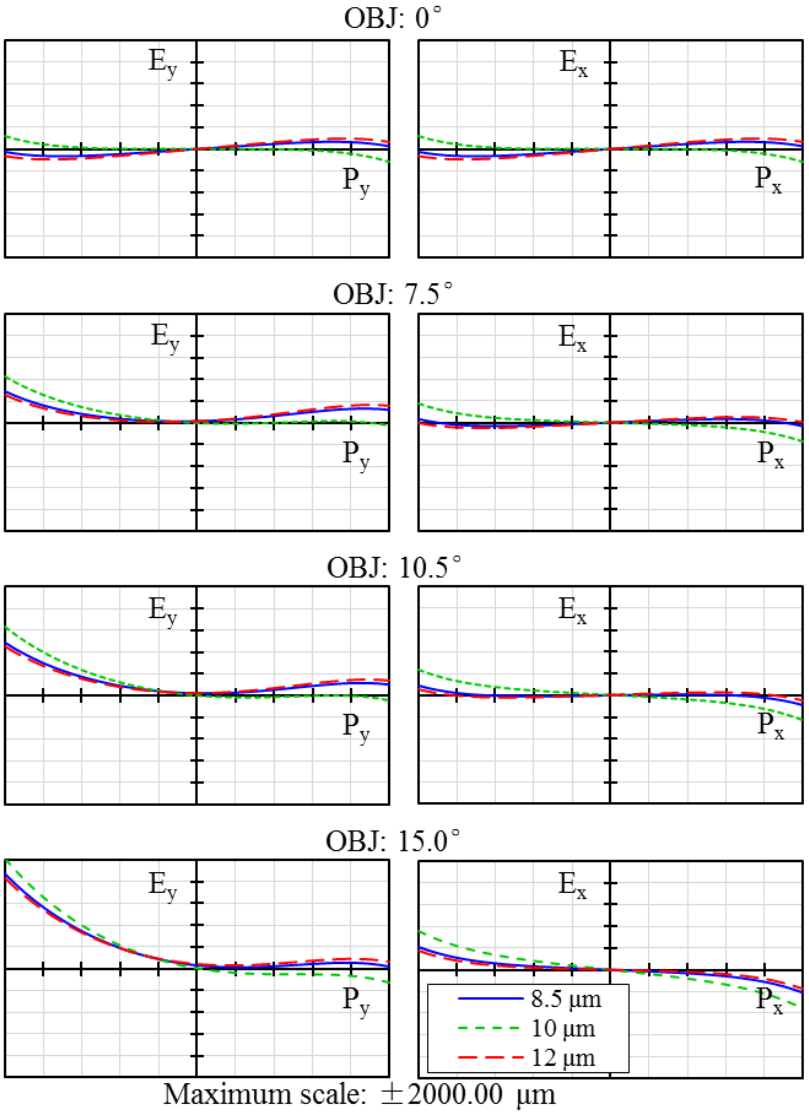

Figure 5.10: Zemax lens transverse ray fan plot for different wavelength and incident angles.

An image of 288×384 pixels in Figure 5.11(a) was used to analyse the lens design. From the analysed image in Figure 5.11(b), the image has some distortion. However, considering other factors, such as the limited HDPE thickness, the image quality can be somewhat compromised.

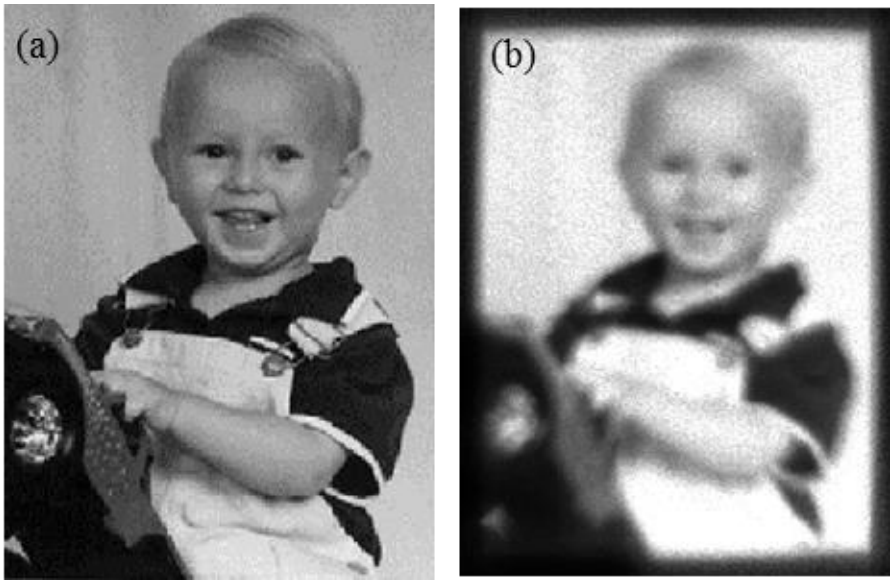

Figure 5.11: (a) An original image from Zemax software and (b) simulated image obtained by the double Si-HDPE hybrid lens.

5.2.3 Imaging setup and evaluation

5.2.3.1. Imaging setup

Meanwhile, an imaging test was performed in night mode using the Therm-App (Opgal Optronic Industries Ltd.) IR thermal camera. The camera has a 384 × 288 pixels image sensor with 17 μm pixels pitch. The camera IR spectrum is for long wave IR regions (7-14 μm). An Android smartphone was connected to operate the camera. Both formed Fresnel lenses were attached to an aluminum camera housing, which was designed and fabricated with an adjustable mechanism to obtain the required back focal length of the lens during imaging. The camera setup for night mode imaging experiment is shown in Figure 5.12, and a human body was selected as the test object. The object was placed at different distances from the camera (400 mm and 2 m) and the image was captured and compared to analyse the performance of the lens. Figure 5.13 displays the actual setup of the camera for night imaging performance evaluation.

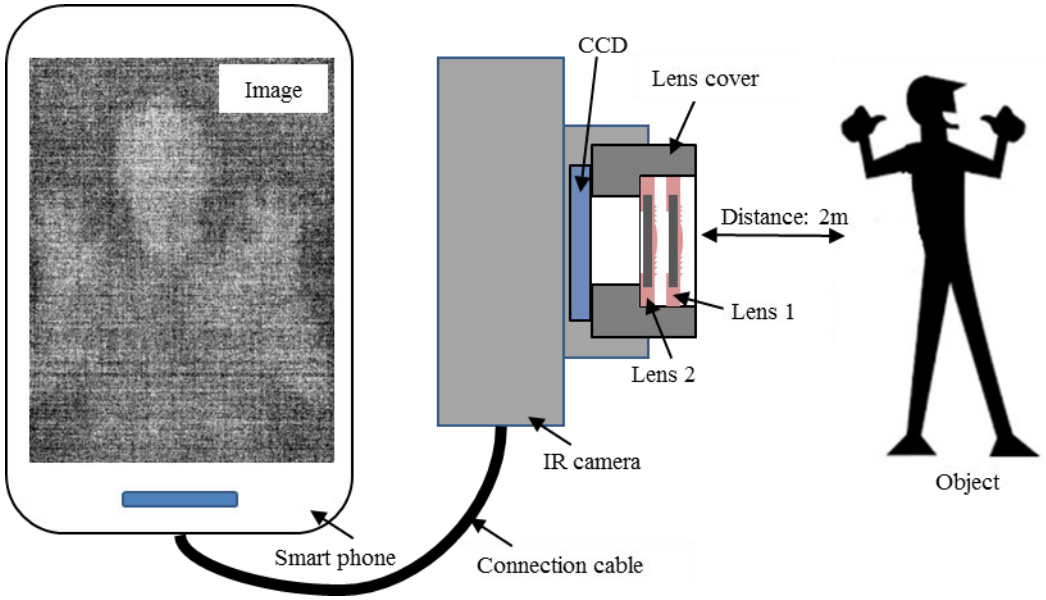

Figure 5.12: Schematic diagram of IR imaging systems camera setup.

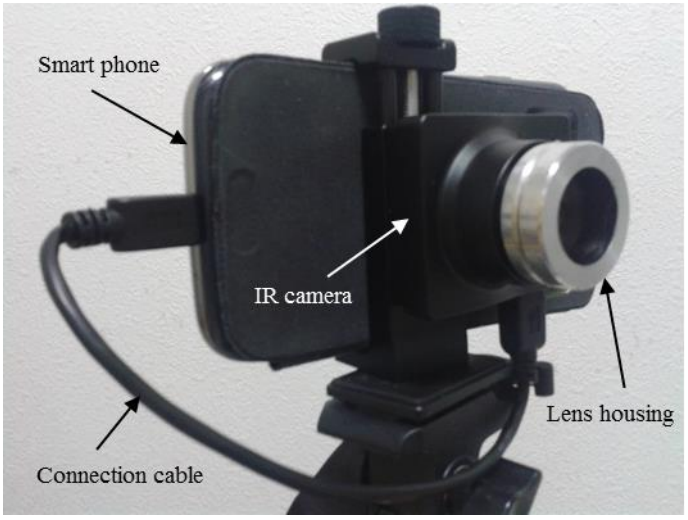

Figure 5.13: Camera setup for night imaging performance evaluation.

5.2.3.2. Lens performance evaluation

The image quality depends on the wavelength distribution, the F-number of the operating systems, and the focal position. It also depends on the field angle of the object. To evaluate the performance of the lens, the modulation transfer function (MTF) was used. It is the effective measurement to characterize the contrast of the lens systems [93].

In calculating the MTF, the optical transfer function (OPT) needs to be considered, which is proportionate to the exit pupil diameter. An autocorrelation as a transfer function is identified by the variable changes, which can be calculated by the following equations:

$$\xi = \frac{x}{\lambda\, d_i} \tag{5.5}$$

where x is the pupil shift distance of the autocorrelation, λ is the wavelength, and d_i is the distance from the image from the pupil exit. For the full-width exit pupil (D) system, an image cut off frequency needs to be considered with the following equations:

$$\xi_{cutoff} = \frac{1}{\lambda\, FN} \tag{5.6}$$

$$FN = \frac{f}{D} \tag{5.7}$$

$$FN = \frac{d_i}{D} \tag{5.8}$$

where FN is the focal ratio, which can be calculated by using Equation 5.7 for the infinity distance of the object, and Equation 5.8 for the finite conjugate operating systems.

The diffraction limited MTF represents the real OTF, which explain the best performance of the lens systems. It will indicates the contrast of the lens system when the line spread function is measured. As the exit pupil of the systems is of a circular shape, the following equations are used:

$$MTF\left(\frac{\xi}{\xi_{cutoff}}\right) = \frac{2}{\pi}\left\{cos^{-1}\left(\frac{\xi}{\xi_{cutoff}}\right) - \frac{\xi}{\xi_{cutoff}}\left[1 - \left(\frac{\xi}{\xi_{cutoff}}\right)^2\right]^{\frac{1}{2}}\right\} if\ \xi \le \xi_{cutoff}$$

$$= 0\ if\ \xi > \xi_{cutoff} \tag{5.9}$$

Figure 5.14 presents the diffractive limit of the lens systems. Results show that the design lens system's diffractive limit is above the curves of tangential and sagittal, which results in the dark image quality. This is also means that the designed lens will face difficulties

in capturing image details at the far distance. However, this diffractive limit is neglected in this research due to the limited thickness of the HDPE layer. However, the lens performance can be improved with the combination of multiple lenses or adding more lens surfaces. During the measurement, the magnitude response of the imaging system to sinusoids of different spatial frequencies was measured, and described in terms of contrast [94]. Contrast can be calculated by using the following equations:

$$\%Constrast = \left[\frac{l_{max} - l_{min}}{l_{max} + l_{min}}\right] \tag{5.10}$$

where l_{max} is the maximum intensity and l_{min} is the minimum intensity. The contrast also can be represented by the square wave as showed in Figure 5.15.

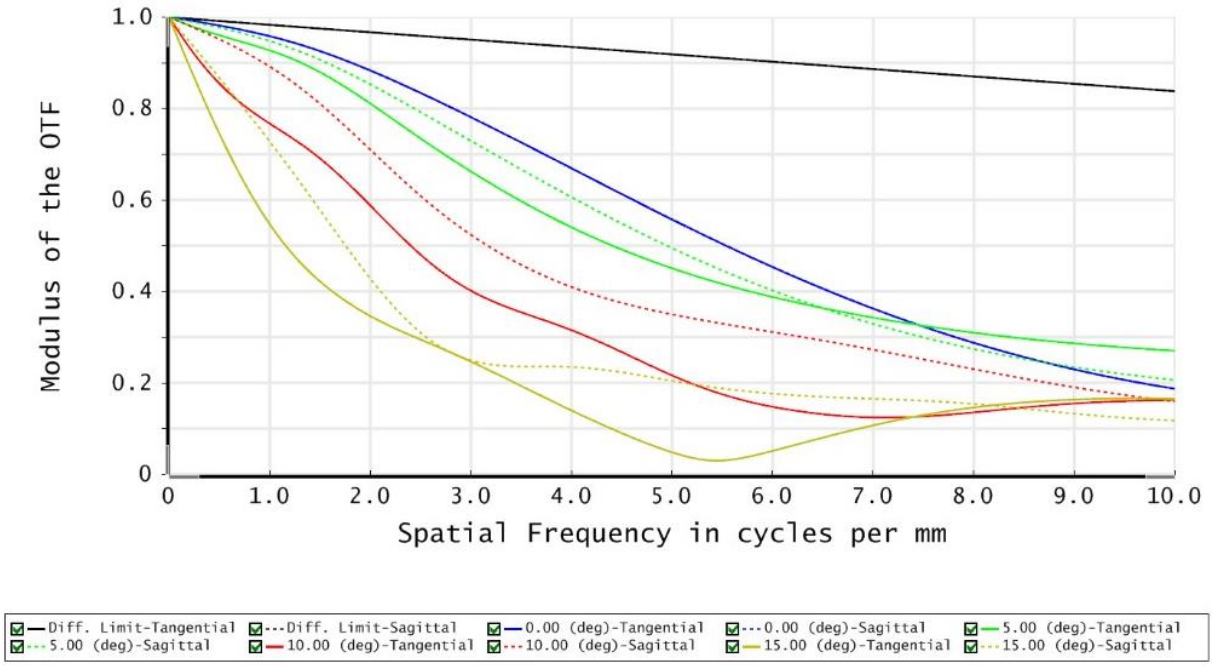

Figure 5.14: Diffractive limit of the double Si-HDPE hybrid Fresnel lens system.

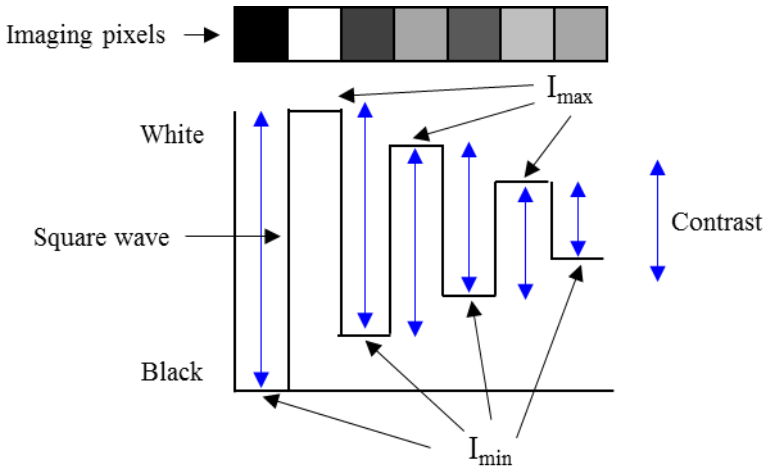

Figure 5.15: Square wave representative of the contrast.

The modulation transfer function (MTF) and effective focal length (EFL) measurements were performed using ImageMaster HR test station (Trioptics Japan Co., Ltd., Japan) at different field angles, as showed in Figure 5.16 (a). The MTF measurement accuracy and repeatability (on-axis and off-axis) of the equipment was ± 0.03 MTF and ± 0.02 MTF, respectively. The details of the measurement parameters are listed in Table 5.3. During the measurement, to obtain the image height, the cross-sectioned of the lens was adjusted in either a negative or positive direction, as per Figure 5.16 (b). The result obtained was then compared with the simulated MTF data of Zemax optical design software.

Table 5.3: MTF measurement parameters.

Measurement conditions	Value
Spatial frequency and pitch (lp/mm)	1~10/1
Angle of view (max. image height) /division pitch	15°/5°
Collimator (mm)	50
AF frequency (lp/mm)	5
Total angle of view	30°
Object distance (m)	Infinite
Light source orientation	Sagittal / Tangential
Center wavelength (µm)	10
Wavelength range (µm)	8.2-12.8

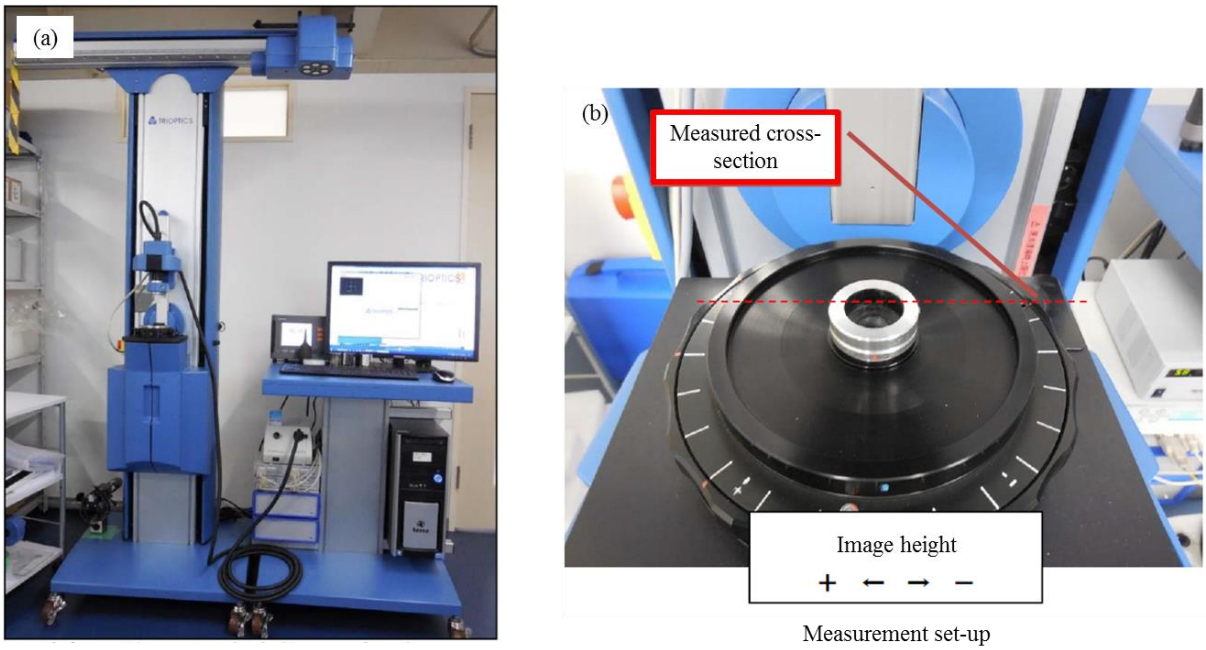

Image Master HR

Measurement set-up

Figure 5.16: Photograph of: (a) ImageMaster MTF equipment and (b) cross section measurement for different image height.

In order to obtain the sagittal and tangential MTF, different orientations of light incident angles was measured as showed in Figure 5.17 (a). The orientation of the angle starts from 0°

to 135°. Meanwhile, to obtain the focal length of the lens system, the lens was moved along the Z axis, in a positive or negative direction, as showed in Figure 5.17(b).

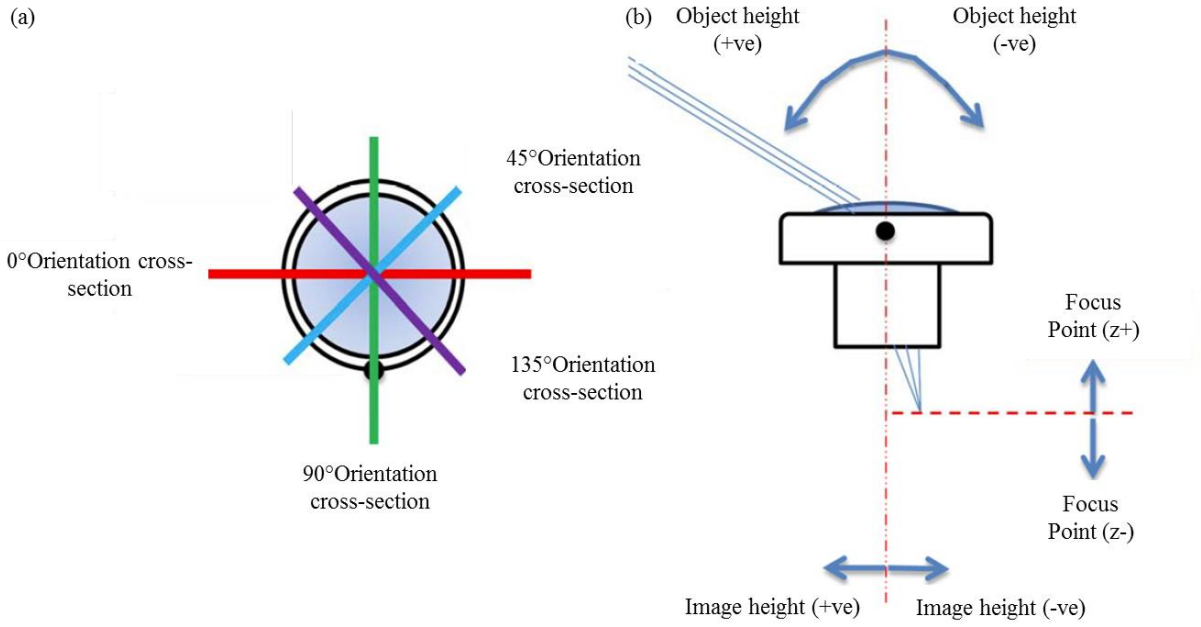

Figure 5.17: MTF measurement conditions.

MTF demonstrates the modulation (contrast) response capabilities of a lens system for each spatial frequency and different tangential/sagittal angles. In this study, the MTF was measured at a wavelength of 10 μm and the field angle varied from 0 to 15°, with an angle pitch of 5°. The experimental MTF data was compared with the theoretical geometric MTF obtained by Zemax and is illustrated in Fig. 5.18.

In the figure, there is good agreement between the experimental data and the theoretical MTF. The experimental curve stands below the simulated MTF at the field angle of 0° as shown in Figure 5.18(a), resulting in lower image contrast. The differences in the measured and the simulated MTF is due to errors caused by poor line image density or line spread function (LSF) during MTF measurement. In some cases, LSF is barely obtained because of the darkness of the image. Thus autofocusing was used to obtain reliable measurement data.

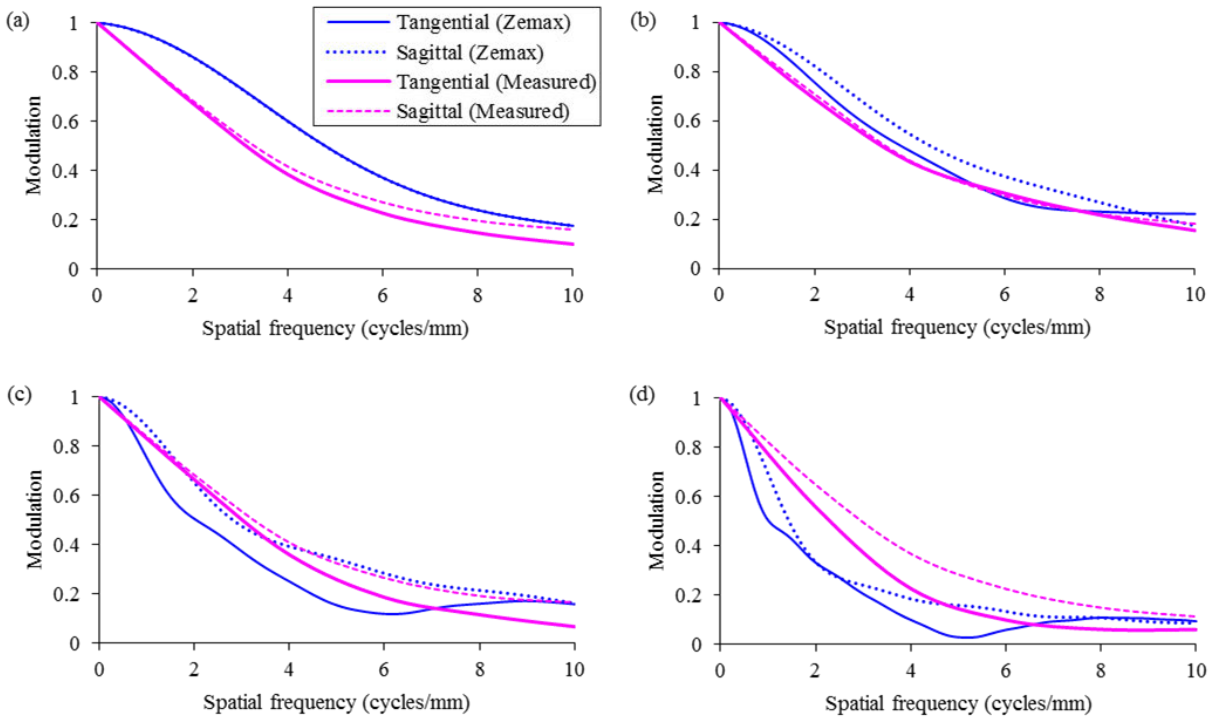

Figure 5.18: Comparison of geometric MTF calculated by Zemax and measured results for different field angles: (a) θ = 0°, (b) θ = 5°, (c) θ = 10°, and (d) θ = 15°.

As the field angle increased to 5° and 10° as shown in Figures 5.18(b) and (c) respectively, the frequency dependence of tangential and sagittal from the measured and simulated data are almost the same. However, a higher contrast was noticed at the measured tangential frequency of 10° field angle, at a lower frequency. The measured MTF continued to show better performance at a lower frequency as illustrated in Figure 5.18(d) as the field angle increased to 15°, and continued on the same pattern with the simulated MTF, as the frequency increased. The slight differences between the simulated and the measured MTF curve were also due to the differences in the light passing through the diffractive surfaces of the lenses. In the overall performance for all field angles, the MTF curve stands 0.1 above the modulation. Therefore, the fabricated lens results in relatively low contrast images.

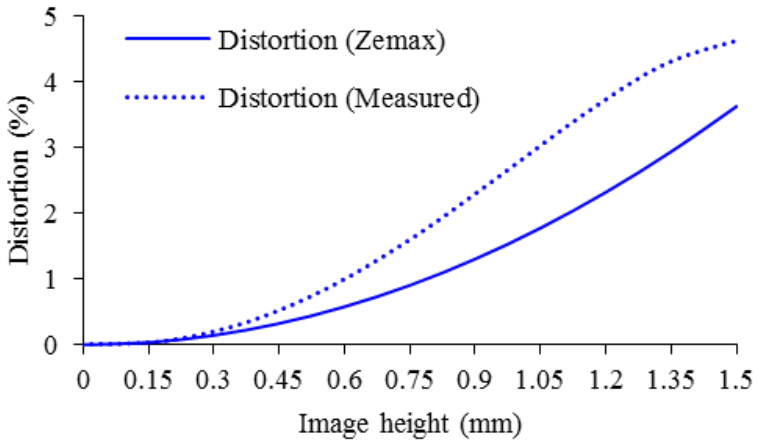

Figure 5.19: Zemax-simulated and measured image distortion.

Meanwhile, as shown in Figure 5.19, the measured distortion percentage shows a similar pattern as the results simulated by Zemax with an approximately 1% difference. To calculate the distortion percentage of the image produced by the lens systems, the following equation (Eq. 5.11) was used, where *AD* is the actual distance, and *PD* is the predicted distance.

$$Distortion\ (\%) = \frac{AD-PD}{PD} \times 100 \tag{5.11}$$

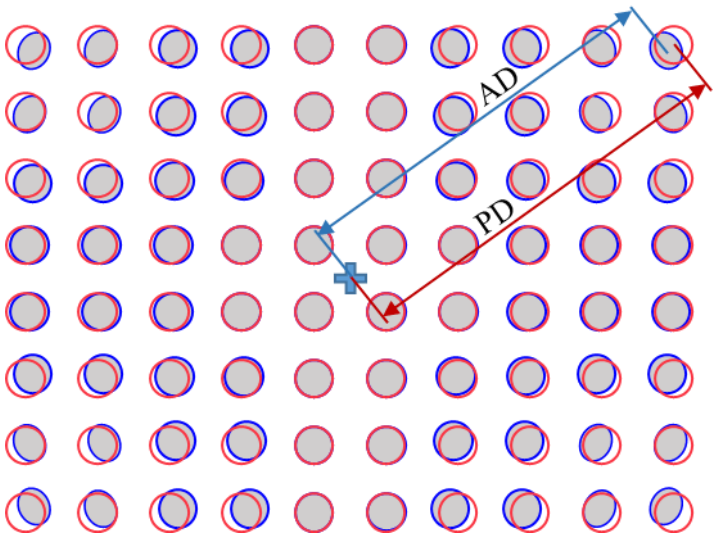

Figure 5.20: Schematic diagram of image distortion.

A series of EFL measurements at the wavelength of 10 μm was also done and illustrated in Figure 5.21, where the average measured focal length was 9.6 mm. Although there is a

difference in the measured results, all of the measured focal lengths are in the tolerance of ± 1.5 mm with respect to the designed focal length (10.982 mm).

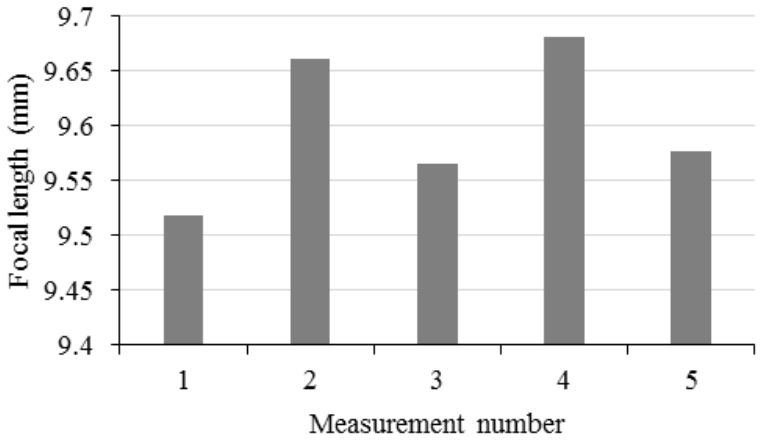

Figure 5.21: Focal length measurement results at a wavelength of 10 μm.

5.2.4 Night mode imaging

The press molded lenses were assembled with the lens housing and attached to the IR camera for night mode imaging. The white-hot imaging mode was selected for the camera setting. Night vision images captured by a double Si-HDPE hybrid Fresnel lens are shown in Figure 5.22. These images were captured at the distances of 400 mm and 2 m. For comparison, visible light images were also listed in the same figure. After pixel correction, at a shorter imaging distance (400 mm), acceptable image quality was obtained where details of the object could be seen. At longer distances (2 m), the object shape is still identifiable even though it lost some image sharpness due to chromatic aberrations of the lens systems. As viewed from the MTF measurement result, the contrast of the image is low, resulting in a dark image. Another possible reason for the low image sharpness is due to the fact that the Si-HDPE hybrid substrate has low transmittance in ~9 μm of IR region.

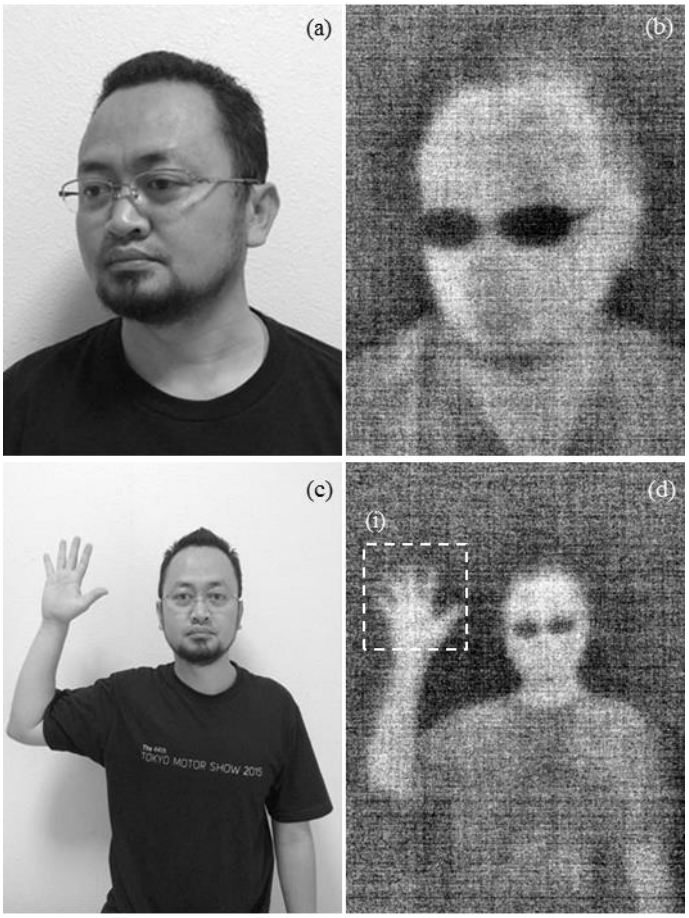

Figure 5.22: Visible light and night vision images at different distances; (a)-(b) 400 mm and (c)-(d) 2 m, and rectangle (i) showing image aberration.

Meanwhile, image distortion is not identifiable from the captured image due to the low contrast of the images; even though the measured distortion showed slightly higher values than the Zemax estimation, as discussed earlier in Section 5.22. Chromatic aberration was also detected in the IR image, as shown in Figure 5.22(d) in rectangle (i), which resulted in blurred images due to stray light from the lens system. The stray light might have been caused by the light scattering at the edges and wall of the Fresnel structure, as well as light reflection from the Si substrate [91,95]. Figure 5.23 shows the stray light generation in the lens system. Meanwhile, the difference between lens design wavelengths (8.5-12 μm) and image sensor sensitivity wavelengths (7-14 μm) also degraded the image quality and resulted in the blurred image. Another reason for the blurred image was the IR transmittance of the Si-HDPE hybrid

substrate in the significantly low ~9.5 μm region, as presented previously in Chapter 3 (see Fig. 3.24).

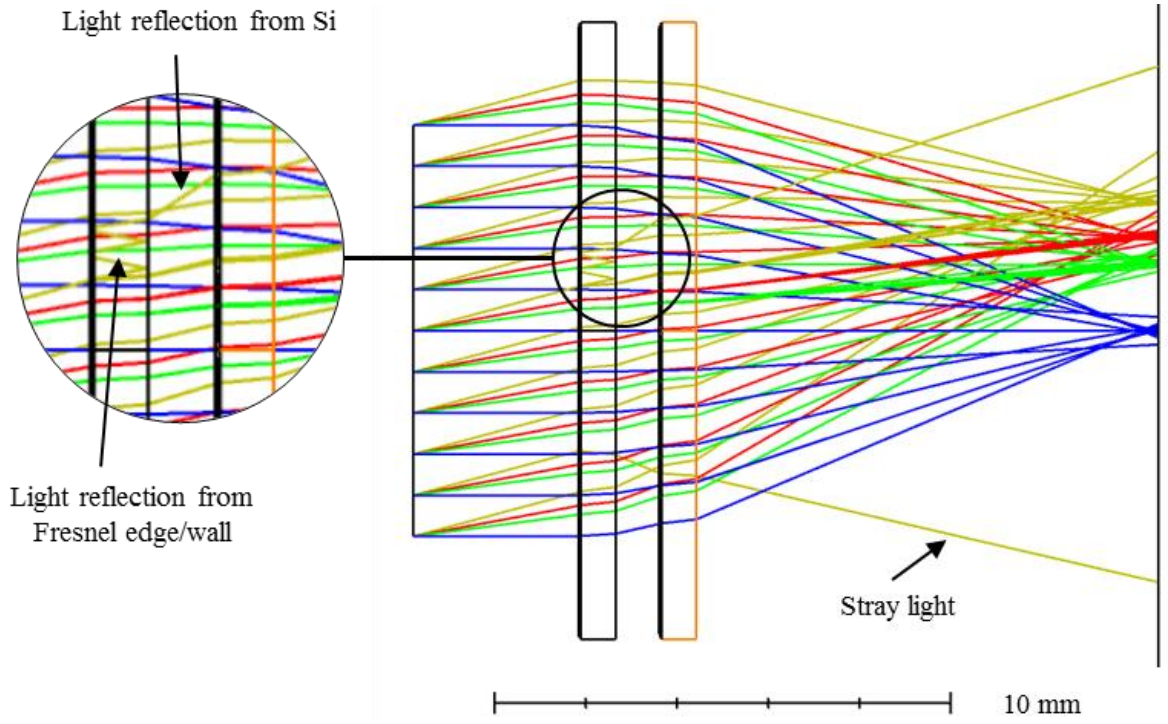

Figure 5.23: Schematic diagram of stray light formation from the lens system.

5.2.5 Thermography imaging

A thermography imaging trial has also been done using a double Si-HDPE hybrid Fresnel lens as shown in Figure 5.24. The captured image validated the lens systems as being usable in thermography application. There is no significant difference in the image quality between the standard Ge lens systems (Therm-App 19 mm lens) and Si-HDPE hybrid Fresnel. The temperature distribution of the object can be recognized and measured, although the temperature value and accuracy needs to be calibrated to realize the use of hybrid lenses for thermography applications.

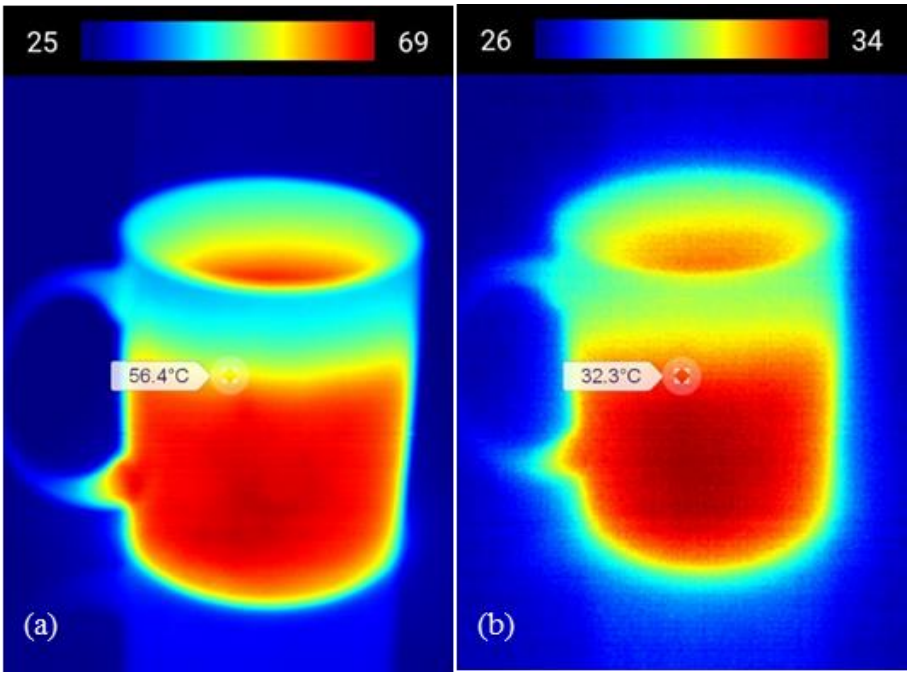

Figure 5.24: Thermography images of different lens systems: (a) standard germanium lens and (b) uncalibrated double Si-HDPE hybrid Fresnel.

5.2.6 Combination of Si-HDPE with Ge lens

To demonstrate the ability of the developed Si-HDPE hybrid lens to work with other IR lens materials,, imaging trials were conducted by combining a spherical hybrid Fresnel lens (Lens 1) and a Ge convex-concave lens. The lens systems schematic diagram is illustrated in Figure 5.25(a). The captured images using this lens combination are shown in Figures 5.25(b) and (c). The chromatic aberration is minimized as shown in Figure 5.25(c) in rectangle (i), which might be due to reduced stray light, and the better IR transmittance of Ge. Clearer and sharper images are obtained compared with the double Si-HDPE hybrid lenses, which can be seen from Figure 5.26. From the figure, a higher grey value is recorded when a combination of hybrid Fresnel and Ge convex-concave lens was used, in contrast to the double hybrid Fresnel. This highlights the use of the developed hybrid lens in combination with other IR lens material is possible, which has the potential to greatly improve the imaging quality of the developed lens system, for higher-precision applications.

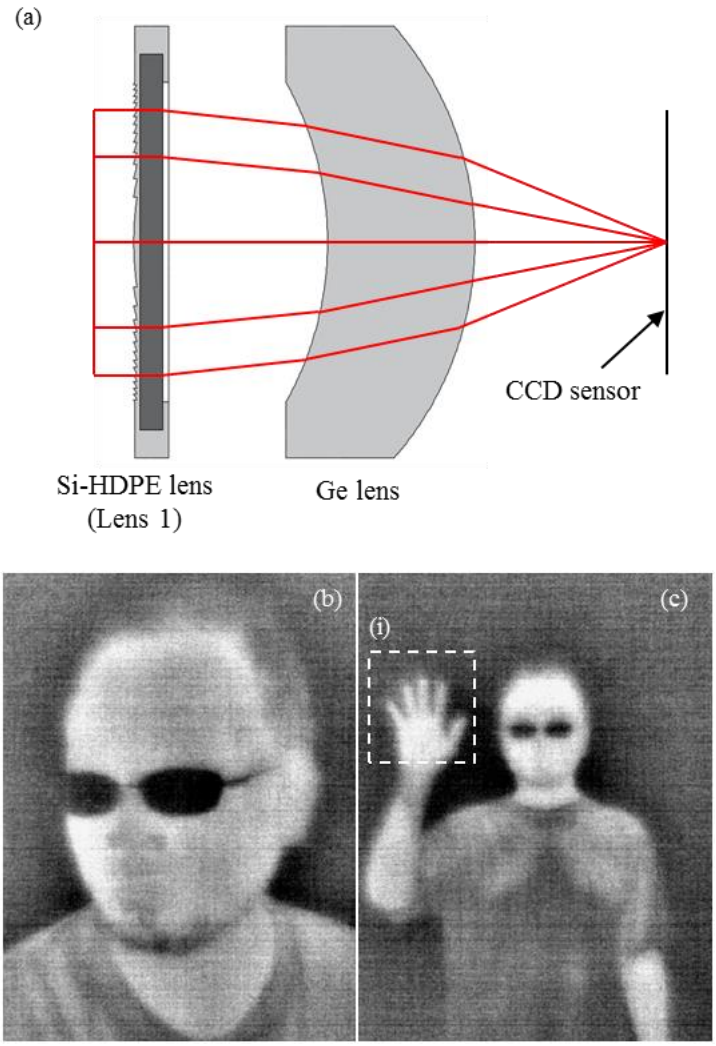

Figure 5.25: (a) Schematic diagram of combining a Si-HDPE hybrid lens and germanium lens, (b) night vision images captured by combining a Si-HDPE hybrid lens and a germanium lens at different distances; (b) 400 mm and (c) 2 m, and rectangle (i) showing image aberration.

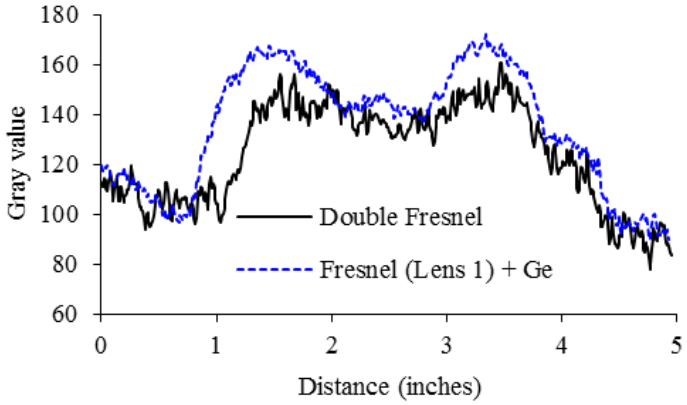

Figure 5.26: Image sharpness evaluation between double Si-HDPE hybrid Fresnel and a combination of a spherical Si-HDPE hybrid Fresnel (Lens 1) + Ge.

5.2.7 Si-HDPE and HDPE Fresnel lens comparison.

A comparison also has been made to differentiate the performance of the Si-HPDE lens with the HDPE lens. As a comparison, Lens 1 of Si-HDPE hybrid lens was compared with the Fresnel lens made by only HDPE. The HDPE Fresnel lens thickness was 250 μm to ensure the IR transmittance at its best (Figure 5.27). An object was captured at the distance of 400 mm, and the images are presented in Figure 5.28.

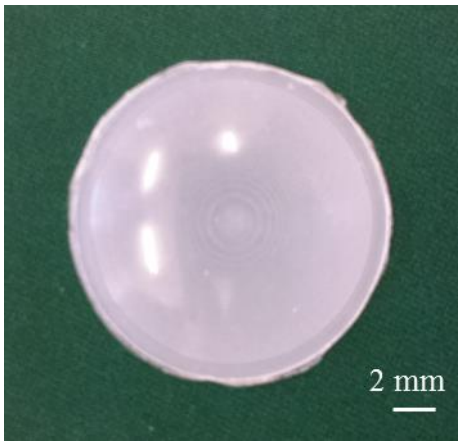

Figure 5.27: A 250 μm Fresnel lens made by HDPE

From the figure, it displays that the object that captured using the Si-HDPE hybrid Fresnel lens was able to capture more clear images compared to those image that captured by the HDPE lens alone. The results demonstrate that the HDPE lens is unsuitable to be used as the IR lens due to its IR absorbance, even though it is formed at 250 μm. To control the IR absorbance, the thickness of the HDPE needs to be reduced. However, the stiffness of the extremely thin HDPE Fresnel lens will become very low, and unsuitable to be used as the lens.

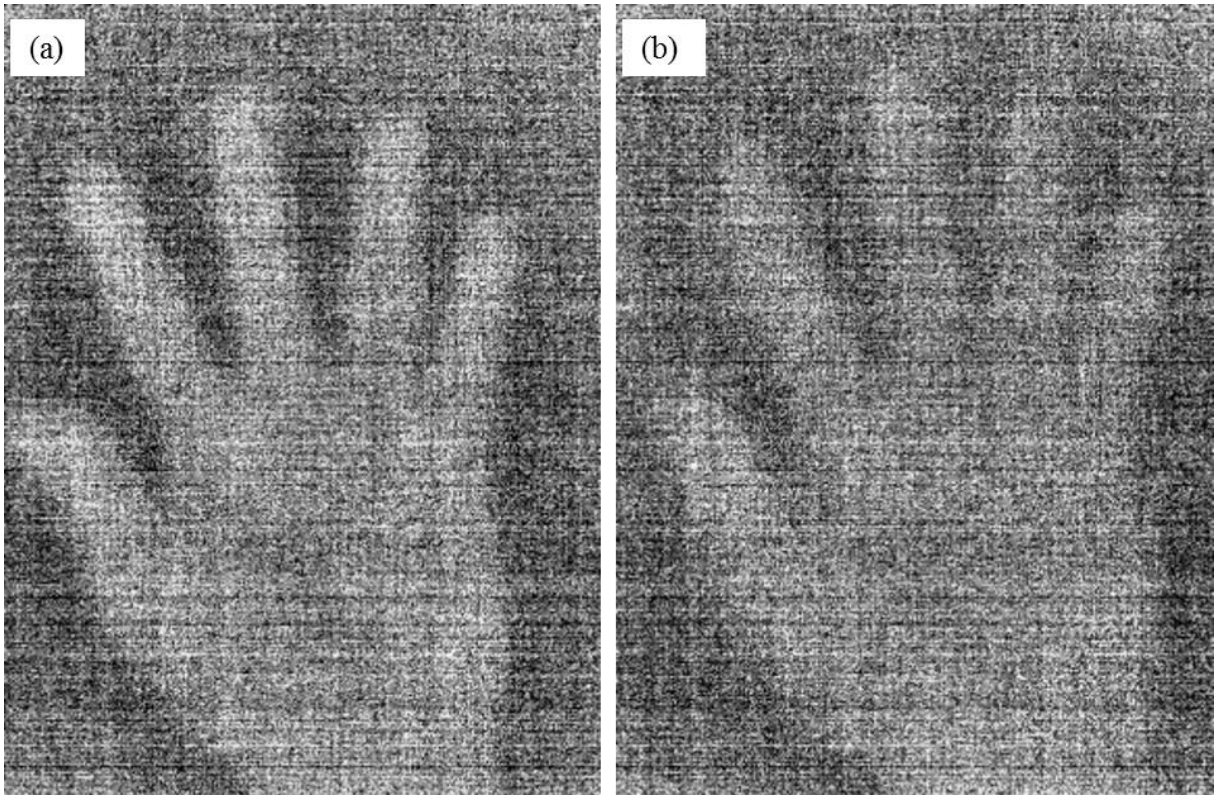

Figure 5.28: Image comparison of the object captured by using (a) Si-HDPE hybrid Fresnel, and (b) HDPE Fresnel lens.

5.3 Chapter summary

A Si-HDPE hybrid Fresnel lens system for infrared imaging applications has been designed and fabricated. The form accuracy and optical capabilities of the fabricated lenses were evaluated. The following conclusions were obtained:

1. The measured modulation transfer function of the fabricated lens system showed similar results to the simulated data by the Zemax optical design software.
2. The fabricated hybrid lens system produced satisfactory image quality in night mode, with a slightly lower image contrast than that of Ge lenses.
3. The ability of the lens systems in thermography imaging was also demonstrated. The temperature distribution was properly detected by the developed lenses.

4. A combination of a Si-HDPE hybrid lens and a concave-convex Ge lens produced a higher quality image than the double Si-HDPE hybrid lens system. This offers the possibility of using the fabricated hybrid lens in combination with other IR material lenses for high-precision infrared systems.

This study demonstrates the possibility of a cost-effective method for fabricating compact and high-performance IR optical components for night vision systems. These lenses might have the potential for applications in future infrared optical technologies for rescue, night surveillance, night driving assistance, as well as thermography.

CHAPTER 6

Conclusion

6.1 Conclusion

The work presented in this thesis addresses a step by step procedure in fabricating the Si-HDPE hybrid lens. The work is mainly categorized into three parts which are, the evaluation of Si-HDPE hybrid substrate for IR applications, the lens forming on the hybrid substrate, and the Si-HDPE hybrid lens design. Based on the results presented within this thesis, the main conclusions and achievements are detailed below.

The Si-HDPE hybrid substrate has been successfully fabricated using the press molding method. The Si-HDPE adhesion was achieved with the help of silane crosslinking HDPE resin. The hybrid substrate is capable of improving the IR transmittance of Si in the IR region of ~7.4-8.8 μm and ~9.3-12 μm, when extremely thin HDPE was used to laminate one side of the Si. The hybrid substrate also demonstrated the capability for IR imaging during the optical evaluations.

The micro structures also successfully formed on the HDPE layer of the hybrid substrate, where it demonstrates the capability of designing the lens using the hybrid substrate. The form accuracies are achieved when shrinkage compensation is included. The press molding in a vacuum environment is essential to improve the form accuracies, and also eliminate the formation of trenches on the lens and coating surfaces.

The lens design was also manipulated using the hybrid substrate. A flat and thin Fresnel were designed on the hybrid substrate, whereas the design uses a combination of double Si-HDPE hybrid Fresnel lenses. The lenses were accurately press molded using a two-step pressing method. During the optical evaluation, the double Si-HDPE hybrid Fresnel lens also displays its capabilities to capture the image during night mode imaging. The hybrid lenses also show capabilities used for thermography. The temperature distributions were visualized clearly during the imaging.

In order to improve the IR imaging, the Si-HDPE hybrid Fresnel also displays its capabilities to work with other IR lens materials. A combination with Ge produced a dramatically improved image.

Overall, the Si-HDPE hybrid lens demonstrates its usability to be for IR imaging and thermography. With the use of the hybrid lens, it is possible to reduce the cost of manufacturing the IR lenses as well as the IR material. It also provides an alternative solution for cheaper and lighter weighing (compact) IR imaging system.

6.2 Future works

Several recommendations are proposed for the future work of the Si-HDPE hybrid optics. The recommendations are as follows:

1. Evaluation of refractive index drop of Si-HDPE after the press molding process. This is important for enhancing the image quality obtained with the hybrid lenses. The HDPE material is subjected to the residual stress during the press molding. The relationship between the residual stress and the refractive index changes need to be further studies with different parameters.

2. In the present work of the Si-HDPE hybrid micro lens array, a numerical simulation was used to investigate the polymer flow during press molding. A numerical simulation of air trapping work should be investigated in to explain the air trapping phenomenon.
3. For future works, other types of polymers need to be used to improve the IR transmittance of the hybrid lens. This is important to improve the image quality of the lens design.
4. New Si-HDPE hybrid lens designs should be pursued to obtaining better image quality during night imaging. Thinner Si should be included to achieve higher IR transmittance.
5. The application of the Si-HDPE hybrid lens in thermography imaging holds great promise for the future. Proper lens calibration is required to accurately measure the temperature distributions.
6. For further IR camera systems cost reduction, a cheaper solution of IR camera need to be considered.

REFERENCES

1. A. Rogalski, "Recent progress in infrared detector technologies," Infrared Phys. Technol. **54**, 136–154 (2011).

2. N. A. Kulakova, A. R. Nasyrov, and I. M. Nesmelova, "Current trends in creating optical systems for the IR region," J. Opt. Technol. **77**, 324–330 (2010).

3. J. Yan, M. Yoshino, T. Kuriagawa, T. Shirakashi, K. Syoji, and R. Komanduri, "On the ductile machining of silicon for micro electro-mechanical systems (MEMS), opto-electronic and optical applications," Mater. Sci. Eng. A **297**, 230–234 (2001).

4. J. Yan, K. Maekawa, J. Tamaki, and T. Kuriyagawa, "Micro grooving on single-crystal germanium for infrared Fresnel lenses," J. Micromechanics Microengineering **15**, 1925–1931 (2005).

5. J. Yan, K. Syoji, and J. Tamaki, "Some observations on the wear of diamond tools in ultra-precision cutting of single-crystal silicon," Wear **255**, 1380–1387 (2003).

6. M. Mukaida and J. Yan, "Ductile machining of single-crystal silicon for microlens arrays by ultraprecision diamond turning using a slow tool servo," Int. J. Mach. Tools Manuf. 0–1 (2016).

7. R. N. Claytor, N. E. Claytor, W. M. Drive, and F. Worth, "Low-Cost Polymer Infrared Imaging Lens," **5074**, 855–866 (2003).

8. V. Doushkina, "Innovative Hybrid Optics: Combining the thermal stability of glass with low manufacturing cost of polymers," Polym. Opt. Des. Fabr. Mater. SPIE **7788**,

778809-778809–12 (2010).

9. N. Sultanova, S. Kasarova, and I. Nikolov, "Characteristics of Optical Polymers in the Design of Polymer and Hybrid Optical," J. Phys. **40**, 258–264 (2013).

10. L. Li and A. Y. Yi, "An affordable injection-molded precision hybrid glass–polymer achromatic lens," Int. J. Adv. Manuf. Technol. **69**, 1461–1467 (2013).

11. V. C. Venkatesh, "Precision manufacture of spherical and aspheric surfaces on plastics, glass, silicon and germanium," Curr. Sci. **84**, 1211–1219 (2003).

12. V. C. Venkatesh, S. Izman, S. Sharif, T. T. Mon, and M. Konneh, "Precision micro-machining of silicon and glass," Proc. IEEE Int. Conf. Ind. Technol. **2**, 1146–1151 (2002).

13. J. Yan, T. Oowada, T. Zhou, and T. Kuriyagawa, "Precision machining of microstructures on electroless-plated NiP surface for molding glass components," J. Mater. Process. Technol. **209**, 4802–4808 (2009).

14. T. Zhou, J. Yan, J. Masuda, T. Oowada, and T. Kuriyagawa, "Investigation on shape transferability in ultraprecision glass molding press for microgrooves," Precis. Eng. **35**, 214–220 (2011).

15. T. F. Zhou, J. W. Yan, J. Masuda, and K. Tsunemoto, "Ultraprecision Mass Fabrication of Aspherical Fresnel Lens by Glass Molding Press," Adv. Abras. Technol. Xiv **325**, 713–718 (2011).

16. A. Yang, M. Zhang, L. Li, Y. Wang, B. Zhang, Z. Yang, and D. Tang, "Ga-Sb-S Chalcogenide Glasses for Mid-Infrared Applications," J. Am. Ceram. Soc. **99**, 12–15 (2016).

17. J. Deegan, K. F. Walsh, G. Lindberg, R. Benson, D. Gibson, S. Bayya, J. Sanghera, and

E. Stover, "Index change of chalcogenide materials from precision glass molding processes," Proc. SPIE **9451**, 94511R (2015).

18. J. D. Owen, M. A. Davies, D. Schmidt, and E. H. Urruti, "On the ultra-precision diamond machining of chalcogenide glass," CIRP Ann. - Manuf. Technol. **64**, 113–116 (2015).

19. M. Arif, M. Rahman, and W. Y. San, "A state-of-the-art review of ductile cutting of silicon wafers for semiconductor and microelectronics industries," Int. J. Adv. Manuf. Technol. **63**, 481–504 (2012).

20. T. L. Williams, Thermal Imaging Camera: Characteristics and Performance (CRC Press, 2009).

21. J. M. Lloyd, Thermal Imaging Systems (Springer US, 1975).

22. A. B. Djuris, "UV-VIS and Photoluminescence Spectroscopy for Nanomaterials Characterization," 387–403 (2013).

23. T. Kamizuka, T. Miyata, S. Sako, H. Imada, T. Nakamura, K. Asano, M. Uchiyama, K. Okada, T. Wada, T. Nakagawa, T. Onaka, and I. Sakon, "Development of high-throughput silicon lens and grism with moth-eye antireflection structure for mid-infrared astronomy," **8450**, 845051 (2012).

24. T. Grulois, G. Druart, N. Guérineau, A. Crastes, H. Sauer, and P. Chavel, "Extra-thin infrared camera for low-cost surveillance applications.," Opt. Lett. **39**, 3169–72 (2014).

25. A. Zakery and S. . Elliott, An Introduction to Chalcogenide Glasses (Springer-Verlag Berlin Heidelberg, 2007).

26. K. J. Ma, H. H. Chien, S. W. Huang, W. Y. Fu, and C. L. Chao, "Contactless molding of arrayed chalcogenide glass lenses," J. Non. Cryst. Solids **357**, 2484–2488 (2011).

27. J. H. Choi, D. H. Cha, H. Y. Kang, J.-H. Kim, and H.-J. Kim, "Development of chalcogenide glass with thermal stability for molded infrared lens," SPIE Photonics West 2014-OPTO Optoelectron. Devices Mater. **8982**, 89821U (2014).

28. H. Li, P. He, J. Yu, L. J. Lee, and A. Y. Yi, "Localized rapid heating process for precision chalcogenide glass molding," Opt. Lasers Eng. **73**, 62–68 (2015).

29. J. D. Lytle, Polymeric Optics, 2nd Edition (McGraw-Hill Professional, 1994).

30. S. N. Kasarova, N. G. Sultanova, C. D. Ivanov, and I. D. Nikolov, "Analysis of the dispersion of optical plastic materials," Opt. Mater. (Amst). **29**, 1481–1490 (2007).

31. S. Namnabat, R. Norwood, E. Dereniak, J. Griebel, and J. Pyun, "Sulfur copolymers for IR optics," SPIE Newsroom 10–12 (2014).

32. E. V Loewenstein, D. R. Smith, and R. L. Morgan, "Optical constants of far infrared materials. 2: crystalline solids.," Appl. Opt. **12**, 398–406 (1973).

33. P. T. Tsilingiris, "Comparative evaluation of the infrared transmission of polymer films," Energy Convers. Manag. **44**, 2839–2856 (2003).

34. N. E. Claytor and R. N. Claytor, "Polymer Imaging Optics for the Thermal Infrared," SPIE **5406**, 107–113 (2004).

35. R. J. Zwiers and G. C. Dortant, "Aspherical lenses produced by a fast high-precision replication process using UV-curable coatings.," Appl. Opt. **24**, 4483 (1985).

36. B. Goss, "Bonding glass and other substrates with UV curing adhesives," Int. J. Adhes. Adhes. **22**, 405–408 (2002).

37. C. Y. Huang, C. C. Chen, C. R. Chang, H. Y. Chou, Y. W. Lin, and C. H. Hwang, "Fabrication of a Hybrid Aspheric Lens Using Glass and Thermosetting Polymer

Molding Technique," Mater. Sci. Forum **773**–**774**, 525–533 (2013).

38. C.-Y. Huang, C.-C. Chen, K.-S. Chang, H.-Y. Chou, W.-Y. Hsu, and T.-X. Lee, "Fabrication of a hybrid optical micro-component with a thermosetting polymer and glass," **8769**, 87693O (2013).

39. D. Morihara, H. Hiroshima, and Y. Hirai, "Numerical study on bubble trapping in UV-nanoimprint lithography," Microelectron. Eng. **86**, 684–687 (2009).

40. S. Askins, M. Victoria, R. Herrero, C. Domín uez, I. Antón, G. Sala, F. Dimroth, S. Kurtz, and A. W. Bett, "Effects of Temperature on Hybrid Lens Performance," AIP **57**, 57–60 (2011).

41. L. Li, P. He, F. Wang, K. Georgiadis, O. Dambon, F. Klocke, and A. Y. Yi, "A hybrid polymer–glass achromatic microlens array fabricated by compression molding," J. Opt. **13**, 55407 (2011).

42. T. Takahata, K. Matsumoto, and I. Shimoyama, "A Silicon-Glass Hybrid Lens for Simultaneous Color-and-Thermal Imaging," IEEE 1408–1411 (2013).

43. D. Vicker and R. LeBlanc, "Midwave Infrared Imager with Plastic Laminated Diffractive / Aspheric Surfaces," SPIE **4369**, 642–648 (2001).

44. D. Vicker, "Infrared optic using polymer layered lens," SPIE **4832**, 315–319 (2002).

45. J. Yan, T. Zhou, J. Masuda, and T. Kuriyagawa, "Modeling high-temperature glass molding process by coupling heat transfer and viscous deformation analysis," Precis. Eng. **33**, 150–159 (2009).

46. J. Yan, T. Zhou, N. Yoshihara, and T. Kuriyagawa, "Shape transferability and microscopic deformation of molding dies in aspherical glass lens molding press," J. Manuf. Technol. Res. **1**, 85–102 (2009).

47. X. Zhu, T. W. Simon, and T. Cui, "Hot embossing at viscous state to enhance filling process for complex polymer structures," Microsyst. Technol. **18**, 257–265 (2011).

48. Y. Xie, C. a S. Hill, Z. Xiao, H. Militz, and C. Mai, "Silane coupling agents used for natural fiber/polymer composites: A review," Compos. Part A Appl. Sci. Manuf. **41**, 806–819 (2010).

49. A. Baldan, "Adhesion phenomena in bonded joints," Int. J. Adhes. Adhes. **38**, 95–116 (2012).

50. M. P. Larsson and M. M. Ahmad, "Improved polymer–glass adhesion through micro-mechanical interlocking," J. Micromechanics Microengineering **16**, S161–S168 (2006).

51. W. MacBain and D. Hopkins, "," J Phys Checm **29**, (1925).

52. Springer, Handbook of Adhesion Technology (Springer, 2011).

53. L. H. Sharpe and H. Schonhorn, "Surface Energetics, Adhesion, and Adhesive Joints," Contact Angle, Wettability, Adhes. 189–201 (1964).

54. S. Yang, L. Gu, and R. Gibson, "Nondestructive detection of weak joints in adhesively bonded composite structures," Compos. Struct. **51**, 63–71 (2001).

55. J. J. Bikerman, "The Science of Adhesive Joints," Acad. Press. New-York London 1961 (1961).

56. A. J. Kinloch, "Review The science of adhesion," J. Mater. Sci. **15**, 2141–2166 (1980).

57. W. J. Aziz, A. Ramizy, K. Ibrahim, Z. Hassan, and K. Omar, "The effect of anti-reflection coating of porous silicon on solar cells efficiency," Opt. - Int. J. Light Electron Opt. **122**, 1462–1465 (2011).

58. R. Volkel, M. Eisner, and K. J. Weible, "Miniaturized imaging systems," Microelectron.

Eng. **67**–**68**, 461–472 (2003).

59. P. Nussbaum, R. Völkel, H. P. Herzig, M. Eisner, and S. Haselbeck, "Design, fabrication and testing of microlens arrays for sensors and microsystems," Pure Appl. Opt. J. Eur. Opt. Soc. Part A **6**, 617–636 (1999).

60. Y. He, J.-Z. Fu, and Z.-C. Chen, "Optimization of control parameters in micro hot embossing," Microsyst. Technol. **14**, 325–329 (2007).

61. A. R. Abdul Manaf and J. Yan, "Press molding of a Si–HDPE hybrid lens substrate and evaluation of its infrared optical properties," Precis. Eng. **43**, 429–438 (2016).

62. Y. Guo, G. Liu, X. Zhu, and Y. Tian, "Analysis of the demolding forces during hot embossing," Microsyst. Technol. **13**, 411–415 (2006).

63. F. Omar, E. Brousseau, A. Elkaseer, A. Kolew, P. Prokopovich, and S. Dimov, "Development and experimental validation of an analytical model to predict the demoulding force in hot embossing," J. Micromechanics Microengineering **24**, 55007 (2014).

64. K. Kendall, "Shrinkage and peel strength of adhesive joints," J. Phys. D. Appl. Phys. **6**, 1782–1787 (2002).

65. Y. Guo, G. Liu, Y. Xiong, J. Wang, X. Huang, and Y. Tian, "Study of hot embossing using nickel and Ni-PTFE LIGA mold inserts," J. Microelectromechanical Syst. **16**, 589–597 (2007).

66. J. Sudagar, J. Lian, and W. Sha, "Electroless nickel, alloy, composite and nano coatings - A critical review," J. Alloys Compd. **571**, 183–204 (2013).

67. D. Gutsev, M. Antonov, I. Hussainova, and A. Y. Grigoriev, "Effect of SiO_2 and PTFE additives on dry sliding of NiP electroless coating," Tribol. Int. **65**, 295–302 (2013).

68. J. M. Li, C. Liu, and J. Peng, "Effect of hot embossing process parameters on polymer flow and microchannel accuracy produced without vacuum," J. Mater. Process. Technol. **207**, 163–171 (2008).

69. N. Chaix, C. Gourgon, S. Landis, C. Perret, M. Fink, F. Reuther, and D. Mecerreyes, "Influence of the molecular weight and imprint conditions on the formation of capillary bridges in nanoimprint lithography.," Nanotechnology **17**, 4082–4087 (2006).

70. E. V. Miu, A. J. Fox, S. H. Jubb, and K. Wakabayashi, "Morphology and toughness enhancements in recycled high-density polyethylene (rHDPE) via solid-state shear pulverization (SSSP) and solid-state/melt extrusion (SSME)," J. Appl. Polym. Sci. **133**, n/a-n/a (2016).

71. H. Taylor, Y. C. Lam, and D. Boning, "An investigation of the detrimental impact of trapped air in thermoplastic micro-embossing," J. Micromechanics Microengineering **20**, 65014 (2010).

72. H. Schift and L. Heyderman, "Pattern formation in hot embossing of thin polymer films," Nanotechnology **173**, (2001).

73. M. Heckele and W. K. Schomburg, "Review on micro molding of thermoplastic polymers," J. Micromechanics Microengineering **14**, R1–R14 (2004).

74. J. Giboz, T. Copponnex, and P. Mélé, "Microinjection molding of thermoplastic polymers: a review," J. Micromechanics Microengineering **17**, R96–R109 (2007).

75. M. Le Berre, J. Shi, C. Crozatier, G. Velve Casquillas, and Y. Chen, "Micro-aspiration assisted lithography," Microelectron. Eng. **84**, 864–867 (2007).

76. T. Zhang, Y. He, and J. Z. Fu, "Simulation Research on Stress of Polymeric Patterns during Micro Hot Embossing," Appl. Mech. Mater. **80**–**81**, 339–345 (2011).

77. P. Jin, Y. Gao, and T. Liu, "Simulation of filling characteristics during hot embossing of polymer microstructures," in (Fifth International Symposium on Instrumentation Science and Technology, 2008), Vol. 7133, p. 71334N–71334N–6.

78. S. Reddy, P. R. Schunk, and R. T. Bonnecaze, "Dynamics of low capillary number interfaces moving through sharp features," Phys. Fluids **17**, 1–6 (2005).

79. H. Hocheng and C. C. Nien, "In-situ monitoring of cavity filling in nanoimprints by capacitance," Japanese J. Appl. Physics, Part 1 Regul. Pap. Short Notes Rev. Pap. **45**, 5590–5596 (2006).

80. J. S. Jha and S. S. Joshi, "Numerical simulation of micro hot embossing of polymer substrate," Int. J. Precis. Eng. Manuf. **13**, 2215–2224 (2012).

81. Y. Wang, Q. Zhang, X. Kuang, Y. Ding, F. Chen, and H. Liu, "Research on hot embossing process of high fill factor microlens array," Microsyst. Technol. **21**, 2109–2114 (2014).

82. Y.-C. Chen, H.-C. Lin, and Y.-D. Lee, "The Effects of Phenyltrimethoxysilane Coupling Agents on the Properties of PTFE/Silica Composites," J. Polym. Res. **11**, 1–7 (2004).

83. H. R. Zafarani, M. Abdi, and M. E. Bahrololoom, "Wear Behavior of PTFE–Hydroxyapatite Composite Fabricated by Hot-Press Sintering Process," Acta Metall. Sin. (English Lett. **27**, 347–351 (2014).

84. A. Vijayakumar and B. Shanti, Design and Fabrication of Diffractive Optical Elements with MATLAB (SPIE, 2017).

85. B. Kim, M. Choi, H. Kim, J. Lim, and S. Kang, "Elimination of flux loss by optimizing the groove angle in modified Fresnel lens to increase illuminance uniformity, color uniformity and flux efficiency in LED illumination.," Opt. Express **17**, 17916–17927

(2009).

86. R. Kasztelanic, I. Kujawa, R. Stępień, K. Haraśny, D. Pysz, and R. Buczyński, "Fresnel lens fabrication for broadband IR optics using hot embossing process," Infrared Phys. Technol. **60**, 1–6 (2013).

87. A. Davis and F. Kühnlenz, "Optical Design using Fresnel Lenses Basic Principles and some Practical Examples," Opt. Photonik, Wiley 52–55 (2007).

88. A. R. Abdul Manaf and J. Yan, "Improvement of form accuracy and surface integrity of Si-HDPE hybrid micro-lens arrays in press molding," Precis. Eng. **47**, 469–479 (2017).

89. L. Peng, Y. Deng, P. Yi, and X. Lai, "Micro hot embossing of thermoplastic polymers: a review," J. Micromechanics Microengineering **24**, 13001 (2014).

90. C. Liu, J. M. Li, J. S. Liu, and L. D. Wang, "Deformation behavior of solid polymer during hot embossing process," Microelectron. Eng. **87**, 200–207 (2010).

91. T. Fujii, A. Goulet, K. Hattori, K. Konno, A. Tanaka, R. Bosmans, M. Sawada, and H. Yazawa, "Fresnel lens sidewall design for imaging optics," J. Eur. Opt. Soc. **10**, (2015).

92. J. W. Horwitz, "Infrared refractive index of polyethylene and a polyethylene-based material," Opt. Eng. **50**, 93603 (2011).

93. "Introduction to Modulation Transfer Function," http://www.edmundoptics.com/resources/application-notes/optics/introduction-to-modulation-transfer-function/. Feb 14, 2017

94. G. D. Boreman, "Transfer function techniques," Handb. Opt. 1–10 (1995).

95. F. A. Jenkins and H. E. White, Fundamentals of Optics, 4th Edit. (The McGraw-Hills, 2001).

LIST OF ACHIEVEMENT

Articles in periodicals (related to thesis)

1. A. R. Abdul Manaf and J. Yan, "Press molding of a Si–HDPE hybrid lens substrate and evaluation of its infrared optical properties," Precision Engineering **43**, 429–438 (2016).
2. A. R. Abdul Manaf and J. Yan, "Improvement of form accuracy and surface integrity of Si-HDPE hybrid micro-lens arrays in press molding," Precision Engineering **47**, 469–479 (2017).
3. A. R. A. Manaf, T. Sugiyama, and J. Yan, "Design and fabrication of Si-HDPE hybrid Fresnel lenses for infrared imaging systems," Optics Express **25**, 1202-1220 (2017).

Articles in international conference proceedings

1. A. R. Abdul Manaf and J. Yan, "Press molding of Si-HDPE hybrid lens substrate for infrared optical applications," in Proceedings of the 8th International Conference on Leading Edge Manufacturing in 21st Century, LEM 2015 (2015).

Presentations at international conferences

1. A. R. Abdul Manaf and J. Yan, "Press molding of Si-HDPE hybrid lens substrate for infrared optical applications," The 8th International Conference on Leading Edge Manufacturing in 21st Century (LEM21), 18-22 October 2015, Kyoto, Japan.

2. A. R. Abdul Manaf and J. Yan, "Press molding of extremely thin hybrid optics for IR applications" Invited presentation, Symposium of Optoelectronic Technology and Applications (OTA 2016), 9-11 May 2016, Beijing, China.
3. A. R. Abdul Manaf and J. Yan, "In-situ observation of hot press molding of Si-HDPE hybrid micro-lens array", The 5th International Conference on Nanomanufacturing (nanoMan 2016), 15-17 August 2016, Macau, China.
4. A. R. Abdul Manaf, T. Sugiyama, and J. Yan, "Press molding of Si-HDPE hybrid micro Fresnel lenses for IR imaging" International Symposium on Micro-nano Science and Technology 2016 (MNST 2016), 16-18 December 2016, Tokyo, Japan.

Awards

1. Best Paper Award, A. R. Abdul Manaf and J. Yan, "Press molding of Si-HDPE hybrid lens substrate for infrared optical applications," The 8th International Conference on Leading Edge Manufacturing in 21st Century (LEM21), 18-22 October 2015, Kyoto, Japan.